Defense Threat Reduction Agency
8725 John J. Kingman Road, MS
6201 Fort Belvoir, VA 22060-6201

DTRA-TR-18-7

TECHNICAL REPORT

A Novel Multiscale QM-MD-SPH Computational Method for Heterogeneous Multicomponent Reactive Systems

November 2017

HDTRA1-13-1-0025

G. Liu et al.

Prepared by:
University of Cincinnati
733 Rhodes Hall
Cincinnati, OH 45221

DESTRUCTION NOTICE:

Destroy this report when it is no longer needed.
Do not return to sender.

PLEASE NOTIFY THE DEFENSE THREAT REDUCTION AGENCY, ATTN: DTRIAC/ RD-NTF, 8725 JOHN J. KINGMAN ROAD, MS-6201, FT BELVOIR, VA 22060-6201, IF YOUR ADDRESS IS INCORRECT, IF YOU WISH IT DELETED FROM THE DISTRIBUTION LIST, OR IF THE ADDRESSEE IS NO LONGER EMPLOYED BY YOUR ORGANIZATION.

REPORT DOCUMENTATION PAGE

Form Approved
OMB No. 0704-0188

1. REPORT DATE *(DD-MM-YYYY)*	**2. REPORT TYPE**	**3. DATES COVERED** *(From - To)*
30-11-2017	Technical	July 1, 2016 - December 9, 2016

4. TITLE AND SUBTITLE

A Novel Multiscale QM-MD-SPH Computational Method for Heterogeneous Multicomponent Reactive Systems

5a. CONTRACT NUMBER
HDTRA1-13-1-0025

5b. GRANT NUMBER

5c. PROGRAM ELEMENT NUMBER

6. AUTHOR(S)

Liu,Guirong
Wang,Guangyu
De,Suvranu
Peng,Qing

5d. PROJECT NUMBER
J9BAP6209

5e. TASK NUMBER

5f. WORK UNIT NUMBER

7. PERFORMING ORGANIZATION NAME(S) AND ADDRESS(ES)

University of Cincinnati
733 Rhodes Hall,Cincinnati, OH 45221
Rensselaer Polytechnic Institute
110 8th ST, Troy, NY, 12108

8. PERFORMING ORGANIZATION REPORT NUMBER

9. SPONSORING / MONITORING AGENCY NAME(S) AND ADDRESS(ES)

Defense Threat Reduction Agency
8725 John J. Kingman Road, STOP 6201
Fort Belvoir, VA 22060-6201

10. SPONSOR/MONITOR'S ACRONYM(S)
DTRA

11. SPONSOR/MONITOR'S REPORT NUMBER(S)
DTRA-TR-18-7

12. DISTRIBUTION / AVAILABILITY STATEMENT

Distribution Statement A. Approved for public release; distribution is unlimited.

13. SUPPLEMENTARY NOTES

14. ABSTRACT

This project aims to develop a novel three-stage coupled multi-scale QM-MD-SPH approach for modeling and simulation of complex heterogeneous multicomponent reactive systems, considering both high explosive (HE) explosion effects. The novelty of our approach is that the unified particle-based approaches couples the dynamic events over nine orders of magnitude length scales (nm-m) and twelve orders of magnitude timescales (ps-s). This is achieved by using ab initio quantum mechanics (QM) approaches at the nano scale, molecular dynamics (MD) at the micro scale and smoothed particle hydrodynamics (SPH) at the continuum scale.

15. SUBJECT TERMS

multi-scale modeling, high explosive, ab initio model, quantum mechanics, molecular dynamics

16. SECURITY CLASSIFICATION OF:			**17. LIMITATION OF ABSTRACT**	**18. NUMBER OF PAGES**	**19a. NAME OF RESPONSIBLE PERSON**
					Allen Dalton
a. REPORT	**b. ABSTRACT**	**c. THIS PAGE**	UU	146	**19b. TELEPHONE NUMBER** *(include area code)*
UU	UU	UU			703-767-3054

Standard Form 298 (Rev. 8-98)
Prescribed by ANSI Std. Z39.18

UNIT CONVERSION TABLE

U.S. customary units to and from international units of measurement*

U.S. Customary Units	Multiply by → / ← Divide by†		International Units
Length/Area/Volume			
inch (in)	2.54	$\times 10^{-2}$	meter (m)
foot (ft)	3.048	$\times 10^{-1}$	meter (m)
yard (yd)	9.144	$\times 10^{-1}$	meter (m)
mile (mi, international)	1.609 344	$\times 10^{3}$	meter (m)
mile (nmi, nautical, U.S.)	1.852	$\times 10^{3}$	meter (m)
barn (b)	1	$\times 10^{-28}$	square meter (m^2)
gallon (gal, U.S. liquid)	3.785 412	$\times 10^{-3}$	cubic meter (m^3)
cubic foot (ft^3)	2.831 685	$\times 10^{-2}$	cubic meter (m^3)
Mass/Density			
pound (lb)	4.535 924	$\times 10^{-1}$	kilogram (kg)
unified atomic mass unit (amu)	1.660 539	$\times 10^{-27}$	kilogram (kg)
pound-mass per cubic foot (lb ft^{-3})	1.601 846	$\times 10^{1}$	kilogram per cubic meter (kg m^{-3})
pound-force (lbf avoirdupois)	4.448 222		newton (N)
Energy/Work/Power			
electron volt (eV)	1.602 177	$\times 10^{-19}$	joule (J)
erg	1	$\times 10^{-7}$	joule (J)
kiloton (kt) (TNT equivalent)	4.184	$\times 10^{12}$	joule (J)
British thermal unit (Btu) (thermochemical)	1.054 350	$\times 10^{3}$	joule (J)
foot-pound-force (ft lbf)	1.355 818		joule (J)
calorie (cal) (thermochemical)	4.184		joule (J)
Pressure			
atmosphere (atm)	1.013 250	$\times 10^{5}$	pascal (Pa)
pound force per square inch (psi)	6.984 757	$\times 10^{3}$	pascal (Pa)
Temperature			
degree Fahrenheit (^oF)	$[T(^oF) - 32]/1.8$		degree Celsius (^oC)
degree Fahrenheit (^oF)	$[T(^oF) + 459.67]/1.8$		kelvin (K)
Radiation			
curie (Ci) [activity of radionuclides]	3.7	$\times 10^{10}$	per second (s^{-1}) [becquerel (Bq)]
roentgen (R) [air exposure]	2.579 760	$\times 10^{-4}$	coulomb per kilogram (C kg^{-1})
rad [absorbed dose]	1	$\times 10^{-2}$	joule per kilogram (J kg^{-1}) [gray (Gy)]
rem [equivalent and effective dose]	1	$\times 10^{-2}$	joule per kilogram (J kg^{-1}) [sievert (Sv)]

*Specific details regarding the implementation of SI units may be viewed at http://www.bipm.org/en/si/.

†Multiply the U.S. customary unit by the factor to get the international unit. Divide the international unit by the factor to get the U.S. customary unit.

Abstract

Simulation of reactive energetic materials has long been the interest of researchers due to its extensive applications in military. While substantial research has been done on the subject at macro scale, the research at micro scale has initiated recently. Equation of state (EoS) is the relation between physical quantities (pressure, temperature, energy and volume) describing thermodynamic states of materials under a given set of conditions. It is the key connecting the microscopic and macroscopic behavior when simulating the macro effects of an explosion. For instance, ignition and growth model for high explosives uses two Jones-Wilkins-Lee (JWL) EoSs, one for solid explosive and the other for gaseous products of high explosive. The JWL EoS of gaseous products is obtained by conducting explosion experiments, which are expensive, time-consuming and hazardous. It would be much less expensive and hazardous to obtain the EoSs of energetic materials through computational method instead of field experiments. In this project, we developed a novel three-stage coupled multi-scale QM-MD-SPH approach to model complex heterogeneous multicomponent reactive systems. Our QM-MD-SPH approach is particle-based covering nine orders of magnitude length scales (nm-m) and twelve orders of magnitude timescales (ps-s) and it is capable of easing accommodation of multi-species systems, and each of the species as well as their interfaces are traceable during the simulation of explosion events. In this work, the EoSs of solid β-HMX and gaseous products of β-HMX are calculated using molecular dynamics (MD) simulation with ReaxFF-d3, a reactive force field obtained from quantum mechanics (QM) simulations based on the first principle. The microscopic QM-MD simulation results are shown to compare well with the experimental data, other numerical methods and some empirical ignition and growth models. The calculated QM-MD EoSs are then incorporated into our smoothed particle hydrodynamics (SPH) code to simulate the macro effects of explosions of high explosive. An ignition and growth model is integrated into the SPH codes to simulate the detonation of high explosives. Further, an afterburning model is integrated in ignition and growth model and implemented in our QM-MD-SPH package to simulate explosion of aluminized explosives. In addition, a Godunov SPH method is also incorporated in our SPH package, which integrates Riemann solver and eliminates the need for artificial viscosity in the standard SPH. Our QM-MD-SPH model is validated using benchmark numerical example problems in one- and two-dimensions of detonation of PBX 9501 explosives. The techniques proposed in this report can also be used to simulate the terminal effects of both high explosives (HEs) and casing breakage/fragmentation.

Table of Content

List of Figures

List of Tables

Chapter 1-Introduction: background and motivation

HMX, or octahydro-1,3,5,7-tetranitro-1,3,5,7-tetrazocine, is a powerful high explosive with extensive applications in the military industry. For example, it is used to implode the fissionable material in a nuclear device, as a component of plastic-bonded explosives, and as a component of rocket propellant. It is of great importance to investigate the properties of HMX numerically and experimentally. The typical morphologies of HMX crystals are shown in Figure 1.1 [1].

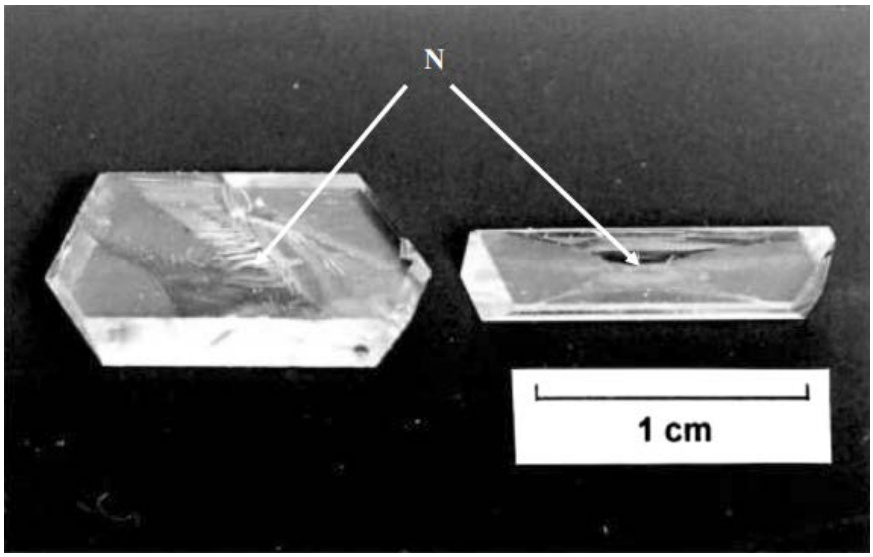

Figure 1.1 The typical morphologies of HMX crystals

The equation of state (EoS), which describes the thermodynamic states of materials under a given set of conditions, plays a significant role in determining the characteristics of energetic materials, such as Chapman-Jouguet (CJ) point and detonation velocity [2]. Furthermore, the EoS is the key to connect microscopic and macroscopic phenomena in the study of energetic materials. For example, the EoS is the foundation of various numerical models for high explosives [3-7], such as the JWL++ model, and ignition and growth model. The JWL++ model consists of two EoSs, one for the solid explosives and the other for gaseous products of high explosives. The two EoSs are mixed using a simple additive rule according to the reaction progress of the explosive. The JWL++ model does not include any physical assumptions, thus, it is only a primitive numerical model and the results produced by the model are not accurate. The other numerical model, ignition and growth model also consists of two EoSs, similar to JWL++ model. The difference is that in the ignition and growth model, two physical assumptions (pressure equilibrium and temperature equilibrium) is introduced, leading to a more complicated but also more accurate mixture rule. As the most popular numerical model for the simulation of high explosives, ignition and growth model has been integrated in commercial software ANSYS and LS-DYNA.

EoSs of high explosives are usually obtained from fitting experimental data. Much research has been done on the Hugoniot EoS of solid materials. Walsh et al. initiated the idea in 1955 to use planar shock

waves to determine the EoS of condensed materials [8]. Afterwards, shock wave experiment has been extensively applied to obtain the EoS of a wide range of materials, such as elements, compounds, alloys, porous materials [9-13]. Some researchers successfully applied planar shock waves in the study of Hugoniot EoS of explosives [14, 15]. Specially, Yoo et al. obtained the EoS of crystal HMX using isotropic pressure experiment [16]. To obtain EoS of gaseous products of high explosives, cylinder test is often conducted. Cylinder test involves recording the detonation velocity and wall displacement of a copper tube filled with explosive sample, which is detonated from one end. The standard tube is 1 in internal, 0.1 in wall and 12 in long [17]. The results of cylinder test are often tuned and fitted to obtain EoS of gaseous products and then applied in numerical models mentioned above.

However, it is usually expensive and hazardous to conduct experiments on high explosives. To reduce cost and unnecessary risks, an economic method is needed to obtain EoSs of solid explosive and gaseous products of explosive. Thus, molecular dynamics (MD) simulation is considered to fulfill the task. Molecular dynamics is a powerful tool to investigate microscopic processes. In recent years, the detonation of high explosives has been explored more profoundly with the introduction of reactive force fields (ReaxFF) in molecular dynamics [18]. Furthermore, Liu et al. introduced an additional vdW-like interaction to ReaxFF, which enables ReaxFF to obtain the correct density of molecular crystals [19]. Strachan et al. studied thermal decomposition of RDX under various temperature and densities [20]. Chenoweth et al. studied thermal decomposition of a poly polymer with ReaxFF [21]. Zhang et al. studied thermal decomposition of 1,3,5-trinitrohexahydro-s-triazine (RDX) bonded with polyurethane (Estane) using molecular dynamics simulation equipped with ReaxFF [22]. However, their research mainly focuses on the thermal decomposition of high explosives. In this work, the geometry of the primitive unit cell of the β-HMX is obtained from our previous DFT-D2 study [23]. The EoSs of solid explosive and gaseous products of β−HMX are calculated using ReaxFF-d3, a reactive force field obtained from quantum mechanics simulation. The calculated EoSs of β-HMX are compared with experiment [16] and EoSs in ignition and growth model [24]. Then, the calculated EoSs are incorporated in the smoothed particle hydrodynamics (SPH) code to simulate the macroscopic explosion of PBX 9501, which contains 95% HMX, 2.5% Estane and 2.5% BDNPA-F.

Aluminized explosive is an enhanced metalized explosive (e.g. HMX-Al), which usually contains high explosive such as HMX, and uses aluminum particles (5~10 μm in diameter) as additive. The mass fraction of Al powder ranges from 20% to 40% or even higher. Aluminized explosives have extensive application in military industry. Different from ideal explosives like TNT, HMX, RDX, and TATB, aluminized explosives feature both fast detonation of high explosives and slow combustion of aluminum particles. The detonation of high explosives occurs in microseconds, oppositely, the combustion of

aluminum particles takes milliseconds or even longer. Due to the addition of aluminum powder, aluminized explosives have relatively low brisance but high blast potential [25].

The detonation of aluminized explosives is rather complicated. The underlying mechanism of the chemical reaction is still not thoroughly understood till today. Modeling the detonation and subsequent combustion requires a particular knowledge of the chemical kinetics [26].

To investigate the detonation of high explosives and aluminized explosives, researches have conducted experiments and performed theoretical analyses. Wilkins et al. obtained the Chapman-Jouguet pressure and equation of state of PBX 9404 through experiments [27]. Wackerle et al. investigated the pressure history of PBX 9404 through planar shock initiation [28]. Cook et al. measured detonation pressure and detonation velocity of TNT-Al and other aluminized explosives [25]. Due to the complexity of the problem, it takes longer time for researchers to understand the mechanism theoretically. Boiko et al. studied the ignition of aluminum powers in shock waves, and measured the relationship between reaction rate and temperature [29]. Khul et al. proposed a model to calculate the reaction rate of the combustion of aluminum under shock waves [30-32]. Based on these models, Kuhl et al. investigated the explosion of aluminized explosive [31]. However, the model proposed by Kuhl et al. is way too complicated. It also has other disadvantages such as negative internal energy, which is incompatible with mainstream model of high explosive such as ignition and growth model. Thus, a simplified afterburning model is employed in this work. The idea is to use a reaction rate model to describe the combustion of aluminum particles. Heat will be gradually released along with the chemical reaction. The details of the model will be introduced in the following chapters. There have been abundant literatures on the application of afterburning model to simulate combustion of aluminum particles. Togashi et al. investigated the detonation and afterburning effects of AFX 757 and TNT-Al in confined facility [33, 34]. The simulation agrees well with measurements. Zhou et al. studied the detonation of aluminized explosive using the same model and good agreement with experiment is observed [35]. However, they just use simple JWL model to simulate the detonation of high explosives. In this work, afterburning model is combined with ignition and growth model so that the detonation of high explosive and combustion of aluminum particles can be investigated simultaneously.

The numerical method used in this work is smoothed particle hydrodynamics (SPH) method. SPH is a mesh-free Lagrangian method which was first developed by Gingold, Monaghan and Lucy et al. [36, 37] to study astrophysics. Compared with Euler method, SPH method is advantageous in tracking free interfaces and dealing with large deformation, thus it has been extended to fluid dynamics and solid mechanics to simulate high-velocity impact and explosion. Liu et al. [38-41] investigated the feasibility of using SPH to simulate explosion of high explosives, underwater explosion, and shaped charge detonation.

However, in these literatures, the numerical model for explosive is just simple JWL model, which is much less accurate than ignition and growth model.

In this project, a SPH method incorporated with ignition and growth model is proposed to study high explosives and aluminized explosives. The simulation results are compared with experiment and finite volume method (FVM) solution, and good agreement is observed, which indicates that the proposed method is reliable and sufficiently accurate. Then, the EoSs calculated from molecular dynamics simulation are applied in SPH codes to investigate high explosive and aluminized explosive.

A more advanced SPH method, Godunov method is described, which integrates Riemann solver and eliminates the need for artificial viscosity, which is a significant improvement compared with traditional SPH with artificial viscosity. A shock tube problem is investigated using Godunov SPH to validate the accuracy of the algorithm. Then, the Godunov SPH is applied in the simulation of high explosive.

A three-dimensional SPH model with JWL++ model is developed for non-ideal explosive ANFO. The influence of smoothing length on simulation is investigated. A three-dimensional cylinder test model is developed to test the stability and accuracy of the proposed SPH method with JWL++ model.

Chapter-2 DFT-D2 study of HMX using Quantum Mechanics (QM) Approach

2.1 Accurate modeling of the density of HMX using DFT-D2 study

Density is one of the most important physical properties of solid energetic materials [42, 43] because it determines the detonation velocity and detonation pressure, which are used to assess the potential performance of this energetic material [44]. In addition, density plays an important role in the equations of state describing thermodynamic properties, which can be used to describe materials at continuum level [45]. Despite its importance, the accurate prediction of the densities of energetic materials is challenging [46]. Although first-principles calculations based on density functional theory (DFT) provide overall better predictive power than force field models, they fail in predicting densities of energetic materials with standard approximations, partially due to their poor descriptions of dispersion forces in molecular crystals [47-51].

There are extensive studies to improve the modeling of dispersion interactions, or van der Waals (vdW) interactions. These studies can be classified into two approaches. One approach is the modification of the exchange-correlation functions in the standard DFT formula [52-54]. The other approach is to add an energy term for empirical corrections to the total energy [55-64]. The latter approach is more popular since it takes much less computing resources than the former, within acceptable accuracy. Although there are dramatic improvements referring to standard DFT calculations, previous modellings [49, 65] with vdW corrections in DFT-D1 method [55] still show considerable errors in densities compared to experiments. A significant improvement in the prediction of equilibrium densities and isothermal equations of state for hydrostatic compressions of energetic materials at nonzero temperatures was achieved by combining van der Waals corrections with thermal and zero-point energy corrections (denoted as DFT-D1-T method) [45]. However, substantial complexity and computing demand associated with the reported DFT-D1-T method render its application impractical for large systems. The DFT-D2 method [57] is a revised version of DFT-D1 method [55] and has considerable improvement of its predecessor with negligible extra computing demands comparing to the standard DFT calculations. Its application in studying the structural properties and equations of state of β-HMX under high pressure needs further investigation.

HMX, also known as cyclotetramethylene-tetranitramine, or 1,3,5,7-Tetranitro-1,3,5,7-tetrazocane, or tetrahexamine tetranitramine, is an important secondary explosive that is most commonly used in polymer-bonded explosives, and as a solid rocket propellant.The HMX molecular crystal has three pure crystallographic polymorphs, as α, β, and δ phases. The P21/c monoclinic β-phase molecular crystal, as shown in the Figure 2.1(a), is the thermo-dynamically most stable polymorph of HMX at room temperature and has highest density. A molecule with a ring-chain structure in the β-HMX crystal is shown in Figure 2.1(b). Due to its importance, HMX becomes objective of extensive studies, both

experimental and theoretical. It is generally believed that the β phase exists only below 375K at ambient pressure, or at room temperature with pressure below 10 GPa.

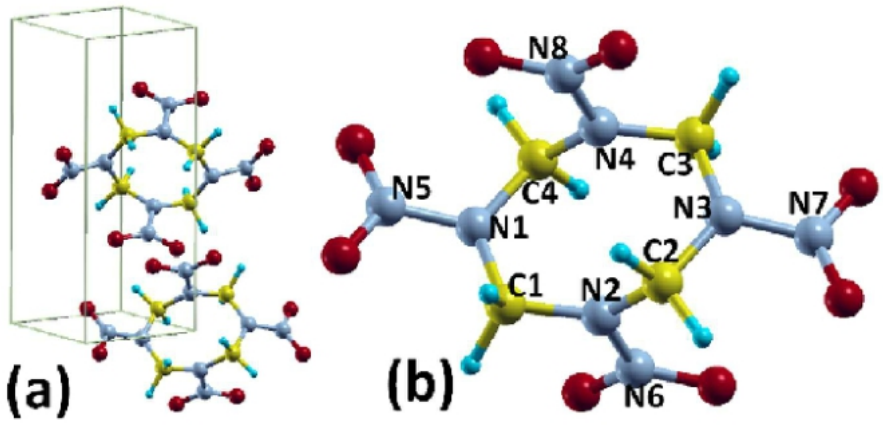

Figure 2.1 Geometry of β-HMX.

The unit cell of β-HMX containing two HMX molecules with ring-chain structure is shown in Figure 2.1. The four carbon atoms (yellow) and four nitrogen atoms form the ring-chain. In Figure 2.1(b), a molecule with a ring-chain structure is shown. The molecule is center-symmetric.

It can be seen from Figure 2.1(b) that the N1-N3 and N2-N4 forms major and minor axis of the ring-chain structure, respectively. The four carbon atoms are coplanar on theC4-plane. The four nitrogen atoms on the ring-chain are also coplanar on the N4-plane.The angle between C4-plane and N4-plane is 30.3°.

Here we model β-HMX using DFT-D2 method [57], which describes the van der Waals interactions as a simple pair-wise force field. This method is chosen as a result of compromise between two opposite considerations: accuracy and feasibility. We investigate the molecular structure, mechanical properties, and equations of state of the β-HMX. To the best of our knowledge, for the first time, we predict the elastic constants of β-HMX using DFT-D2 calculations.

We consider a conventional unit cell containing two HMX molecules (56 atoms in total) with periodic boundary conditions, as depicted in Figure 2.1. The total energies of the system, forces on each atom, stresses, and stress-strain relationships of β-HMX under the desired deformation configurations are characterized via first-principles calculations based on density-functional theory (DFT). DFT calculations were carried out with the Vienna Ab-initio Simulation Package (VASP) [66, 67] which is based on the Kohn-Sham Density Functional Theory (KS-DFT) [68, 69] with the generalized gradient approximations as parameterized by Perdew, Burke, and Ernzerhof (PBE) for exchange-correlation functions [70]. The electrons explicitly included in the calculations are the $1s^1$ for hydrogen atoms, $2s^22p^4$ electrons for carbon atoms, $2s^22p^5$ for nitrogen atoms, and $2s^22p^6$ for oxygen atoms. The core electrons are replaced by the projector augmented wave (PAW) and pseudo-potential approach [71, 72]. The kinetic-energy cutoff

for the plane-wave basis was selected to be 800 eV in this study. The calculations are performed at zero temperature.

The criterion to stop the relaxation of the electronic degrees of freedom is set by total energy change to be smaller than 0.000001 eV. The optimized atomic geometry was achieved through minimizing Hellmann-Feynman forces acting on each atom until the maximum forces on the ions were smaller than 0.001 eV/Å. The atomic structures of all the deformed and undeformed configurations were obtained by fully relaxing a 168-atom-unit cell. The simulation invokes periodic boundary conditions for the three directions. The irreducible Brillouin Zone was sampled with a $5 \times 3 \times 4$ Gamma-centered k-mesh. The initial charge densities were taken as a superposition of atomic charge densities.

In the DFT-D2 method [57], the van der Waals interactions are described using a pair-wise force field. Such a semi-empirical dispersion potential is then added to the conventional Kohn-Sham DFT energy as $E_{DFT-D2} = E_{DFT} + E_{disp}$, and

$$E_{disp} = -\frac{1}{2}\sum_{i=1}^{N}\sum_{j=1}^{N}\sum_{L}{}' \frac{C_{6ij}}{r_{ij,L}^{6}} f_{d,6}(r_{ij,L}) \qquad \text{Eqn 2.1}$$

where N is the number of atoms. The summations go over all atoms and all translations of the unit cell $= (l_1, l_2, l_3)$. The prime indicates that for $= 0$, $i \neq j$. C_{6ij} stands for the dispersion coefficient for the atom pair j . $r_{ij,L}$ is the distance between atom i in the reference cell $L = 0$ and atom j in the cell L. $f(r_{ij})$ is a damping function whose role is to scale the force field such as to minimize contributions from interactions within typical bonding distances r. Since the van der Waals interactions decay quickly in the power of -6, the contributions outside a certain suitably chosen cutoff radius are negligible. The cutoff radius for pair interaction in this study is set to 30.0 Å. Here Fermi-type damping function is used as

$$f_{d,6}(r_{ij}) = \frac{s_6}{1+e^{-d\left(\frac{r_{ij}}{srR_{0ij}}-1\right)}} \qquad \text{Eqn 2.2}$$

where S_6 is the global scaling parameter. The global scaling factor $S_6 = 0.75$ is used for PBE exchange-correlation functions. S_R is fixed at 1.00. The damping parameter $d = 20.0$ is used.

Compared to DFT-D2 method, the DFT-D1 method [55] has a few shortcomings: (1) It has parameters available only for elements H, C-Ne. (2) There are systematic errors for calculations of molecules containing third-row elements. (3) It leads to inconsistencies for thermochemistry due to double-counting problem [57]. In addition to overcome these shortcomings, DFT-D2 generalized the dispersion correction and improved the accuracy.

We first optimize the geometry of the monoclinic crystal (also shown in Figure 2.1) by full relaxation of all the atoms and lattice constants. The optimized lattice constants are: a=6.542 Å, b=10.842 Å, c= 8.745 Å, α=γ=90◦, and β=124.413◦. For the comparison, we also optimize the structure without the van der Waals corrections. Our results of the lattice constants, the volume of the unit cell, and the densities are

summarized in Table 2.1 and compared to the experiment and previous theoretical results. It shows that the standard DFT calculations give poor predictions. For example, the volume of the unit cell is 6.7% higher than the experimental value. The prediction of the density of β-HMX from our DFT-D2 calculations is more accurate, with a difference of -1.47% compared to the experimental value. This is a significant improvement over standard DFT calculations without van der Waals corrections.

Table 2.1 Lattice constants a, b, c, lattice angle β, volume of the unit cell V, and density ρ predicted from DFT and DFT-D2 calculations, compared with experiments and previous calculations. The numbers in parentheses are differences in percentage referring to the experiment.

	a (Å)	b (Å)	c (Å)	β	V(Å^3)	$\rho(10^3 Kg/m^3)$
Expt.a	6.54	11.05	8.70	124.30	519.39	1.894
Expt.b	6.537	11.054	8.7018	124.443	518.558	1.897
Expt.c	6.5255	11.0369	7.3640	102.670	517.45	1.901
Expt.d	6.54	11.05	7.37	102.8	519.37	1.894
DFT	6.673(+2.03%)	11.312(+2.37%)	8.894(+2.23%)	124.395(+0.08%)	553.99(+6.66%	1.775(-6.23%)
DFT-D2	6.542(+0.03%)	10.842(-1.88%)	8.745(+0.52%)	124.41(+0.09%)	511.73(-1.47%)	1.923(+1.53%)
Theory e	6.70(+2.45%)	11.35(+2.71%)	8.91(+2.41%)	124.13(-0.14%)	560.86(+7.98%)	1.754(-7.39%)
Theory f1	6.38(-2.45%)	10.41(-5.79%)	8.43(-3.1%)	123.0(-1.05%)	463.1(-10.74%)	2.122(12.03%)
Theory f2	6.90(+5.50%)	11.65(+5.43%)	9.15(+5.17%)	124.5(+0.16%)	608.1(+17.08%)	1.617(-14.59%)
Theory f3	6.56(+0.31%)	10.97(-0.72%)	8.70(0.0%)	124.4(+0.08%)	517.4(-0.38%)	1.901(+0.38%)
Theory g2	6.78(+3.67%)	11.48(+3.89%)	9.19(+5.63%)	125.02(+0.58%)	585.57(+12.74%)	1.680(-11.30%)
Theory g1	6.43(-1.68%)	10.34(+6.43%)	8.61(-1.03%)	124.23(-0.06%)	473.81(-8.78%)	2.076(+9.62%)
Theory h	6.539(-0.02%)	11.03(-0.18%)	8.689(-0.13%)	123.9(-0.32%)	520.17(+0.15%)	1.891(-0.15%)
Theory i	6.762(+3.39%)	11.461(+3.72%)	8.865(+1.90%)	123.8(-0.40%)	570.599(+9.89%)	1.724(-8.97%)
Theory j	6.67(+1.99%)	11.17(+1.09%)	8.95(+2.87%)	124.5(+0.16%)	549.30(+5.76%)	1.791(-5.45%)
Theory k	6.57(+0.46%)	11.02(-0.27%)	9.04(+3.91%)	124.9(+0.48%)	531.12(+2.26%)	1.852(-2.21%)
Theory l	6.58(+0.61%)	11.12(+0.63%)	8.76(+0.69%)	124.3(+0.0%)	529.8(+2.0%)	1.856(-1.96%)
Theory m	6.57(+0.46%)	10.63(-3.80%)	9.13(+4.94%)	123.67(-0.51%)	530.6(+2.16%)	1.854(-2.11%)
Theory n1	-	-	-	-	556.07(+7.06%)	1.769(-6.60%)
Theory n2	-	-	-	-	500.77(-3.58%)	1.964(+3.72%)
Theory n3	-	-	-	-	519.41(+0.0%)	1.894(0.00%)

a: Ref.73,16; b: Ref.74; c: 303 K space group P 21/n in Ref.50; d : space group P21/n in Ref.75; e: DFT study using PAW-PBE (GGA) in Ref.49; f1: DFT study using USPP-LDA in Ref.76; f2: DFT study using USPP-PBE(GGA) in Ref.76; f3: DFT-D2 study using USPP-PBE(GGA) in Ref.76; g1: DFT study using USPP-LDA in Ref.77; g2: DFT study using USPP-PBE(GGA) in Ref.77; h: DFT study using USPP-LDA in Ref.78; i: DFT study using USPP-PBE(GGA) in Ref.79; j: Monte Carlo calculations in Ref.80; k: Molecular Dynamics study in Ref.81; l: Molecular Dynamics study in Ref.82.

The one non-standard cell commonly used is $P_{21/n}$ which is derived from $P_{21/c}$. The lattice vectors a_0 , b_0 , and c_0 in space group $P_{21/n}$ can be transformed to space group $P_{21/c}$ as $a = -a_0$, $b = -b_0$, and $c = a_0 + b_0$.

In general, the molecular dynamics (MD) simulations predict better lattice vectors than the standard DFT calculations. It is partially because the MD calculations include the van der Waals interactions. Once the van der Waals corrections are introduced, the first-principles calculations [45] show good predictions with accuracy within 3% of the experimental values.

2. 2 Equation of State of HMX up to 100 GPa

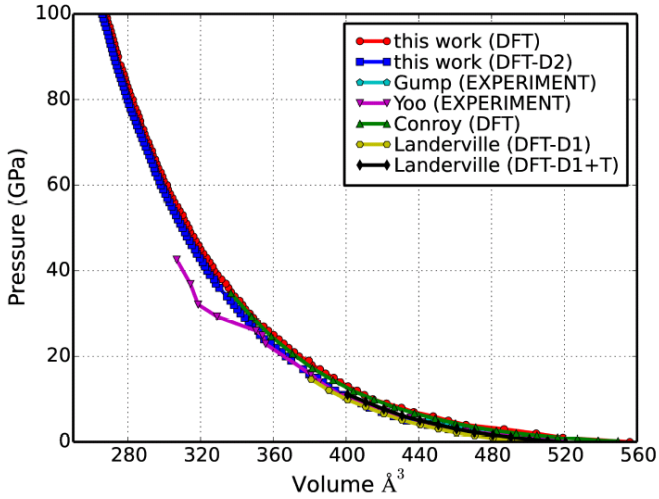

(a) The EoS of the solid β-HMX at zero temperature.

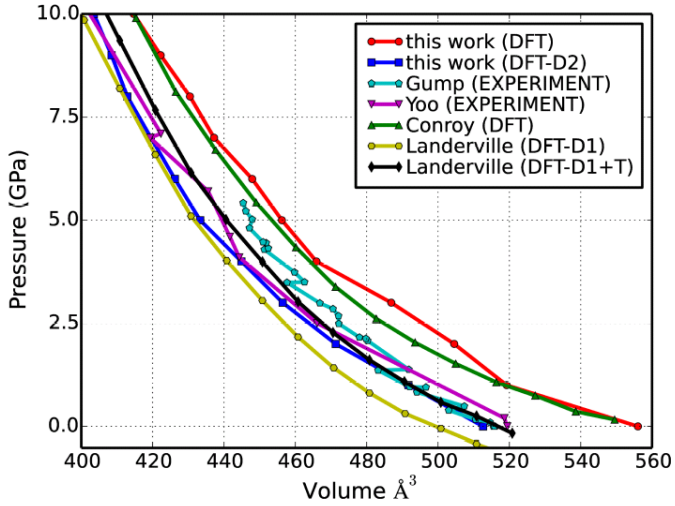

(b) The detailed EoS of the solid β-HMX at zero temperature. Volume ranges from 400 Å^3 to 560 Å^3

Figure 2.2 Equation of state. The pressure-volume relationship of the solid β-HMX at zero temperature.

We study the isothermal equations of states of β-HMX at zero temperature under hydrostatic pressures. The corresponding volume is obtained after the system is fully relaxed. The pressure-volume curve of unreacted β-HMX at the temperature of 0K was illustrated in Figure 2.2. The volume corresponds to the 56-atom-unitcell volume. The isothermal hydrostatic equation of state of β-HMX is compared with experiments (Gump [83] and Yoo [16]) and previous calculations (Conroy [49] and Landerville [45]) . The upper panel shows pressure from 0-100 GPa. The corresponding volume in the present DFT-D2 calculations varies from 512.64 $Å^3$ (100%) to 265.95 $Å^3$ (51.9%). The lower panel shows pressure from 0-10 GPa for better comparison. Unlike standard DFT calculation (blue-circle line), our DFT-D2 study (red-square line) shows reasonably good agreement with the hydrostatic-compression experiments [83, 16], suggesting that the Van der Waals interaction is critically important in modeling the mechanical properties of this molecular crystal.

In Figure 2.2, the volume is the 56-atom-unit-cell volume. The upper panel shows pressure from 0-100 GPa. The corresponding volume in the present DFT-D2 calculations varies from 512.64 $Å^3$ (100%) to 265.95 $Å^3$ (51.9%). The lower panel shows pressure from 0-10 GPa for better comparison. The experiments (Gump [84] and Yoo [16]) and previous calculations (Conroy [49] and Landerville [45]).

It is worthy pointing out that the experimental data were collected at room temperature. Whereas, our results are for zero temperature and we have not corrected the results to account for finite temperature. Moreover, our calculations are performed using the β polymorph of HMX, which is consistent with the experimental data of Gump and Peiris [83]. As observed in previous studies [49, 84] the calculated isotherm appears to approach experimental curve with increasing pressure. However, as discussed below, the sample from the experiment of Yoo and Cynn [16] is no longer in the β phase for pressures beyond 12 GPa.

In order to determine the bulk modulus and its derivative with respect to pressure, the calculated hydrostatic-compression data, up to about 12 GPa, were fit to the third-order Birch-Murnaphan (BM) equations of states, [85, 49] as

$$P = \frac{3}{2}B_0\left(\eta^{-7/3} - \eta^{-5/3}\right)\left[1 + \frac{3}{4}(B_0' - 4)(\eta^{-2/3} - 1)\right] \qquad \text{Eqn. 2.3}$$

where $\eta = V/V_0$ is the ratio of volume V in response to P to the equilibrium volume V_0 at zero pressure. B_0 is the bulk modulus and $B_0' = \frac{\partial B_0}{\partial P}$ is the pressure derivative of bulk modulus.

The values of B_0 and $B_0^{'}$ from both standard DFT and DFT-D2 calculations are listed in Table 2.2, compared to experimental values [16, 83] and theoretical predictions [49, 45] that are also obtained from fitting to the BM equations of states. The errors from the fitting process of this study are also listed in the Table 2.2. Our results agree with experiments and the previous predictions. Moreover, our bulk modulus from this BM EOS fitting also agrees with elastic constants calculations in previous subsection.

Table 2.2 The Bulk modulus B and its derivative with respect to pressure B' fitted from the isothermal equations of states from DFT and DFT-D2 studies, compared to experiments and theoretical predictions. The error-bar rises in the least-square fitting process.

	Source	B_0 (GPa)	error	B_0'	error
Ref. [16]	Expt	16.7		6.8	
Ref. [83]	Expt	21.0		7.45	
DFT-D2	Theory	14.46	$\pm$ 0.98	9.96	$\pm$0.98
DFT	Theory	13.62	$\pm$ 2.8	6.5	$\pm$ 0.8
Ref. [49]	Theory	9.8		9.1	
Ref. [45]	Theory	16.74		7.78	

By comparing the predictions from DFT-D2 and standard DFT, one can conclude that the van der Waals correction is necessary for accurate modeling the elastic properties of β-HMX.

2.3 Structural response of HMX to hydrostatic compression: molecular "hot spots"

We studied the evolution of the structures of β-HMX under high pressures. Firstly we studied the lattice structures including lattice constants and lattice angles. We observed that the lattice constant b and lattice angle β are more sensitive to the applied pressures. We then studied the bond lengths of C-H, C-N, N-O, and N-N bonds. We noticed that the N-N bonds are vulnerable to pressure. We further studied the bending angle between N-N bonds with the plane formed by carbon atoms.We found the N-N bonds along the minor axis of the ring are more susceptible to pressure.

The lattice constants a, b, and c as a function of hydrostatic pressure p are plotted in Figure 2.3, compared with experimental results from Gump [83] and Yoo [16]. For a good comparison, three panels for the range from (a) 0-10 GPa, (b) 0-40 GPa, and (c) 0-100 GPa are presented, while keeping the y in the same scale.There is a good agreement of the lattice constants between our DFT-D2 predictions with the experiments under the pressure of 10 GPa where there is no phase transition.At the pressure of 12 GPa, there is a phase transition in experiment.

The lattice constants a, b and c as a function of hydrostatic pressure p ranging from 0-10 GPa, 0-40 GPa, and 0-100 GPa is shown in Figure 2.3(a), (b), (c) respectively. Simulation results are compared with experiments from Gump [83] and Yoo [16].

At the pressure of 36 GPa, there is another phase transition observed in the experiment. However, those phase transitions were not observed in our computations, partly due to the small cells which exclude

the long wavelength phonon modes in addition to the zero temperature that preclude the dynamic instabilities.

We noticed that the lattice constant b is more sensitive to the pressure than lattice constants a and c.

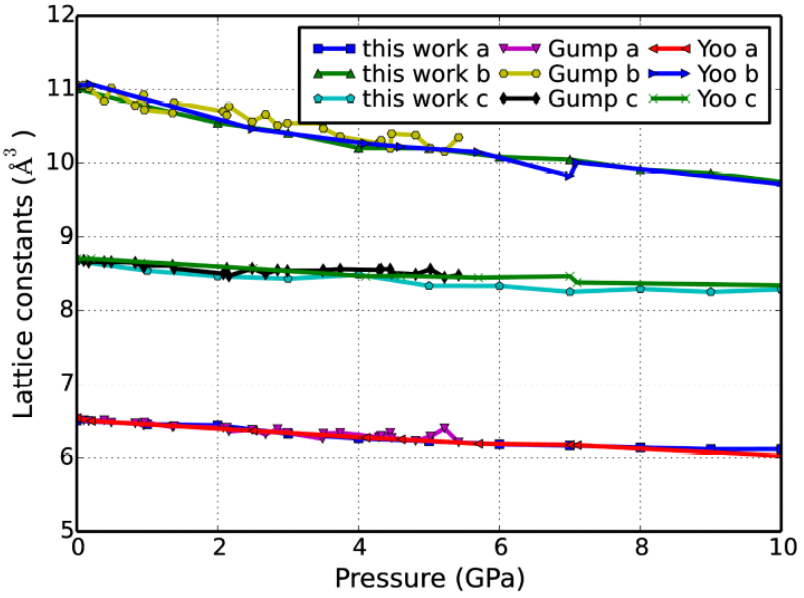

(a) Lattice constants a, b and c as a function of hydrostatic pressure p ranging from 0-10 GPa

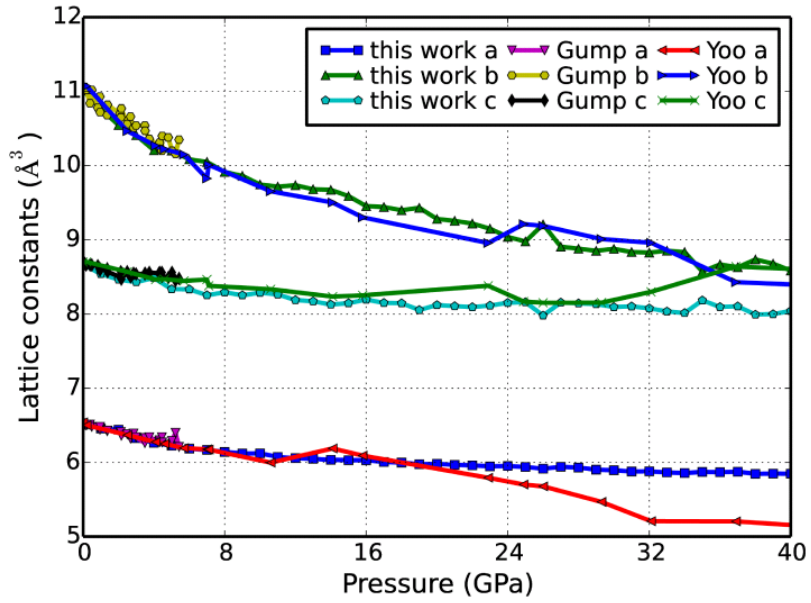

(b) Lattice constants a, b and c as a function of hydrostatic pressure p ranging from 0-40 GPa

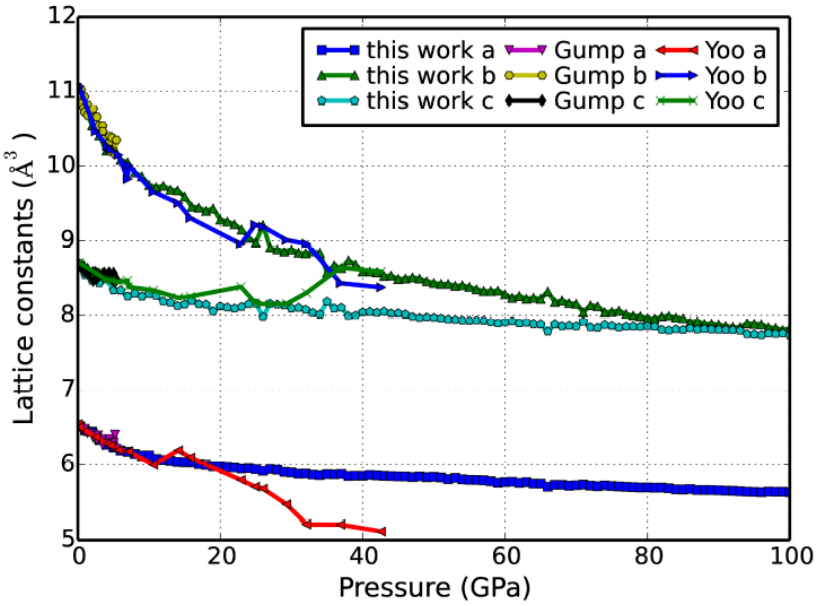

(c) Lattice constants a, b and c as a function of hydrostatic pressure p ranging from 0-100 GPa

Figure 2.3 Lattice constants a, b, and c under high pressure.

Similar to the lattice constants, we studied the lattice angles as a function of hydrostatic pressure. We found that the angle α and γ varies little under pressures. On the contrary, the angle β is more sensitive to pressure. The β angle as a function of hydrostatic pressure p are plotted in Figure 2.4, and compared with experimental results from Gump [83] and Yoo [16].

Notice that the phase transition is clearly reflected in the experimental plots, whereas, it is absent in the simulation plots due to the small cell and zero temperature constrain in the DFT-D2 modeling.In spite of these differences, there is a reasonably good agreement between the lattice constants obtained in our DFT-D2 calculations and experiments. Furthermore, we noticed that the lattice angle β is the most sensitive to pressure among all three lattice angles.

The lattice angle β as a function of hydrostatic pressure p ranging from 0-10 GPa, 0-40 GPa, 0-100 GPa is shown in Figure 2.4(a), (b), (c) respectively. Simulation results are compared with experiments from Gump [83] and Yoo [16].

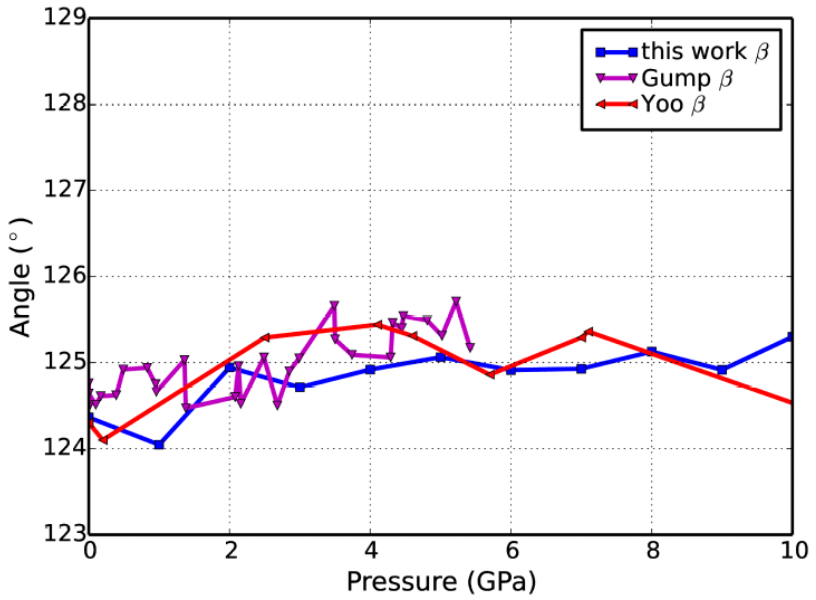

(a) Lattice angle β as a function of hydrostatic pressure p ranging from 0-10 GPa

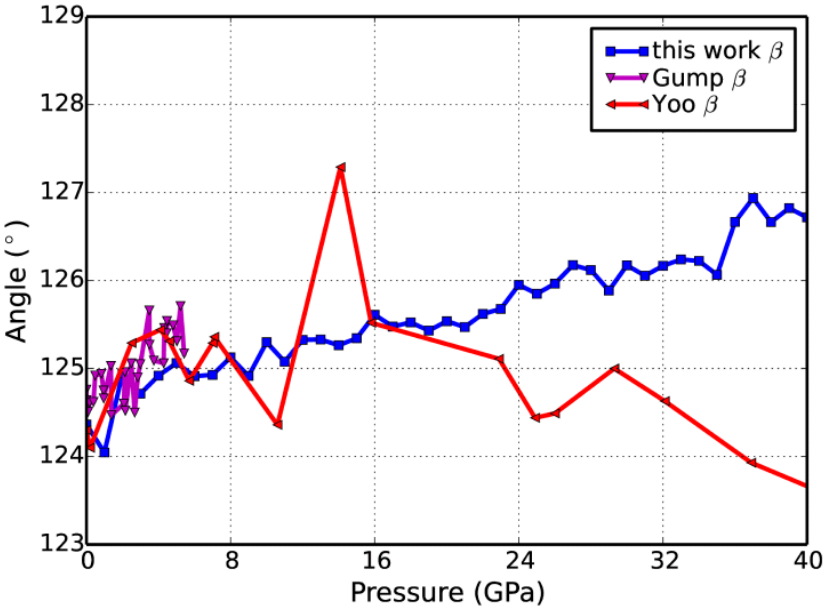

(b) lattice angle β as a function of hydrostatic pressure p ranging from 0-40 GPa

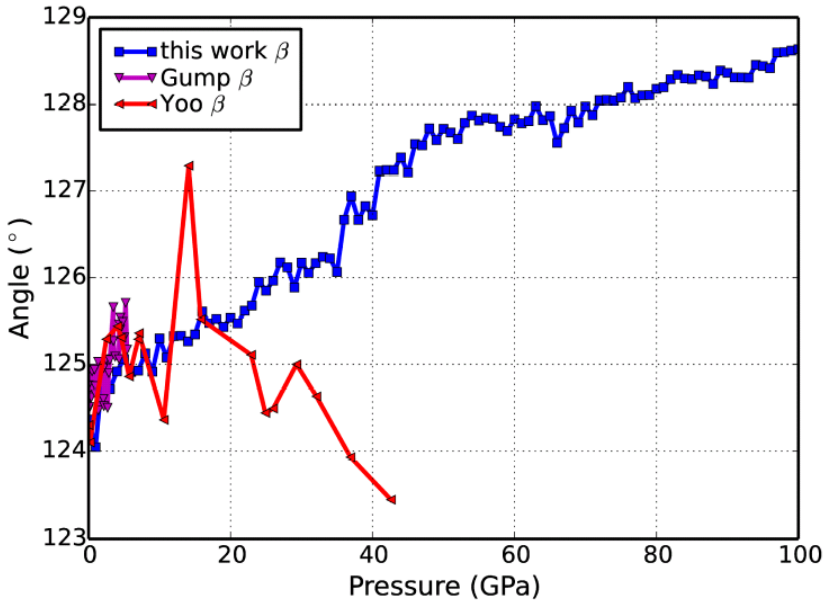

(c) lattice angle β as a function of hydrostatic pressure p ranging from 0-100 GPa

Figure 2.4 Lattice angle β under high pressure.

Next, we examine the bond lengths under various pressures in order to find the atomistic mechanism corresponding to the variations of lattice structures.The bond lengths of the bonds C-H, C-N, N-O, and N-N as a function of hydrostatic pressure p ranged from 0-100 GPa are illustrated in Figure 2.5. In our unit cell, the number of bonds is 16, 16, 16, and 8 for C-H, C-N, N-O, and N-N, respectively. The bond lengths are averaged over the unit cell. Our results show that the N-N bonds are the most sensitive to the applied hydrostatic pressure, which indicates that it is vulnerable to compression.

The bond lengths of C-H, C-N, N-O, and N-N as a function of hydrostatic pressure p ranging from 0-100 GPa are shown in Figure 2.5. The bond lengths are averaged over the unit cell.

In order to find the atomic mechanism corresponding to the variations of lattice structures, we further study examine the bending angles under various pressures. There are two kinds of N-N bonds in a HMX molecule: one along the major axis along N1-N3 of the ring-chain (Figure 2.1b) and the other along the minor axis along N2-N4 of the ring-chain (Figure 2.1b). The four carbon atoms are co-planar, marked as C4-plane. Due to the symmetry, there are two angles between the N-N bonds and the C4-plane.The angle along the major axis is denoted as β1and the angle along the minor axis is denoted as β2. During the compression, the two angles β1and β2might respond differently, causing the anisotropy of the crystal.

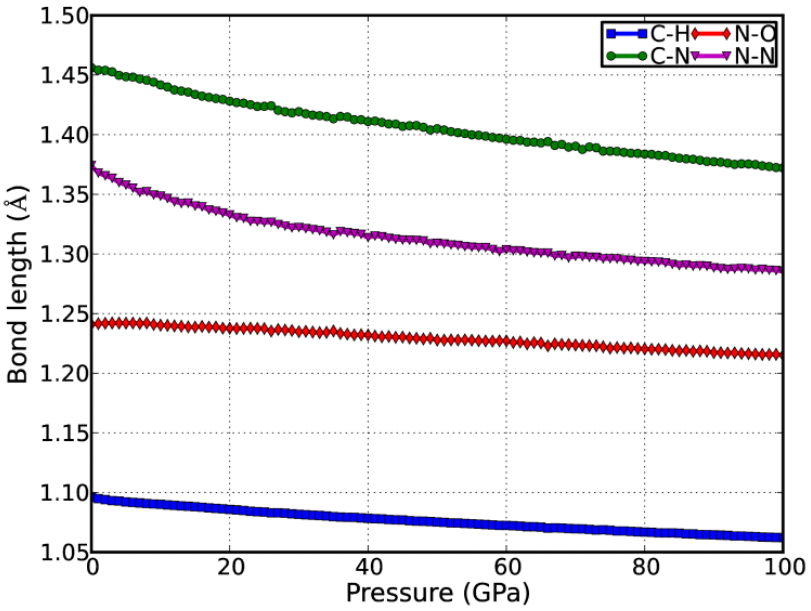

Figure 2.5 Bond lengths under high pressure.

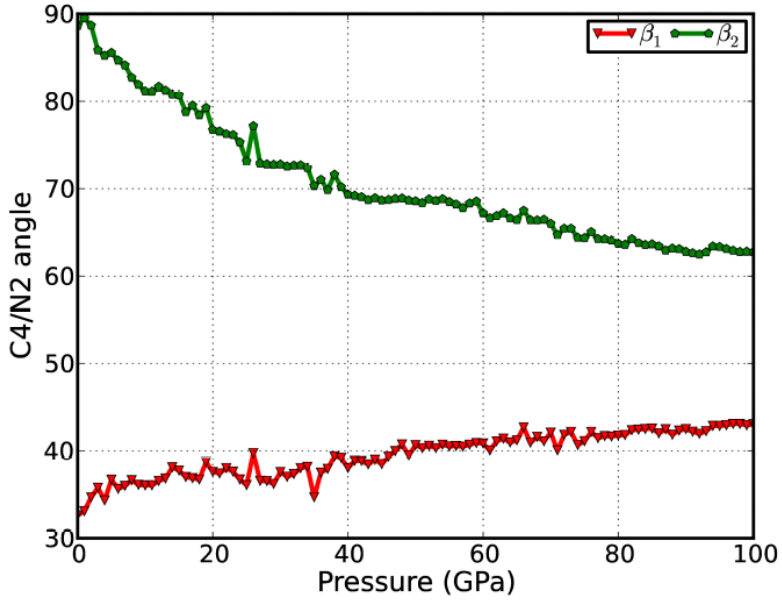

Figure 2.6 Bond angles under high pressure.

The angles (β1 and β2) between the N-N bond and the plane formed by the four carbon atoms as a function of hydrostatic pressure p ranging from 0-100 GPa is shown in Figure 2.6. We found that β1 increases with respect to an increasing pressure, opposite to the decrease of β2. Furthermore, the angle β2 is more sensitive to the applied pressure than the angle β1, indicating that the N-N bonds along the minor

axis are more vulnerable to the compression.Therefore, we may conclude that the N-N bonds along the minor axis are responsible for the sensitivity of β-HMX.

2.4 Elastic properties of HMX

We next calculate the elastic properties of β-HMX. The elastic constants are the second derivatives of the total energy with regard to strain. For the first time, we predict the elastic constants of β-HMX using DFT-D2 method. Our results of all 13 elastic constants, in standard Voigt notation 45, are listed in Table 2.3, and compared with experiments and theoretical pre- dictions. Our results show that the prediction from standard DFT studies is far off the experiments, but the prediction from DFT-D2 agrees reasonably well with the experiments.

Table 2.3 13 Non-zero elastic constants C_{ij}, bulk modulus B , shear modulus G , Poisson's ratio ν , and Cauchy pressure $C_P(C_P = C_{12} - C_{44})$ of β-HMX predicted from DFT and DFT-D2 calculations, compared with experiments and previous calculations. The units are GPa except Poisson ratio

	C_{11}	C_{12}	C_{13}	C_{15}	C_{22}	C_{23}	C_{25}	C_{33}	C_{35}	C_{44}	C_{46}	C_{55}	C_{66}	B	G	ν	C_p
Expt a.	20.58	9.65	9.75	-0.61	19.69	12.93	4.89	18.24	1.57	9.92	4.42	7.69	10.67	13.69	7.40	0.271	-0.27
Expt b.	18.41	6.37	10.50	-1.10	14.41	6.42	0.83	12.44	1.08	4.77	2.75	4.77	4.46	10.20	4.26	0.317	1.6
Expt c.	19.4	5.9	8.4	-1.1	17.5	8.2	3.2	17.8	0.2	9.1	2.4	9.2	9.8	11.08	7.77	0.217	-3.2
Expt d.	20.8	4.8	12.5	-0.5	26.9	5.8	-1.9	18.5	1.9	4.2	2.9	6.1	2.5	12.49	5.43	0.310	0.6
DFT	75.1	18.6	1.4	-23.4	28.9	24.6	1.0	44.5	-14.2	23.4	-8.0	18.7	28.7	26.41	21.09	0.185	-4.8
DFT-D2	29.3	10.6	13.8	-2.1	25.0	16.6	6.2	27.5	1.1	13.6	6.8	12.8	13.9	18.20	10.78	0.253	-3.0
MD f	22.2	9.6	13.2	-0.1	23.9	13.0	4.7	23.4	1.6	9.2	2.5	11.1	10.1	15.68	8.33	0.274	0.4
MD g	13.6	3.75	4.66	-0.15	9.50	5.07	-2.71	13.2	-0.96	6.41	-2.1	4.04	4.68	7.03	4.55	0.234	-2.7
DFT h	22.2	5.0	11.5	1.3	23.1	8.2	2.2	15.3	3.5	4.1	4.7	5.5	1.6	12.22	4.63	0.332	0.9

a: Ref[75]; b: Ref[86]; c: Ref[87]; d: Ref[88];e: Ref[89];f: Ref[82],g: Ref[90];h: Ref[91]

For a valid comparison, the Cartesian system to which the elastic constants referenced must be the same for all these data sets. We used the reference system of the x and y axes parallel to the a - and b - crystallographic axes, respectively, which is the same as Sewell Bibliography entry and Stevens Bibliography entry . Zaug's results (d in Table 2.3) were transformed to this Cartesian system by Sewell. Note that the experimental studies prefer using the $P21/n$ space group over standard $P21/c$ space group. The elastic constants in these two space groups are identical except that $C_{15}^c = -C_{15}^n$, $C_{25}^c = -C_{25}^n$, $C_{35}^c = -C_{35}^n$, and $C_{46}^c = -C_{46}^n$, where supper index c refers to space group $P21/c$ and super index n

refers to space group $P21/n$. For a valid comparison, we transformed our results of C_{ij}^{c} into the form of C_{ij}^{n} (Table 2.3).

The bulk modulus B measures the resistance to hydrostatic compression and it can be calculated using the Voigt notation from the elastic constants as:

$$B = \frac{1}{9}\sum_{i,j}^{3} C_{ij} \qquad \text{Eqn 2.4}$$

Our calculated value of the bulk modulus is 18.2 GPa, which is larger than the average value 11.9 GPa of the four sets of experimental values. It is well known that the theoretical elastic constants are often stiffer compared to those of experiments. This overestimation is attributed to two factors: the use of the rigid-body approximation for flexible molecules, and the neglect of the anharmonic softening of the lattice at finite temperatures. Our DFT studies are performed at zero temperature where the thermodynamics as well as the anharmonic softening are excluded. This is reflected in the larger value of our predicted bulk modulus.

The shear modulus measures the resistance in shearing. The shear deformations have been proposed to be a critical component in the initiation of detonation. Therefore, a precise determination of the shear modulus is necessary for substantiating possible detonation mechanisms. The shear modulus G can be calculated using the Voigt notation from elastic constants as:

$$G = \frac{1}{15}(C_{11} + C_{22} + C_{33} - C_{12} - C_{23} - C_{13}) + \frac{1}{5}(C_{44} + C_{55} + C_{66}) \qquad \text{Eqn 2.5}$$

Our result of the shear modulus is 10.8 GPa, which is larger than the average value, 6.2 GPa, of the four sets of experimental values. This is partially attributed to the preclusion of the anharmonic softening of the lattice with temperature.

The Poisson ratio measures the shape change under mechanical loading. For an isotropic material, the Poisson ratio v is related with bulk modules and shear modulus as:

$$\nu = \frac{3B-2G}{2(3B+G)} \qquad \text{Eqn 2.6}$$

We predicted that the Poisson ratio is 0.253, which is slightly smaller than the average (0.278) of the four sets of experimental values. Interestingly, opposite to the bulk modulus and shear modulus, the Poisson ratio agrees well with the experiments.

The Cauchy pressure $C_P = C_{12} - C_{44}$ can be used to evaluate the deductibility of a material [92]. The positive value of C_P indicates that the material is ductile whereas the negative value implies a brittle material. The larger positive value means that the material is more ductile. The results of ductibility from both experiments and molecular dynamics studies are controversial. For example, two experiments [75, 87] indicate β-HMX is brittle, but other two [86, 88] imply that β-HMX is ductile. The average C_P of the four experiments is -0.32. Our DFT and DFT-D2 studies indicate that the β-HMX is brittle, but with

much larger magnitudes. The possible reasons of that our model predicts much lower ductibility than experiments are twofold. First, the simulation boxes in the DFT and DFT-D2 modeling are small, which exclude the long wavelength phonon modes that contribute to the ductility. Second, the zero temperature applied in our models precludes the thermodynamics effects, which is essential for the ductility. As a result, the ductibility of our models appears to be much smaller.

The diagonal elements C_{ii} describe the crystal stiffness under uniaxial compression ($i = 1,2,3$) and shear ($i = 4,5,6$), whereas the off-diagonal elements $C_{i\neq j}$ presents the crystal stiffness under biaxial compression ($i \neq j = 1,2,3$) and distortion ($i \neq j = 4,5,6$). Our results show that there is a remarkable anisotropy in the diagonal elements of the elastic constant tensor. Furthermore, it indicates that the β-HMX is anisotropic upon compression and has a good stability to shear deformation perpendicular to the c-axis.

Here C_{22} is relevant to the "doorway mode" anharmonic coupling model, which is an important feature of detonation of secondary explosives. [93] Experimental and theoretical vibrational analysis illustrates the presence of low-energy modes that have the necessary symmetry for such anharmonic coupling. The experimental value of C_{22} varies from 14.41 GPa to 26.9 GPa, with an average of 19.63 GPa. Our predicted value (25 GPa) of C_{22} agrees with experiments. Especially, it is very close to the experimental findings (26.9 GPa) [88].

2.5 Bandgaps of HMX under hydrostatic compression

The impact sensitivity is a very important characteristic of an energetic material, and it is closely related to its production, storage, transportation, and detonation. It is believed that the electronic bandgap is correlated with the impact sensitivity of an energetic material [94, 78]. The bandgap is the electronic energy difference between the HOMO (highest occupied molecular orbital) and LUMO (lowest unoccupied molecular orbital). Therefore, the study of the electronic properties including the bandgaps may give a clue of the impact sensitivity under hydrostatic compression. The bandgap of β-HMX as a function of hydrostatic pressure is illustrated in the Figure 2.7. It shows that the bandgap monotonically decreases with increasing hydrostatic pressure. This trend could be understood as the decrease of intermolecular space under compression, which leads to an increase of different groups of electronic bands and, hence, to the increase of charge overlap and delocalization.

It is worth mentioning that the rate of decrease of the bandgap is not homogeneous: at lower pressure up to 12GPa, the rate is much larger than those beyond 12 GPa. This indicates that the bandgap energy reduction is more pronounced in the low-pressure region than high-pressure region.

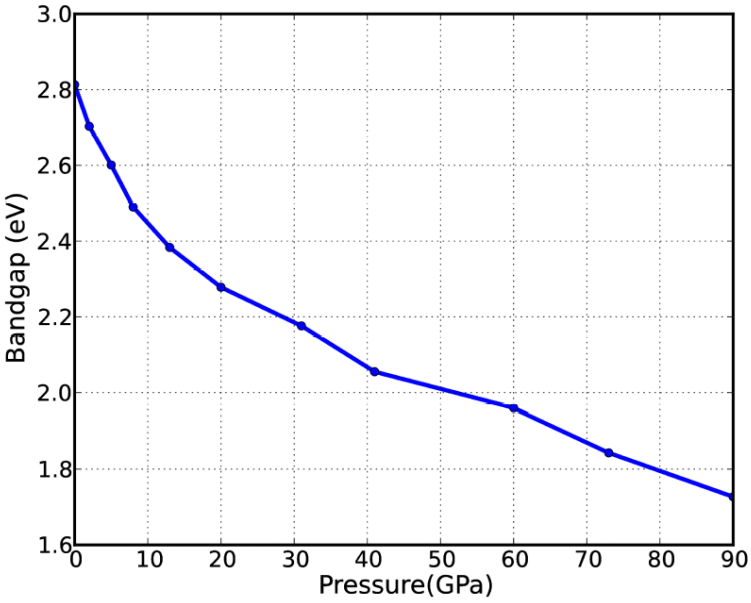

Figure 2.7 The electronic energy bandgap of β-HMX as a function of hydrostatic pressure.

With the monotonic decrease of the bandgap, one could expect that there is a bandgap closure where HMX becomes metallic. It is also proposed that the compression in the detonation fronts causes local metalization which attributed to the shear strains [95]. The bandgap closing produces distortion-induced molecular electronic degeneracy of the highest occupied and lowest unoccupied molecular orbitals of an energetic molecule [96]. The linear fitting of the bandgaps in range of 12-100 GPa gives the reduction ratio of -0.0084 eV/GPa. The extrapolation of such a linear relationship implies that the zero bandgap occurs at 296 GPa. Our result is consistent with a previous theoretical prediction of 320 GPa [78].

Studies on the exitonic mechanism of detonation show that the reduction of the bandgaps promote the HOMO-LUMO transition within a molecule [96, 97], thus increases the sensitivity. The smaller the bandgap is, the higher the possibility that the electron transfers from valence band to conduction band, causing decomposition that may lead to explosion. This correlation between the bandgap and detonation sensitivity could be understood as follows. The number of excited sates increases as a response to the reduction of the bandgap. The increment of the population of excited states augments the possibility of the chemical reactions. As a consequence, it enhances the sensitivity [98]. Therefore, the monotonic decrease of the electronic energy bandgap in Figure 2.7 indicates that the impact sensitivity increases with an increase of hydrostatic pressure.

2.6 Equation of state of HMX at finite temperature using AIMD modeling

Thermal dynamics play a crucial role in the behavior of energetic materials. Especially, the thermal dynamics at high temperature could cause the decomposition of the energetic materials. Accurate

modeling of the energetic materials at finite temperature using first-principles study is computationally demanding and challenging, since it is an extension of the standard first-principles calculation at zero Kelvin temperature.

We studied the equation of states of β-HMX at finite temperature using ab initio molecular dynamics (AIMD) with the VASP package. The simulation box contains 8 HMX molecules, which has 224 atoms. The simulation box is initially compressed, to make the β-HMX at different densities. There are four densities we studied here, 1.90, 2.18, 2.42, 3.05 g/cm^3, corresponding to the pressure of 0, 4, 10, 40 GPa at zero temperature, respectively. At each density, the system was firstly fully relaxed, including the cell and ions. Then the system is subjected to the AIMD modeling with canonical ensemble (NVT). The time step is 1.0 femtosecond (10^{-15} s). Eight temperatures ranged from 50K to 400K are studied. These temperatures were selected to study because they are below the decomposition temperature of β-HMX, which is around 440K. The total time of the simulation of each NVT ensemble is 5.0 picoseconds (10^{-12} s).

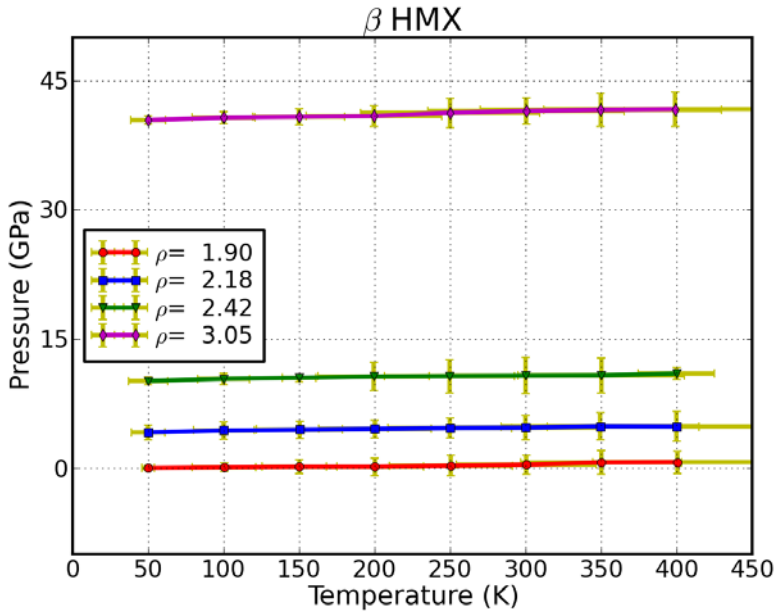

Figure 2.8 Equation of state of β-HMX at different densities and temperatures.

The results of the pressure as a function of temperature are plotted in Figure 2.8 for the 4 densities. It shows that the pressure linearly increases with temperature. It should be noted that the canonical ensemble (NVT) was used for each state (point) using AIMD modeling for 5 picoseconds.

2.7 Mechanical response of β-HMX at the continuum level

We report a theoretical prediction of the mechanical properties of the β-HMX energetic molecular crystal using DFT-D3, a first-principles calculation based on density functional theory (DFT) with van

der Waals (vdW) corrections. The mechanical respons of β -HMX at the continuum level corresponding to the elastic constants predicted from DFT-D3 calculations are compared with experiments, DFT-D2 and standard DFT calculations, and other theoretical calculations, as in Figure 2.9.

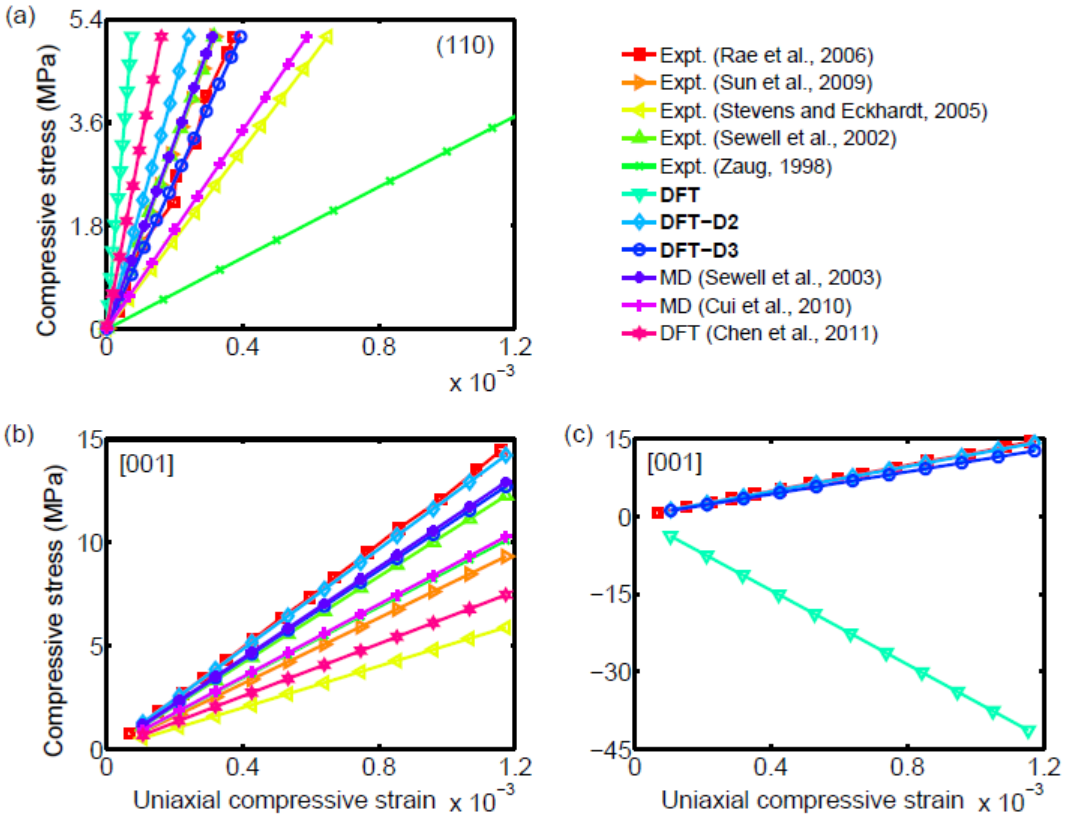

Figure 2.9 Mechanical response of β-HMX.

In Figure 2.9, the mechanical response of β-HMX at the continuum level corresponding to the elastic constants predicted from DFT-D3 calculations are compared with experiments, DFT-D2 and standard DFT calculations, and other theoretical calculations. The squared lines are the direct experimental measurements, opposite to others as interpolation from elastic constants. The uniaxial compressive strains are applied (a) on the (110) plane, and (b) along the [001] direction. (c) The predicted behavior of uniaxial compression along the [001] direction from standard DFT calculations compared with the DFT-D2 and DFT-D3 calculations, and experiment.

Our results show that the DFT-D3 method models the mechanical response of β–HMX better than DFT-D2 method. The standard DFT modeling without van der Waals corrections are not acceptable, as demonstrated in Figure 2.9(c). Our study suggested that the van der Waals interactions are critically important t in modeling the mechanical properties of this molecular crystal.

Chapter 3- QM study of the mechanical properties and the equation of state of Aluminum and Aluminum oxide

It is desirable to further increase the power and thrust output after explosion of explosives. One of the approach is the addition of metal particles to energetic materials. Among them, Aluminum(Al) powders are widely used in pyrotechnics, rocket propellants, and explosives. The aluminized explosives are widely used energetic materials in the military explosives to increase the air blast, incendiary effects, and bubble energies in underwater weapons. Al is also commonly added to propellants to increase the thrust. There is an increased desire to develop combined-effects aluminized explosives to achieve both excellent metal pushing and high blast energies [99], including the study of the detonation characteristics of aluminized explosives [100–103], to understand and predict the macroscopic response of energetic materials on the basis of mechanical properties, which are required in the formulation and parameterization of mesoscale continuum mechanical constitutive models [103-111]. The accurate prediction of the mechanical properties and crystallographic parameters are imperative to the development of physically based constitutive models that are necessary for continuum scale modeling of deformation mechanisms, which affect the sensitivity of energetic molecular crystals such as HMX.

The aluminum powder added into the mixture improves the heat and temperature of the explosion for the mixture and increases the action duration of the explosion. Unlike the homogenous ideal explosive, it is difficult to predict the effect of aluminized explosives because its detonation is not ideal. The EoS for detonation products is needed to predict explosion effects. The EoS for detonation products of ideal homogeneous explosives can be determined easily because its detonation mechanism is simpler and the related research is perfect.

One approach to obtain the EoS of a mixture is to combine the EoS of each component. We take the aluminized HMX as example. There are two ingredients Al (Aluminum) and HMX.

HMX is an important secondary explosive that exists in three crystallographic polymorphs α, β, δ, and in hemi-hydrate γ form. The P21/c monoclinic β-phase molecular crystal (Figure 2.1) is thermodynamically the most stable polymorph of HMX at room temperature [112,16]. β-HMX is a high-density energetic material with a high detonation velocity, which is most commonly used in military and industrial applications including polymer- bonded explosives and propellant formulations. Due to its importance, β-HMX has been the subject of extensive studies both experimental (for example, Ref. [73, 86, 88]) and theoretical, which includes constitutive models [104-111] molecular dynamics simulations [87, 113-115] and first-principles calculations [45, 49, 82]. The structures, mechanical properties, equations of state, and electronic properties of β-HMX under hydro static pressure were studied using a

DFT-D2 method [23]. The predictions of elastic constants under various functionals were reported, as well as EOS.

Aluminum is a common metal used in everyday life. The advantage of using aluminum as an ingredient in aluminized explosives is because of the high performance, as Al is a very active metal with high energy density. Another advantage of aluminized energetic materials is that their reaction products are environmentally friendly. Finally, the materials have in general relatively low production cost. To make our study complete and consistent, we re-investigate the properties and EoS of Aluminum using newly developed more accurate Density Functional Theory calculations.

Mechanical properties including elastic constants are among the most important physical characteristics of solid energetic materials as they provide a description of the mechanical behavior at the continuum level. Although first-principles calculations based on density functional theory (DFT) provide overall better predictive power than pure force-field models (for example, in Ref. [116]), they fail in predicting lattice constants, volumes, and elastic constants of energetic materials with standard approximations, partially due to their poor descriptions of dispersion forces in molecular crystals [23].

We consider a conventional unit cell containing 4 atoms with periodic boundary conditions for face-centered cubic structure which is the most stable phase for Aluminum under ambient condition. The total energies of the system, forces on each atom, stresses, and stress-strain relationships of Al under the desired deformation configurations are characterized via first-principles calculations based on density-functional theory (DFT). DFT calculations were carried out with the Vienna Ab-initio Simulation Package (VASP)[66, 67] which is based on the Kohn-Sham Density Functional Theory (KS-DFT)[68-69] with the generalized gradient approximations as parameterized by Perdew, Burke, and Ernzerhof (PBE) for exchange-correlation functions[70].The electrons explicitly included in the calculations are the 3s23p1 for aluminum atoms, and $2s^2 2p^6$ for oxygen atoms. The core electrons are replaced by the projector augmented wave (PAW) and pseudo-potential approach [71, 72]. The kinetic-energy cutoff for the plane-wave basis was selected to be 800 eV in this study. The calculations are performed at zero temperature. We applied the PBEsol functionals in this study.

The criterion to stop the relaxation of the electronic degrees of freedom is set by total energy change to be smaller than 0.000001 eV. The optimized atomic geometry was achieved through minimizing Hellmann-Feynman forces acting on each atom until the maximum forces on the ions were smaller than 0.001 eV/Å. The atomic structures of all the deformed and undeformed configurations were obtained by fully relaxing the unit cell. The simulation invokes periodic boundary conditions for the three directions. The irreducible Brillouin Zone was sampled with a $16 \times 16 \times 16$ Gamma-centered k-mesh. The initial charge densities were taken as a superposition of atomic charge densities.

We firstly optimized the geometry of the simulation box and obtained the lattice constant of 4.011 Å, which agrees well with experiment 4.05 Å and previous DFT studies ranged from 3.97-4.10 Å.

We examined the electronic band structure, which is illustrated in the Figure 3.1. The Fermi energy is set to be 0.0 eV. The Γ, M, X,K are the four highest symmetric points in the first Brillouin zone, as (0,0,0),(0.5,0,0),(0.5,0.5,0), and (0.5,0.5,0.5) respectively. The energy ranged from -10.3 eV to 16.5 eV. The electron Density of State (DOS) are also plotted aside to the electronic band structure. It clearly shows the consistency with each other.

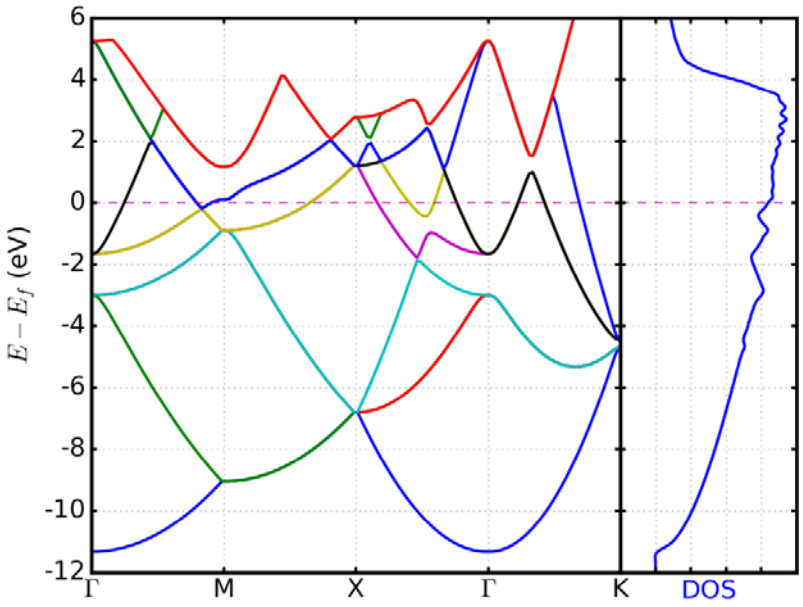

Figure 3.1 The electronic band structure of FCC aluminum (left) and the corresponding electron Density of State (right).

In Figure 3.1, Γ, M, X, K are the four highest symmetric points in the first Brillouin zone, as (0,0,0),(0.5,0,0),(0.5,0.5,0), and (0.5,0.5,0.5) respectively. The Fermi energy are set to be zero.

To gain more insight about the property-structure relationships, we also studied the partial electronic density of state, as illustrated in Figure 3.2. It clearly shows that the electrons on Fermi surface are mainly in p orbitals. Further study of the components of the p electrons of Al reveals that the pz electrons are dominant, which could be the key for its active chemical response.

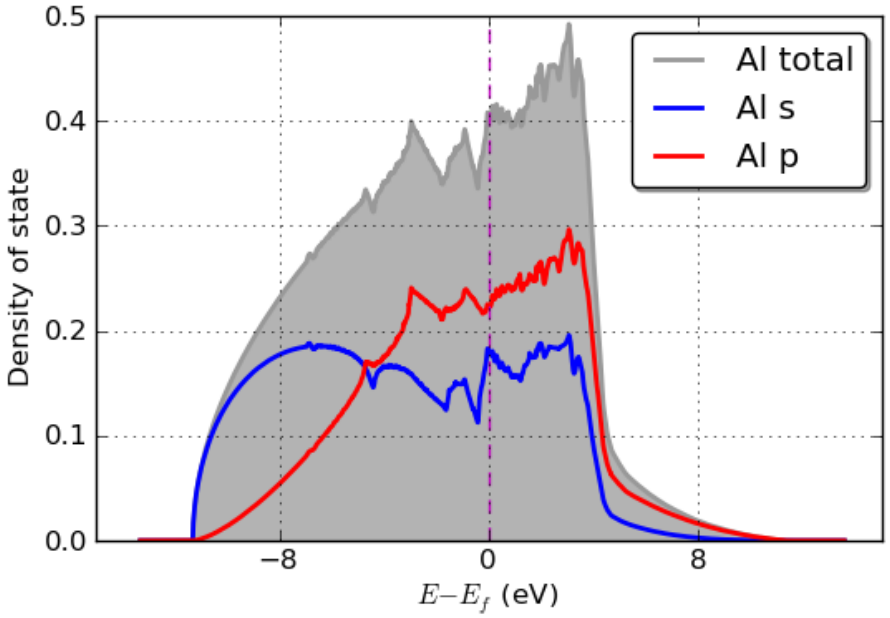

Figure 3.2: The projected electron density of state of Aluminum: Total (gray line), the s orbital (blue line) and the p orbital (red line).

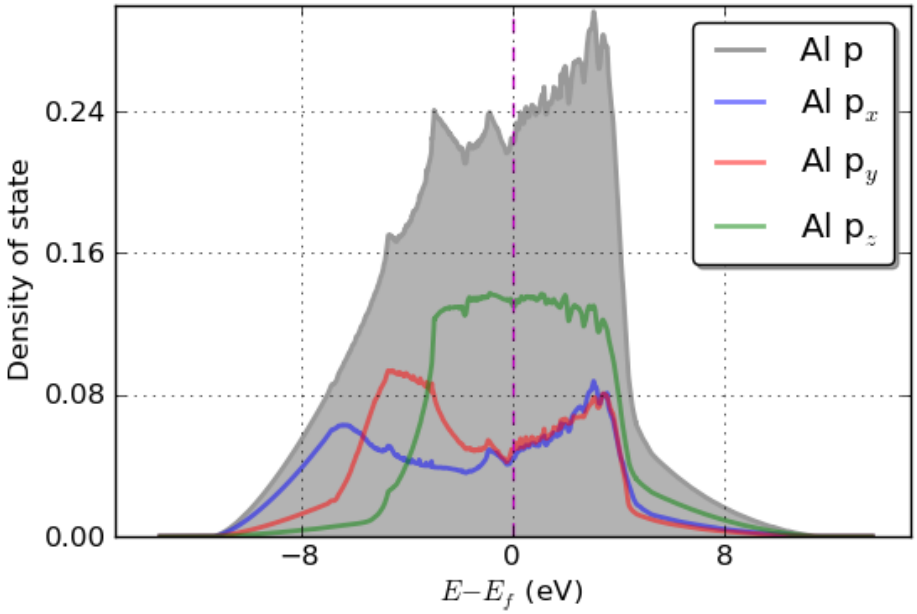

Figure 3.3 The projected electron density of state of p electrons in FCC Aluminum: Total p electrons and it its three components along x,y,z directions.

We next studied the equation of state of FCC aluminum. We isotopically apply external pressure on the simulation box. The corresponding energy and volume after fully relaxation then calculated from DFT. The internal energy as a function of volume is plotted in Figure 3.3. In addition, we fit the E-V curves using the third-order Birch-Murnaghan (BM3) isothermal equation of state, namely,

$$E(V) = E_0 + \frac{9V_0B_0}{16}\left\{\left[\left(\frac{V_0}{V}\right)^{2/3} - 1\right]3B_0' + \left[\left(\frac{V_0}{V}\right)^{2/3} - 1\right]2\left[6 - 4\left(\frac{V_0}{V}\right)^{2/3}\right]\right\} \quad \text{Eqn. 3.1}$$

The fitting parameters were the ground state free energy E_0, the unit cell volume per atom at zero pressure V_0, bulk modulus B_0, and B_0'—the pressure derivative of the bulk modulus at zero pressure. Our results are V_0=16.32 Å^3, bulk modules B_0= 75 GPa, B_0'=4.34, and $E_0 = -3.78$ eV per atom. Our results have good agreement with experimental values.

The unit cell volumes calculated at different pressures were used to generate P-V curves, which were fit with the third-order Birch-Murnaghan isothermal equation of state for pressure, namely,

$$P(V) = \frac{3B_0}{2}\left[\left(\frac{V_0}{V}\right)^{7/3} - \left(\frac{V_0}{V}\right)^{5/3}\right]\left\{1 + \frac{3}{4}(B_0' - 4)\left[\left(\frac{V_0}{V}\right)^{2/3} - 1\right]\right\} \quad \text{Eqn. 3.2}$$

The results of P-V curves and the fitting are shown in Figure 3.4.

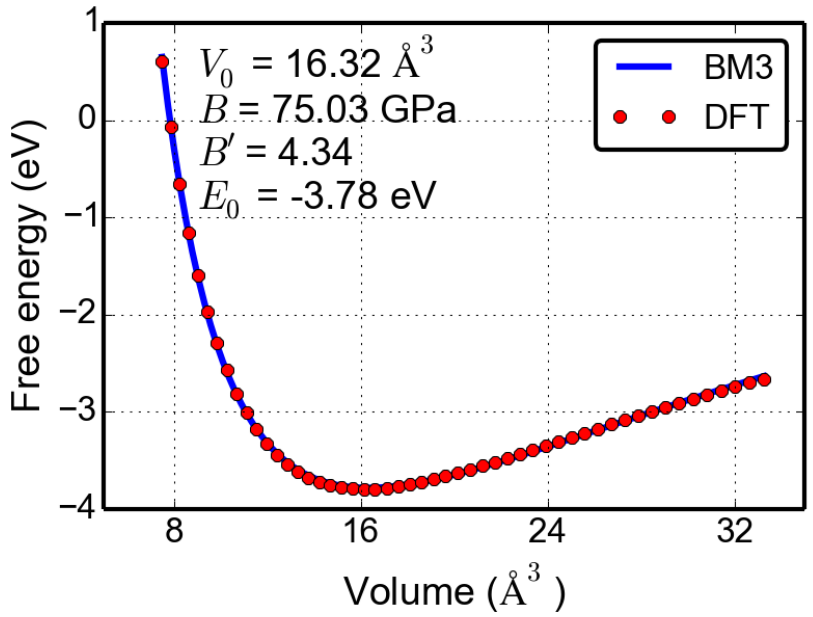

Figure 3.4 The free energy as a function of volume of Aluminum from first-principles calculations (red dots) are fitted with the third-order Birch-Murnaghan (BM3) isothermal equation of state.

In Figure 3.4, the fitting parameters are the ground state free energy E_0, the unit cell volume per atom at zero pressure V_0, bulk modulus B_0, and B_0'—the pressure derivative of the bulk modulus at zero pressure.

In Figure 3.5, the fitting parameters were the unit cell volume per atom at zero pressure V_0, bulk modulus B_0, and B_0'—the pressure derivative of the bulk modulus at zero pressure. The dashed vertical line denotes the position of unstrained state.

Under ambient condition, the Al powder or nanoparticles will have chemical reactions with oxygen in air and generate a thin layer of Al_2O_3 on the surface. This is a protective layer which prevent further oxidation of Al. So Al_2O_3 could be a considerable ingredient when the size of the Al powder is in nanometers. The knowledge of the mechanical properties, thermal properties, and chemical reactions related to Al_2O_3 are critical important for the understanding, design, and engineering the aluminized explosives. To that end, we have studied the structure, elastic properties, and electronic properties.

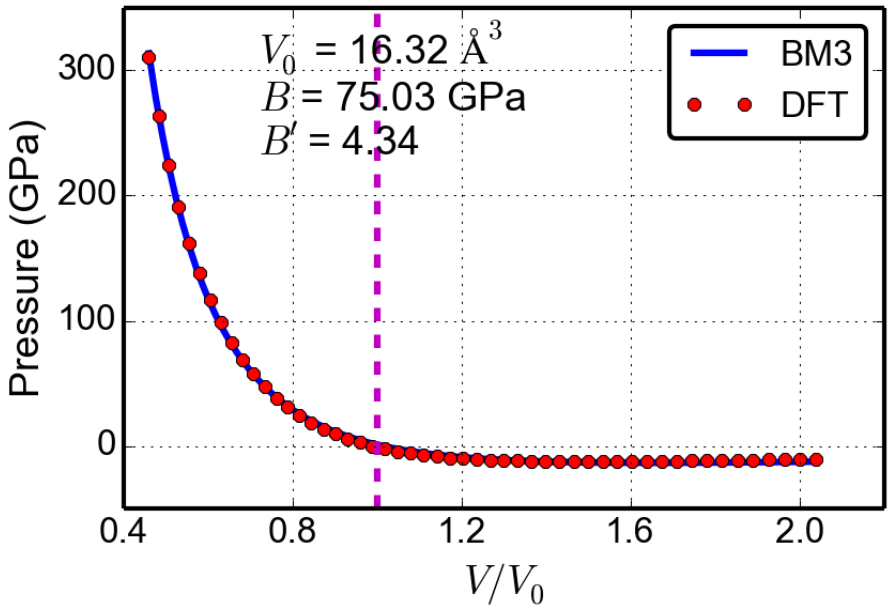

Figure 3.5: The pressure as a function of volumetric strain of aluminum from first-principles calculations (red dots) are fitted with the third-order Birch-Murnaghan (BM3) isothermal equation of state.

The alpha Al_2O_3 has a crystal structure of R-3c with space group number of 167. The conventional unit cell contains 12 Al atoms and 18 oxygen atoms. The full optimization of the geometry using PBEsol functionals reveals the lattice constants of a = 4.777 Å and c = 13.024 Å, agree well with experiment of a = 4.758 Å and c = 12.991 Å, respectively. The simulation cell with the atoms is displayed in Figure 3.6. The grey atoms are Al and the red atoms are oxygen.

In Figure 3.6, the crystal structure is R-3c with space group number of 167. The lattice constants are a = 4.777 Å and c = 13.024 Å predicted from PBEsol functions.

Then we isotopically apply external pressure on the simulation box. The corresponding energy and volume after fully relaxation then calculated from DFT. The internal energy as a function of volume is fitted the third-order Birch-Murnaghan (BM3) isothermal equation of state (Eqn. 3.1). The results are illustrated in Figure 3.7.

In Figure 3.7, the fitting parameters are the ground state free energy E_0, the unit cell volume per atom at zero pressure V_0, bulk modulus B_0, and B_0'—the pressure derivative of the bulk modulus at zero pressure.

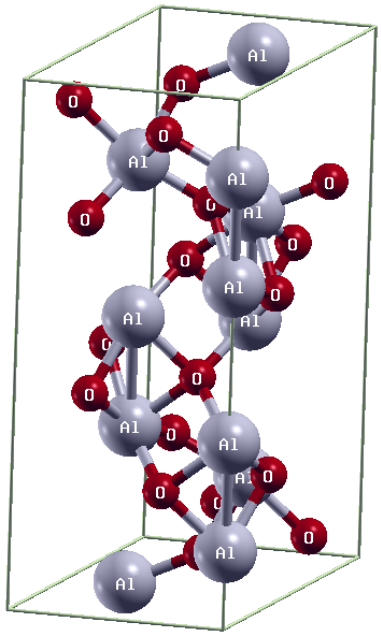

Figure 3.6: The conventional unit cell of the alpha-Al_2O_3 with 12 Al (grey) and 18 oxygen (red) atoms.

Our results are V_0=8.62 Å^3 per atom (which is 257.37 8.62 Å^3 per unit cell), bulk modules B_0= 224.09 GPa, B_0'=4.19, and $E_0 = -7.70$ eV per atom. The free energy is -231.0 eV per unit cell. Our results have good agreement with experimental values.

The heat of formation of Al_2O_3 can be calculated through the energy difference between the reactants and products, as H=E(Al2O3)-2E(Al)-1.5E(O2). At T=0K, the energy of Al E(Al)=-3.78 eV, the energy of Al2O3 is -38.5 eV, the O2 is -8.855 eV. The formation energy at zero K is -17.6575. Therefore, the heat of formation is 1703.7 kJ/mol.

The unit cell volumes calculated at different pressures were used to generate P-V curves, which were fit with the third-order Birch-Murnaghan isothermal equation of state for pressure (Eqn 3.2). The results are shown in Figure 3.8.

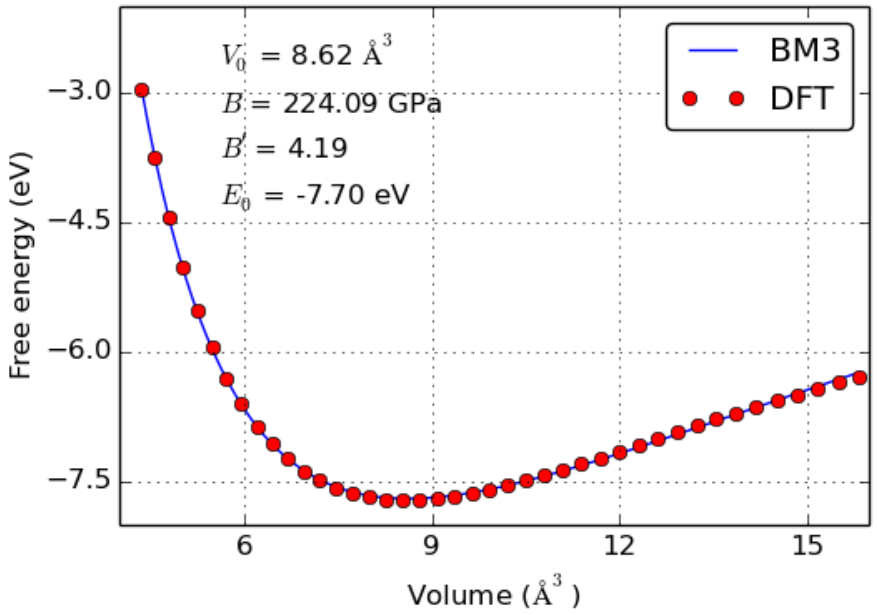

Figure 3.7: The free energy as a function of volume of alpha-Al_2O_3 from first-principles calculations (red dots) are fitted with the third-order Birch-Murnaghan (BM3) isothermal equation of state.

In Figure 3.8, the fitting parameters are the unit cell volume per atom at zero pressure V_0, bulk modulus B0, and B0' at zero pressure. The dashed vertical line denotes the position of unstrained state.

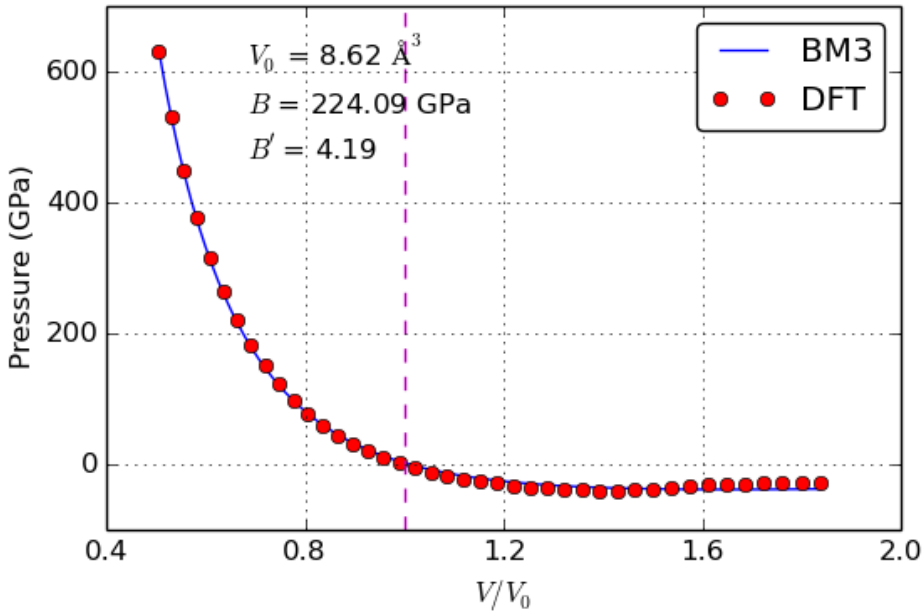

Figure 3.8: The pressure as a function of volumetric strain of alpha-Al2O3 from first-principles calculations (red dots) are fitted with the third-order Birch-Murnaghan (BM3) isothermal equation of state for pressure.

Chapter 4-Validation of the newly developed ReaxFF potential ReaxFF-d3

As a molecular crystal, the β-HMX need accurate energy formula to prescribe the van der Walls interactions between molecules which is critical in modeling the behaviors of this materials. There are extensive studies to improve the modeling of dispersion, or van der Waals (vdW) interactions [68], such as DFT-D [51, 55, 57, 60, 61], vdW-TS [59, 62], and vdW-DF [52, 63] methods. The DFT-D1 and DFT-D2 methods are classified as the 1st rung of Jacob's ladder for DFT-based dispersion correction schemes [68]. The DFT-D3 and vdW-TS methods belong to the second rung that utilizes environment dependent C6 corrections. Non-local density functionals like DFT-DF and DFT-DF2 methods sit in the 3rd rung [68], of which overall accuracy is expected to increase, as well as computational demand. Recently, a few improvements in vdW-DF methods have been proposed, including optPBE-vdW, optB88-vdW, optB86b-vdW [53, 117], vdW-DF2-C09 [54], vdW-DF-cx [118], and rev-vdW-DF2 [119]. These methods are designed to minimize the error of the binding energies, equilibrium separations, and interaction energy curves in the molecular duplexes in a certain collection of materials, such as the S22 data set [120], aiming for a general use for all materials. The accuracy of these models on energetic materials like HMX have been assessed. With the compromise the accuracy and the computational cost, we choose the vdW-D3 as the main functionals for out modeling of the HMX in density functional theory. The mechanical properties and equations of state were reported previously elsewhere by the authors.

As a second stage for bottom-up multiscale modeling, it is vital to pass the information from quantum mechanics electron level to molecular dynamics modeling in atomic level in a form of force field. In order to capture the fast chemical reactions and kinetics during the detonation, the reactive force fields are desirable. To that end, we adopted the ReaxFF potential as our target. A new set of ReaxFF potential was developed last year with the new training sets of HMX structures that are produced from vdW-D3 calculations. As a result, we denote this new set of ReaxFF potential for C-H-N-O systems as ReaxFF-D3.

We continued to validate ReaxFF-D3 by its performance in molecular dynamics simulations. We studied the thermal expansion coefficients of beta-HMX, as the experimental reference is available.

We study the volume change under conditions of NPT at temperature T ranged from 1K to 500K and the pressure of 1 atm (10^5 Pa). The time step in the MD simulations is 0.25fs. The simulations run for 20000 steps which is corresponding to 5ps. The system contains 14336 atoms which is 512 molecules, or 256 primitive unit cells. Such a large system is used for better statistics during MD simulations.

The results of our NPT simulations at varies temperatures are illustrated in Figure 4.1. The volume is for primitive unit cell that contains 56 atoms, or 2 molecules. We observed that the unit cell volume increases when the temperature increases. We fit the results of volumes as a function of temperature using

a quadratic function, $V = 0.000019734\,T^2 + 0.074236T + 503.254$ as displayed in the Figure 4.1. The thermal expansion then can be obtained by the definition.

$$\alpha = \frac{\partial \ln(V)}{\partial T} \qquad \text{Eqn. 4.1}$$

The thermal expansion then is plotted in the same figure to the right axis (Figure 4.1). Our results shows that the volume is 503.23 Å^3 and 527.28 Å^3 at T=0K and 300K respectively. The thermal expansion is 163.25×10^6 at 300K.

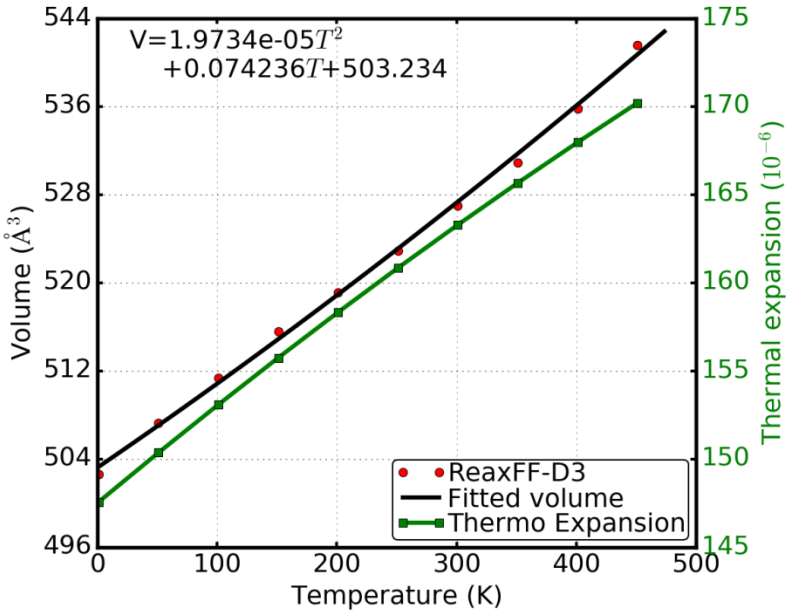

Figure 4.1: The volume as a function of temperature of β-HMX modeled in molecular dynamics using ReaxFF-D3 as potential.

It should be noted that in Figure 4.1, the function is fitted into a quadratic function. The thermal expansion is plotted to the right axis. The original data of volume is denoted by red dots.

As a comparison, we studied the same systems but with the ReaxFF-lg [19], the latest ReaxFF potentials come with LAMMPS. The NPT results of volumes as a function of temperature are plotted in Figure 4.2, including the thermal expansions. The ReaxFF.lg results show that the volume is 503.60 Å^3 and 527.52 Å^3 at T=0K and 300K respectively. The thermal expansion is 165.14×10^6 at 300K.

It should be noted that in Figure 4.2, the function is fitted into a quadratic function. The thermal expansion is plotted to the right axis. The original data of volume is denoted by red dots.

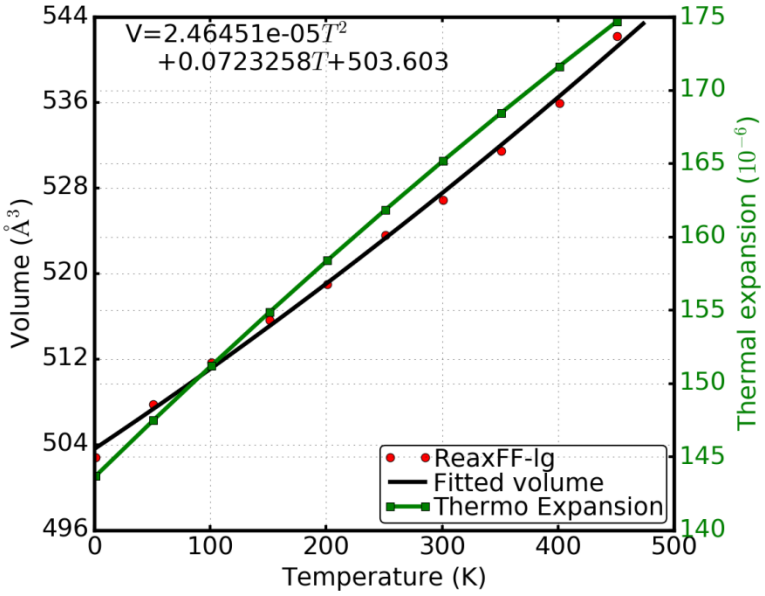

Figure 4.2 The volume as a function of temperature of β-HMX modeled in molecular dynamics using ReaxFF-lg as potential.

Experimentally, the thermal expansion of the beta-HMX was studied [50] in the temperature range of −150 to 30 °C. β-HMX is monoclinic (a = 6.5255(10) Å, b = 11.0369(18) Å, c = 7.3640(12) Å, and β = 102.67(1)°), space group P21/n. The results of the volumes at various temperature then plotted in the Figure 4.3. The volumes are also fitted into a quadratic function. The thermal expansion then obtained. In this way, we have the experimental values of volume which is 500.318 Å^3 and 516.984 Å^3 at T=0 and 300K, respectively. The thermal expansion at 300 is 139.066×10^6 at 300K.

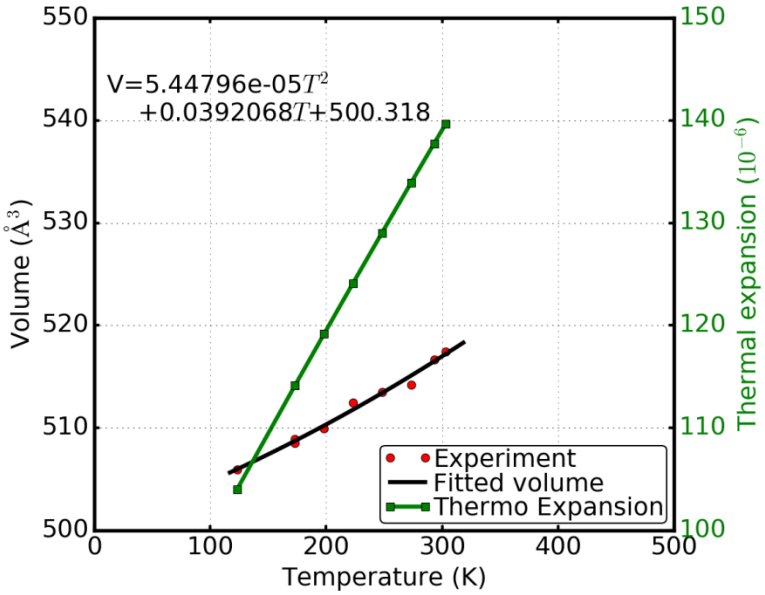

Figure 4.3: The volume as a function of temperature of β-HMX measured in experiment [50].

It should be noted that in Figure 4.3, the volume is fitted into a quadratic function. The thermal expansion were plotted to the right axis. The original data of volume is denoted by red dots.

Besides the thermal expansion, we studied the vibration frequencies of the beta-HMX crystals at finite temperature. In general, Vibrational spectroscopy is a sensitive probe of the atomic structure and of the chemical bonding and thus of the electronic structure. In this study, the phonon density of states (PDOS) has been studied at T=300K using both ReaxFF-D3 and ReaxFF-lg potentials for better comparison. The PDOS is calculated from the Fourier transform of the velocity autocorrelation function [121], as

$$\mathrm{PDOS}(\omega)=\frac{1}{\sqrt{2\pi}}\int e^{-i\omega t}\langle\sum_{j=1}^{N} v_j(t)v_j(0)\rangle dt \qquad \text{Eqn. 4.2}$$

where $v_j(0)$ is the average velocity vector of a particle j at initial time, $v_j(t)$ is its velocity at time t, and ω is the vibration wave number. N is the number of atoms in the system. Our results are plotted in the Figure 4.4.

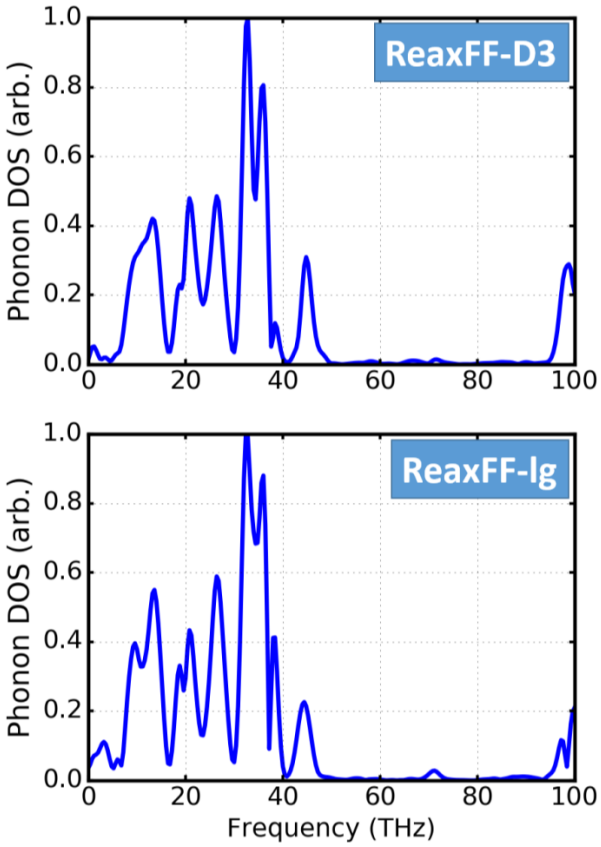

Figure 4.4 The phonon density of states of β-HMX at 300K predicted by ReaxFF-D3 (top) and ReaxFF-lg (bottom) potentials.

It can be seen that the main frequencies are represented and similar in both potentials. For example, the largest frequency goes up to 97.2 THz or 3243 cm^{-1}. This is the typical vibration of hybridized C-H bonds. The nitro groups (-NO2) has vibration frequency of 1550 cm^{-1} or 46.5 THz are also captured.

Chapter 5-QM study of the stabilities, mechanical properties and equations of state of Iron under extreme conditions

Iron is one of the most important metals in everyday life. It is the most common element in the whole planet Earth, forming much of Earth's outer and inner core. Iron is the mostly used metal case for explosives. To have better description of the performance of detonation within a metal case, we need to have better understand of the stabilities, mechanical properties, thermal properties, and equations of state of Iron under extreme conditions.

The thermal properties of solids at constant volume can be calculated from their phonon density of states as a func- tion of frequencies. The phonon contribution to the Helmholtz free energy F A is given by:

$$F_A = \frac{1}{2}\sum_{q,v} \hbar\omega_{q,v} + k_B T \sum_{q,v} \ln[1 - e^{-\frac{\hbar\omega_{q,v}}{k_B T}}] \quad \text{Eqn. 5.1}$$

where k_B and ħ are the Boltzmann constant and the reduced Planck constant, respectively, q and ν are the wave vector and band index, respectively, $\omega_{q,v}$ is the phonon frequency at q and ν, and T is the temperature.

The heat capacity at constant volume C_V and the entropy S at constant volume are given by the following formula:

$$C_V = \frac{1}{2}\sum_{q,v} k_B \left(\frac{\hbar\omega_{q,v}}{k_B T}\right)^2 + \frac{e^{-\frac{\hbar\omega_{q,v}}{k_B T}}}{\left(e^{-\frac{\hbar\omega_{q,v}}{k_B T}} - 1\right)^2} \quad \text{Eqn. 5.2}$$

$$S = -k_B \sum_{q,v} \ln\left[1 - e^{-\frac{\hbar\omega_{q,v}}{k_B T}}\right] - \frac{1}{T}\frac{\hbar\omega_{q,v}}{e^{-\frac{\hbar\omega_{q,v}}{k_B T}} - 1} \quad \text{Eqn. 5.3}$$

In practical, thermodynamical problems related to solids, the thermal properties need to be known at constant pressure. They can be calculated from the previous quantities through thermodynamic relationship. The Gibbs free energy G may be written as

$$G(T,P) = \min_V [U(V) + F_A(F,V) + PV] \quad \text{Eqn. 5.4}$$

where V and P are the volume and the pressure, respectively. $U(V)$ is the total energy of electronic structure at constant volume. The right-hand side of Eq. 4 means the function inside the square brackets is minimized with respect to the volume at each couple of T and p variables.

The heat capacity at constant pressure Cp is derived from G(T, p) by

$$C_p = -T\,\frac{\partial^2 G(T,P)}{\partial T^2} = T\,\frac{\partial V(T,P)}{\partial T}\frac{\partial S(T,V)}{\partial V}\Big|_{V=V(T,P)} + C_V\big(T, V(T,P)\big) \quad \text{Eqn. 5.5}$$

where $V(T,P)$ is the equilibrium volume at temperature T and P.

We have employed quasiharmonic approximation (QHA) to calculate the thermal properties at constant pressure. $U(V)$ and $F_A(T,V)$ were calculated at 11 volume points, from -15% to +15% of volume change around the equilibrium. The corresponding pressure is ranged from 42.6 GPa to -17.9 GPa.

The thermodynamic functions were fitted to the integral form of the Vinet equation of state [99] (EOS) at p = 0. Gibbs free energies at finite temperatures were obtained as the minimum values of the thermodynamic functions, and the corresponding equilibrium volumes and isothermal bulk moduli were obtained simultaneously from the Vinet EOS. Unit cells used to calculate $U(V)$ and $F_A(T,V)$ were relaxed by the first-principles calculation under the hydrostatic-stress conditions. These procedures applied for bcc iron are demonstrated in Figure 5.1, where $U(V) + F_A(T,V)$) as a function of unit-cell volume at temperatures are shown.

The C_P of bcc iron as a function of temperature obtained from the quasi-harmonic approximation are shown in Figure 5.2, ranging from 0 to 2000K. Please keep in mind that the melting temperature of iron is 1800K. The crystal structure might not be stable.

The free energy, entropy, and heat capacity at constant volume C_V as a function of temperature of BCC iron from QHA are obtained and plotted in Figure 5.3.

The phonon band structure of BCC iron under pressure of 0 GPa and 43 GPa are plotted in Figure 5.4. There is negative frequency at high pressure of 43 GPa, which indicates the instability of BCC iron under such pressure. In fact, there is a phase change from BCC structure to HCP structure. At pressures above approximately 10 GPa and temperatures of a few hundred kelvin or less, α-iron changes into a hexagonal close-packed (hcp) structure, which is also known as ε-iron or hexaferrum.

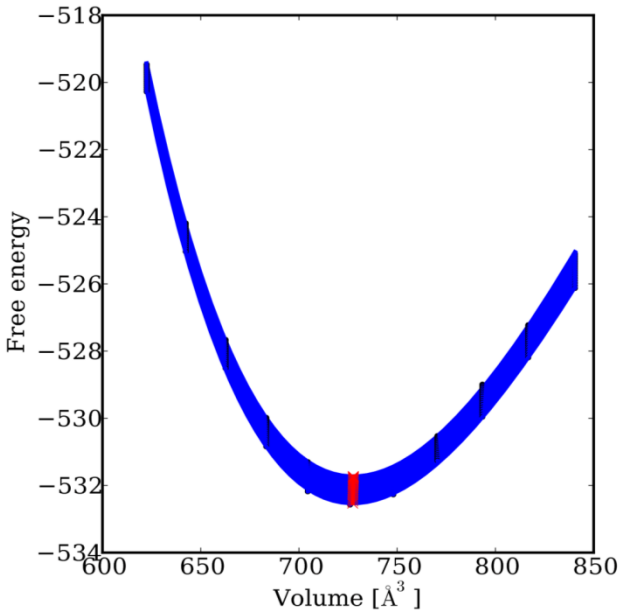

Figure 5.1: $U(V) + F_A(T,V)$ as a function of unit-cell volume of bcc iron.

In Figure 5.1, the solid curves show the fitted thermodynamic functions. The minimum values of the fitted thermodynamic functions at temperatures are depicted by the crosses. The dashed curve passing through the crosses is guide to the eye.

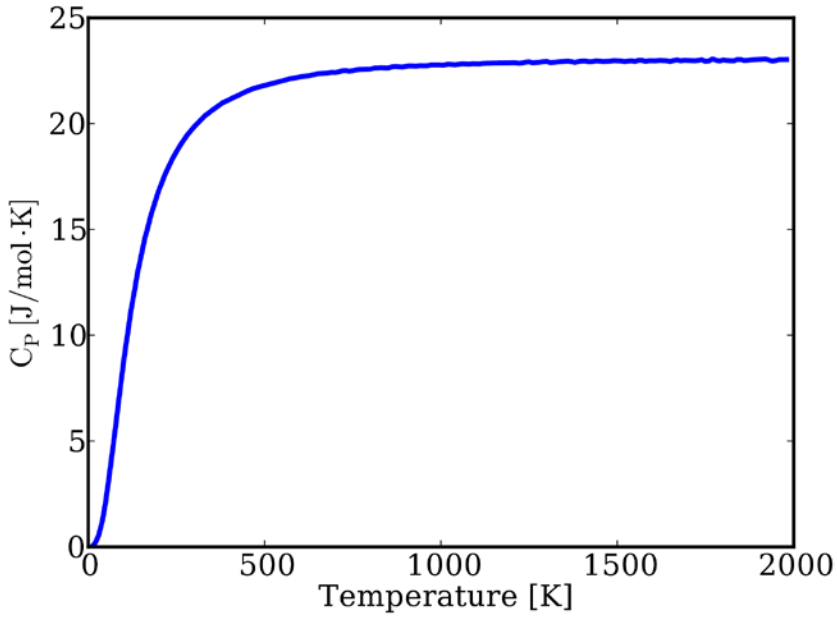

Figure 5.2 The C_P of bcc iron as a function of temperature obtained from the quasi-harmonic approximation.

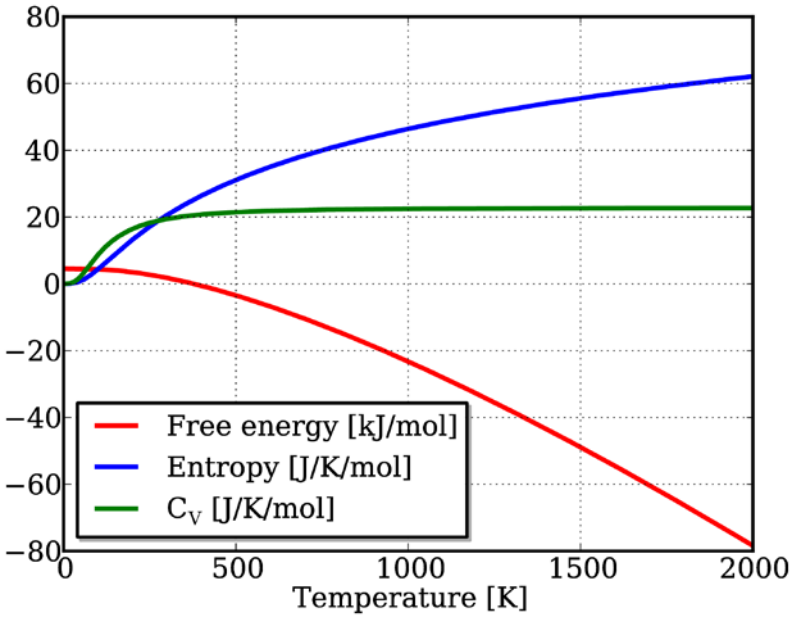

Figure 5.3 The free energy, entropy, and heat capacity at constant volume C_V as a function of temperature of BCC iron from QHA.

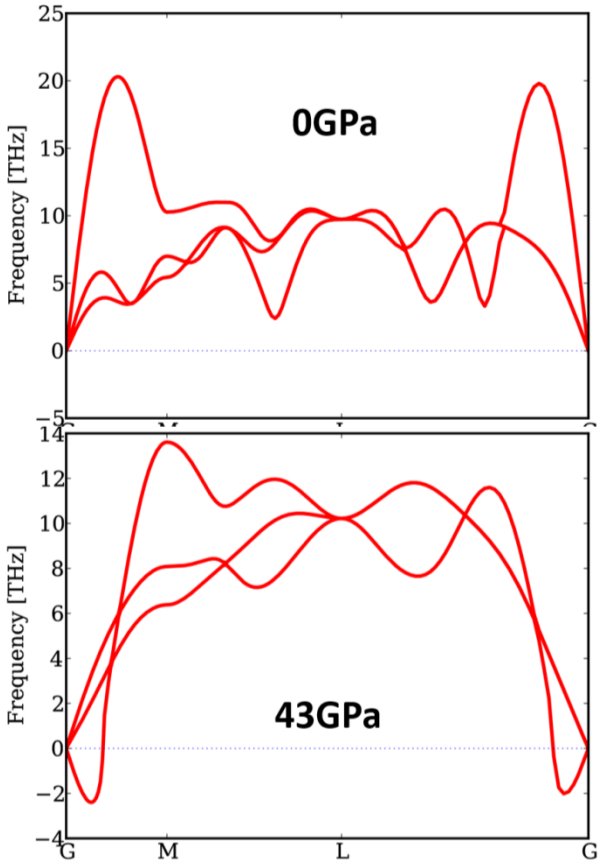

Figure 5.4 Phonon band structure of BCC iron under pressure of 0 GPa (top) and 43 GPa (bottom).

There is negative frequency at high pressure of 43 GPa, which indicates the instability of BCC iron under such pressure.

Chapter 6-Molecular dynamics (MD) simulation using LAMMPS

6.1 Hugoniot EoS of solid HMX

The Hugoniot EoS describes the locus of thermodynamic states of solid high explosives after a shock passing through. It can be derived from the conservation of mass, momentum, and energy, known as Rankine-Hugoniot conditions [122]:

$$\rho_1 u_s = \rho_2 (u_s - u_2) \quad \text{Conservation of mass} \quad \text{Eqn. 6.1}$$

$$p_2 - p_1 = \rho_2 u_2 (u_s - u_2) = \rho_1 u_s u_2 \quad \text{Conservation of momentum} \quad \text{Eqn. 6.2}$$

$$p_2 u_2 = \rho_1 u_s (\frac{1}{2} u_2^2 + E_2 - E_1) \quad \text{Conservation of energy} \quad \text{Eqn. 6.3}$$

where u_s is the shock wave speed, ρ_2 and ρ_1 are the density of material behind and in front of the shock, u_2 is the particle velocity of the material behind the shock, p_2 and p_1 are the pressure of the material behind and in front of the shock, and E_2 and E_1 are the specific internal energies in the two regions.

Based on Rankine-Hugoniot conditions, the following relations can be obtained:

$$\frac{u_2}{u_s} = 1 - \frac{v_2}{v_1} \quad \text{Eqn. 6.4}$$

$$u_s = \sqrt{\frac{p_2 - p_1}{v_1 - v_2}} v_1 \quad \text{Eqn. 6.5}$$

$$u_2 = \sqrt{(p_2 - p_1)(v_1 - v_2)} \quad \text{Eqn. 6.6}$$

$$E_2 - E_1 = \frac{1}{2}(p_2 + p_1)\left(\frac{1}{\rho_1} - \frac{1}{\rho_2}\right) = \frac{1}{2}(p_2 + p_1)(v_1 - v_2) \quad \text{Eqn. 6.7}$$

where v_2 and v_1 are the specific volumes of the material behind and in front of the shock.

The parameters of the JWL EoS of solid PBX 9501 are listed in Table 6.1 [24]. PBX 9501 is chosen because it consists of 95 weight % HMX, 2.5 weight % estane binder, and 2.5 weight % BDNPA/F.

Table 6.1 Parameters of JWL EoS of solid PBX 9501 [24]

$A\ (GPa)$	$B\ (GPa)$	r_1	r_2	ω	$C_V (J/(Kg \cdot K))$	$T_0\ (K)$
732000	-5.2654	14.1	1.41	0.8867	2.7806×10^6	298

6.2 JWL EoS of gaseous products of HMX

The expansion of detonation products of high explosives is considered an isentropic process. It includes complicated chemical reactions, occurring in very short time. Cylinder test has long been the principal method to obtain the data needed for fitting parameters of the JWL EoS of explosive detonation products [17]. It consists of detonating a cylinder of explosive confined by copper and measuring the velocity of the expanding copper wall. The standard tube has a 1-inch internal diameter, 0.1 in copper wall, and is 12 in long. The configuration of cylinder test is shown in Figure 6.1.

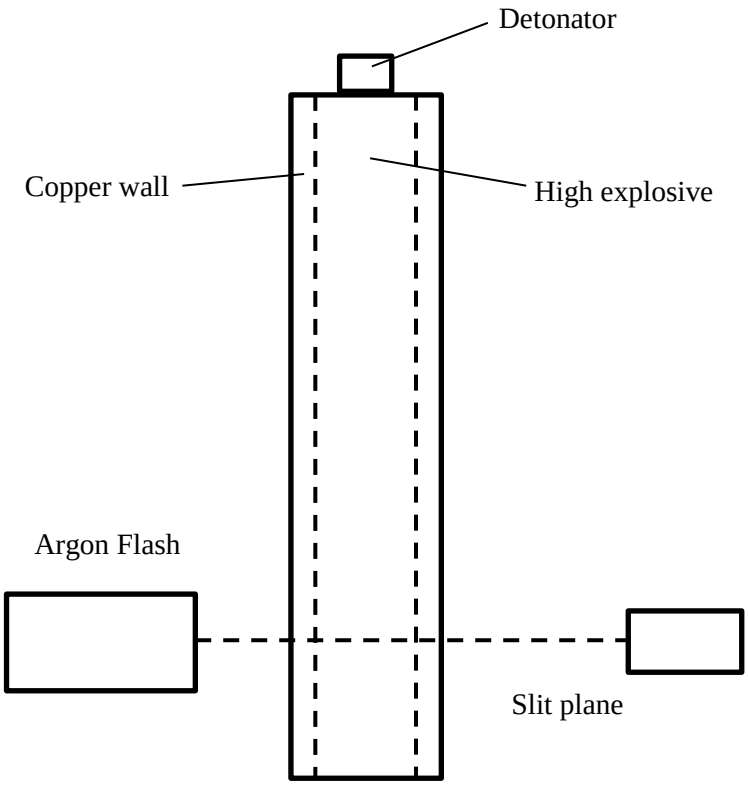

6.1 Configuration of cylinder test

The parameters of the JWL EoS of gaseous products of PBX 9501 are listed in Table 6.2 [24].

Table 6.2 Parameters of JWL EoS of gaseous products of PBX 9501

$A\ (GPa)$	$B\ (GPa)$	r_1	r_2	ω	$C_V(J/(Kg\cdot K))$	$T_0\ (K)$
1668.9	59.69	5.9	2.1	0.45	1.0×10^6	298

6.3 Structure and relaxation of β−HMX using LAMMPS

We focus on the β-HMX (octahydro-1,3,5,7-tetranitro-1,3,5,7-tetrazocine), a typical secondary explosive with chemical formula of $C_4H_8N_8O_8$. The geometry of the primitive unit cell of the β-HMX is shown in Figure 6.2(a) with the cell box, which is obtained from our previous DFT-D2 study [23]. The β-HMX is a P21/c monoclinic crystal with space group number 14. The lattice parameters are listed in Table 2.1. Replication of the primitive unit cell of HMX is shown in Figure 6.2(b), (a), where C, H, O, and N atoms are represented by yellow, aqua, red, and grey balls, respectively. We tested three different systems with 4x2x4, 5x3x5, and 8x5x7 primitive unit cells, with 1792, 4200, and 15680 atoms, respectively and it is found that the results converge at the system with 1792 atoms. Therefore, we report our results from the simulation cells with 1792 atoms as depicted in Figure 6.2(b).

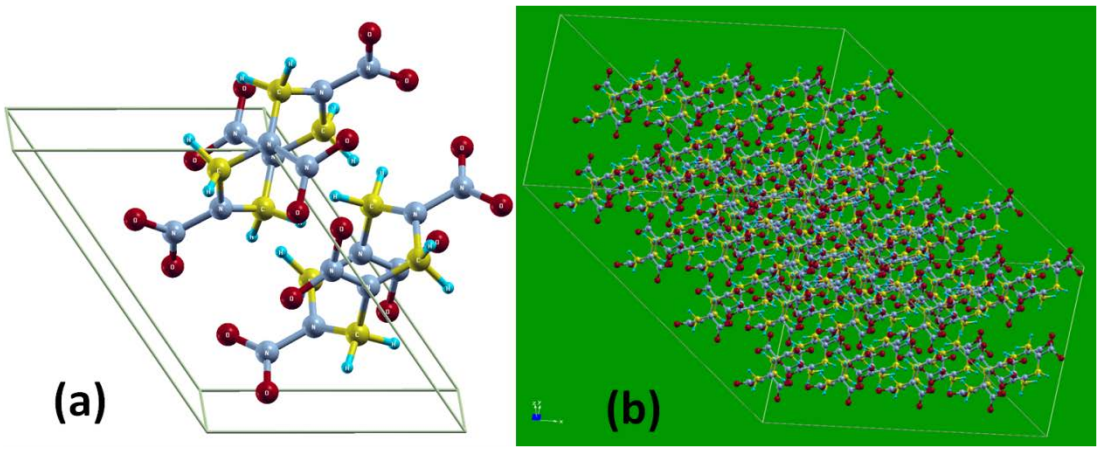

Figure 6.2 Simulation cells and geometry of β-HMX

The structure of β-HMX at $0K$ was obtained from our previous DFT-D2 calculations [23]. The system which contains 1792 atoms is relaxed using the NPT (constant atom number N, pressure P, temperature T), NVT (constant atom number N, volume V, temperature T), and NVE (constant atom number N, volume V, energy E) ensembles successively with ReaxFF-d3. Due to the inadequate consideration of van der Waals (vdW) attractions, when using original ReaxFF to relax the solid molecule, the equilibrium volume will be 10~15% higher than experiment [19]. This disadvantage is overcome by ReaxFF-lg (and ReaxFF-d3), which gives sufficient consideration of vdW interactions in its description of reactive force fields. In the structural of relaxation, the time step is set to be 0.25 fs while the simulation time is set to be 50 ps for each ensemble.

The lattice constants for the unit cell of β-HMX from experiment [88], DFT-D2 [23] studies are listed in Table 6.3.

Table 6.3 Lattice constants of β-HMX from experiment [88], DFT-D2 calculations [23]

	a (Å)	b (Å)	c (Å)	α	β	γ
Experiment[88]	6.54	11.05	8.70	90	124.30	90
DFT-D2[23]	6.542	10.842	8.745	90	124.41	90

The supercell of β-HMX consists of 64 β-HMX molecules, which contains 1792 atoms in total. The density of β-HMX before relaxation is 1891.8 $/m^3$. Three ensembles (NPT, NVT, NVE) are used sequentially to relax the system. Each ensemble takes 50 ps. The variation of volume, total energy, temperature and pressure of the system during relaxation is shown in Figure 6.3.

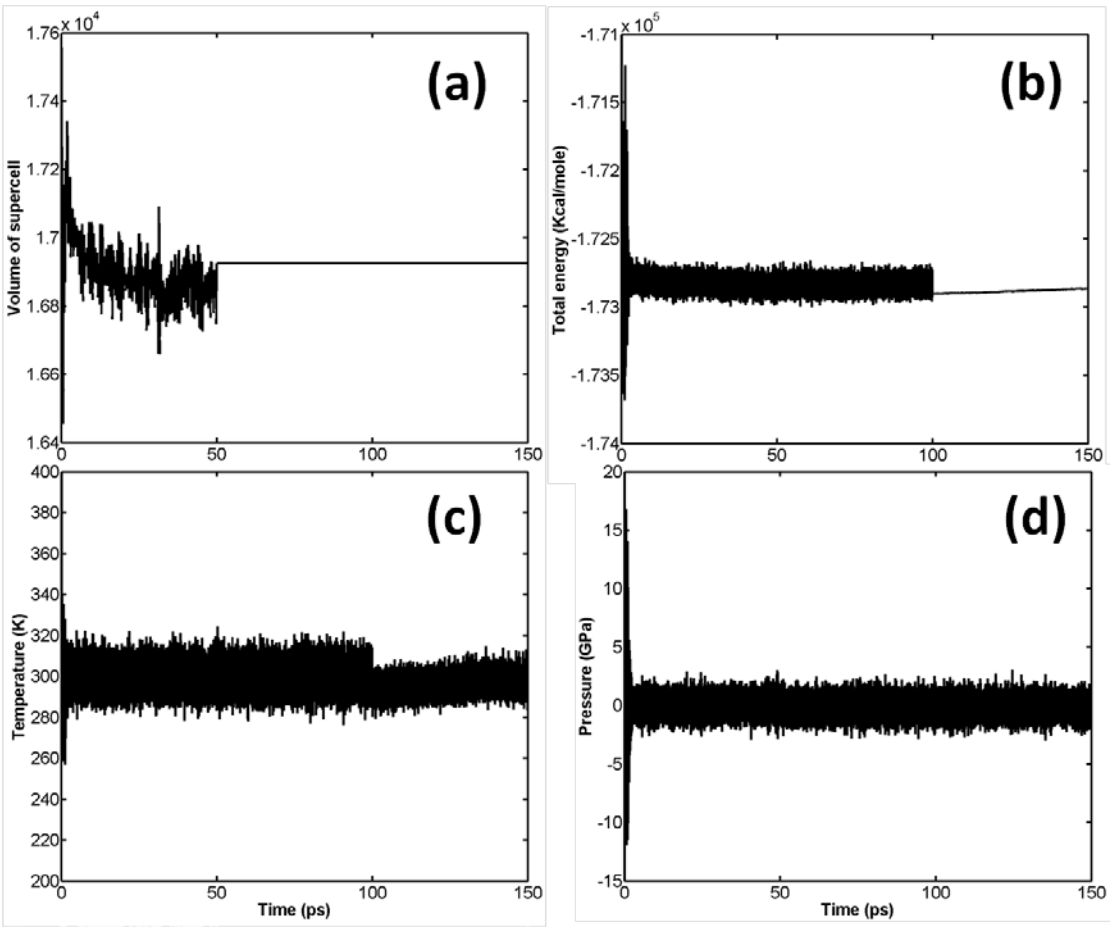

Figure 6.3 Variation of volume (a), total energy (b), temperature (c), and pressure (d) of β-HMX system during the geometry relaxation at the temperature of 300 *K* in MD simulations.

It is well known that β-HMX is very sensitive to fluctuations in temperature. It will transform from β-HMX to δ-HMX above 436K [123]. Therefore, it is necessary to control temperature fluctuations to prevent phase transformation. It can be seen from Figure 6.3(c) that, during the relaxation, the temperature is limited to around 300*K*, which ensures no phase transformation during relaxation. According to Figure 6.3(a), the volume of the supercell fluctuates significantly in the NPT stage, and the maximum volume of the supercell reaches 17558.66 $Å^3$. In the successive NVT and NVE stages, the volume stabilizes at 16924.73 $Å^3$ (or 528.9 $Å^3$ per primitive unit cell). After relaxation, the density of β-HMX is 1858.7 kg/m^3, which is very close to the experimental value (1838.0 kg/m^3) at ambient temperature. According to Figure 6.3(d), after the initial fluctuation, the pressure of the system fluctuates around 0 GPa.

6.4 Calculation of JWL EoS of solid β-HMX using LAMMPS

The JWL EoS of solid β-HMX is obtained through a series of NVT simulations using LAMMPS with ReaxFF-d3. NVT is preferred because as mentioned in section above, in ignition and growth model,

temperature is introduced in the JWL EoS of solid explosive. According to Yoo [16], the pressure-volume relation calculated under hydrostatic conditions is in good agreement with Hugoniot curve. The simulation scheme is as follows: compress the β-HMX along a-direction of the supercell to predefined volume and temperature, thus, for each set of volume and temperature, there is a corresponding pressure. In the implementation of NVT simulation, the time step is set to be 0.1 *fs* and the total simulation time is set to be 15 *ps*. The variation of volume, total energy, temperature and pressure of the supercell is shown in Figure 6.4, where the compression direction is a-direction of the supercell and the predefined volume ratio is 0.5 (compress the volume to 0.5 its original volume V_0) while the predefined temperature is 300 *K*.

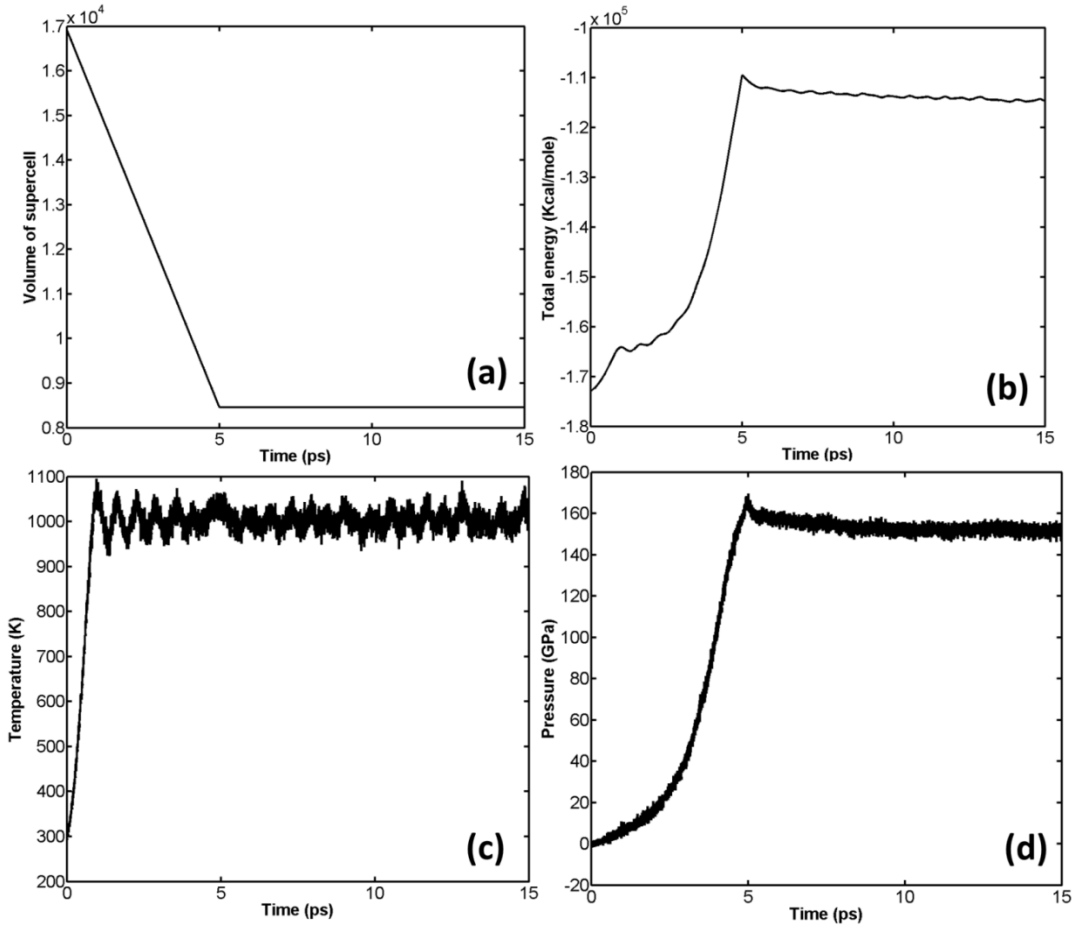

Figure 6.4 Variation of volume (a), total energy (b), temperature (c), and pressure (d) of β-HMX under compression at T=1000K, $\frac{V}{V_0} = 0.5$.

The comparison of the EoS calculated by MD with that obtained from experiment [16], and JWL EoS of solid PBX 9501 [24] is shown in Figure 6.5, where x-axis represents volume ratio, y-axis represents the pressure of the supercell of β-HMX mentioned above. It should be noted that the experiment was performed at room temperature and the JWL EoS of solid β-HMX obtained by MD is calculated at 300 *K*.

.

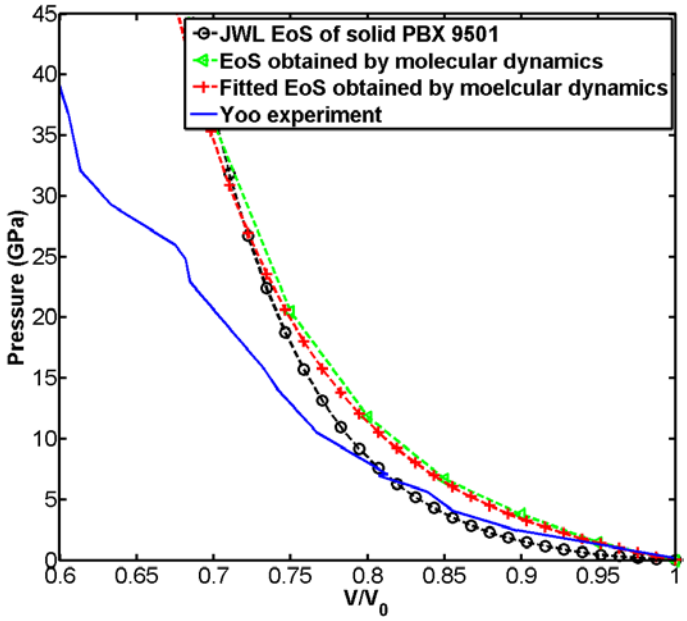

Figure 6.5 Comparison of the EoS calculated by MD with that obtained from Yoo's experiment and JWL EoS of solid PBX 9501

It can be seen from Figure 6.5 that the EoSs, either EoS obtained from MD simulation or EoS of solid PBX 9501, do not agree well with Yoo's experiment. The EoS calculated by MD is close to Yoo's experiment at high volume ratio (greater than 0.97). However, it gradually deviates from experiment when the system is further compressed. The EoS calculated by MD is greater than EoS of solid PBX 9501 when volume ratio is greater than 0.725. When volume ratio is smaller than 0.725, the case is opposite. It is probably because that PBX 9501 contains 95% HMX and 5% other materials (whose density is around 1050 Kg/m^3, smaller than the density of HMX, which is 1910 Kg/m^3) .

The parameters of JWL EoS of solid PBX 9501 [24] and fitted parameters of EoS of solid β-HMX obtained from MD simulation are listed in Table 6.4.

Table 6.4 Parameters of JWL EoS of solid PBX 9501 [24] and fitted parameters of EoS of solid β-HMX obtained from MD

	$A_s\ (GPa)$	$B_s\ (GPa)$	r_{1s}	r_{2s}	ω_s	$T_0\ (K)$
JWL EoS of solid PBX 9501 [24]	732000	-5.2654	14.1	1.41	0.8867	298
Fitted EoS of solid β-HMX	129230	-0.3678	11.8767	-2.4892	4.2431	300

6.5 Calculation of JWL EoS of gaseous products of β-HMX using LAMMPS

Similar to the calculation of JWL EoS of solid β-HMX, the JWL EoS of gaseous products of β-HMX was also obtained through NVT simulations using LAMMPS with ReaxFF-d3. Prior to the NVT simulation, NPHUG is used to compress the system to around 64 GPa. NPHUG performs a time integration of the Hugoniotstat equations of motion developed by Ravelo et al. [122]. Then, the system is dilated from compressed state. The simulation scheme is: expand the β-HMX along a-direction of the supercell to a predefined volume and temperature, thus, for each set of volume and temperature, there is a corresponding pressure. The time step is set to be 0.1 *fs* and the total simulation time is set to be 15 *ps*. The variation of volume, total energy, temperature and pressure of the supercell is shown in Figure 6.6, where the predefined volume ratio is 4 (expand the volume to 4 times its compressed volume V_c), and the predefined temperature is 3000*K*.

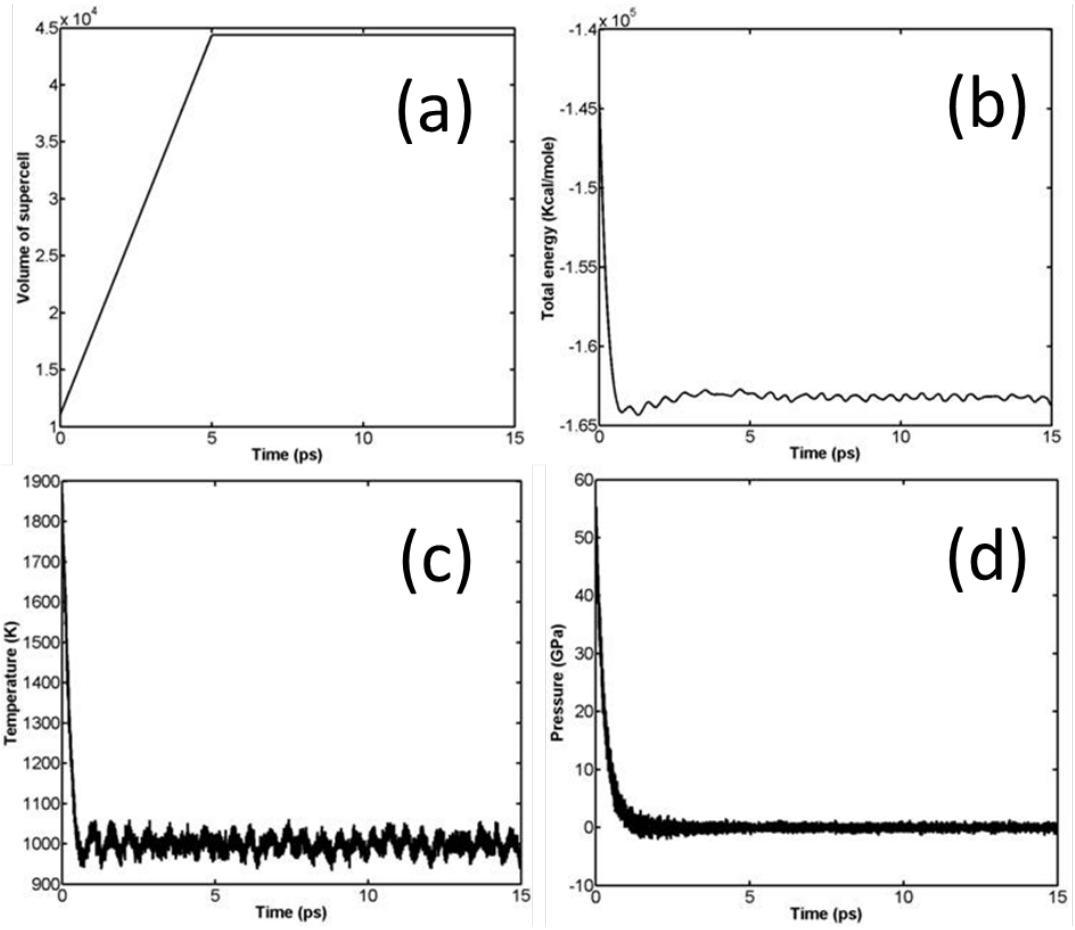

Figure 6.6 Variation of volume (a), total energy (b), temperature (c), and pressure (d) of β-HMX in NVT expansion, T=1000K, $\frac{V}{V_c} = 4.0$.

The comparison of JWL EoS of gaseous products of β-HMX obtained through MD with JWL EoS of PBX 9501 is shown in Figure 6.7, where x-axis represents volume ratio, y-axis represents the pressure of the supercell of β-HMX mentioned above. Temperature is set to be 3000 K, which is close to the temperature of PBX 9501 at CJ state.

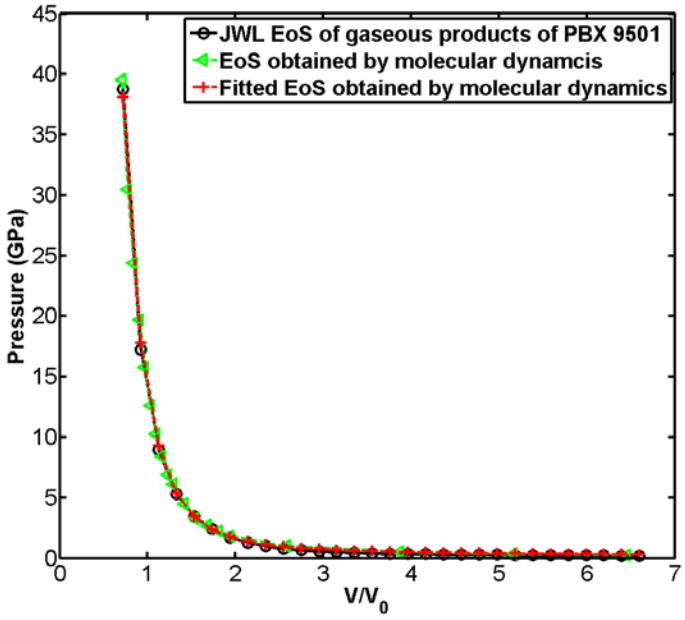

Figure 6.7 Comparison of JWL EoS of gaseous products of β-HMX with JWL EoS of PBX 9501.

It can be seen from Figure 6.7 that the EoS calculated via MD agrees very well with JWL EoS of gaseous products of PBX 9501 in ignition and growth model.

The parameters of the JWL EoS of gaseous products of PBX 9501 [24] and fitted parameters of EoS of β-HMX obtained from MD simulation are listed in Table 6.5.

Table 6.5 Parameters of the JWL EoS of gaseous products of PBX 9501 [24] and fitted parameters of EoS of β-HMX obtained from molecular dynamics

	$A_g\ (GPa)$	$B_g\ (GPa)$	r_{1g}	r_{2g}	ω_g	$T_0\ (K)$
EoS of gaseous products of PBX 9501	1668.9	59.69	5.9	2.1	0.45	3000
Fitted parameters of EoS of gaseous products of β-HMX	1015	85.1	5.35	2.53	0.7041	3000

Chapter 7-QM-MD-SPH simulation of energetic materials

7.1 Shock wave and detonation model

Generally, explosive can be categorized into two classes [124]: low and high explosive. Low explosives are often used as propellants in rocket motors and fireworks. When detonated, the chemical reaction in low explosive will produce a sub-sonic deflagration wave. In contrast to low explosive, the chemical reaction in high explosive will generate a super-sonic detonation wave. According to the constituents, high explosive can be further classified to homogeneous explosive and heterogeneous explosive. Homogeneous explosive has a uniform composition, such as liquid nitromethane [125]. Heterogeneous explosive consists of poly crystalline materials containing voids of various shapes and sizes, defect structure and small amount of polymeric binders and plasticizers [126].

High explosive can be detonated by purpose-built detonators [2] or by high-velocity impact in accidental scenarios or experimental configuration. The shock initiation of heterogeneous explosive is a complicated process which is still not thoroughly understood. HMX is used as a component of plastic-bonded explosive (such as PBX 9501), which is a typical heterogeneous explosive, as shown in Figure 7.1 [127]. It shows PBX 9501 is a mixture of coarse and fine HMX crystal with diameters between 1 and 1000 μm, which are bound together by polymers.

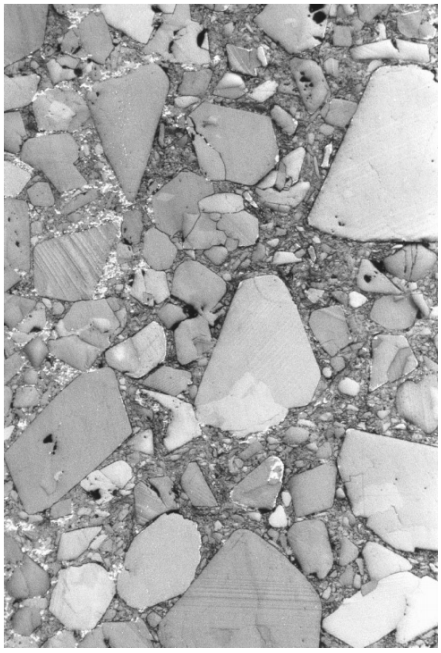

Figure 7.1 Micrograph of PBX 9501

When a shock wave travels through heterogeneous explosive, it provides heating by bulk compression and by interaction with density discontinuity (such as voids) and defect structure, known as hot spots [128]. On appropriate condition, these hot spots may begin to react and spread into surrounding explosive. Growing chemical reactions behind the shock front raise pressure and temperature and finally lead to

stable detonation. This is the mesoscale mechanism of detonation of heterogeneous explosives by shock, as shown in Figure 7.2. According to Field et al. [129], the size of hot spot ranges from 0.1-10 μm.

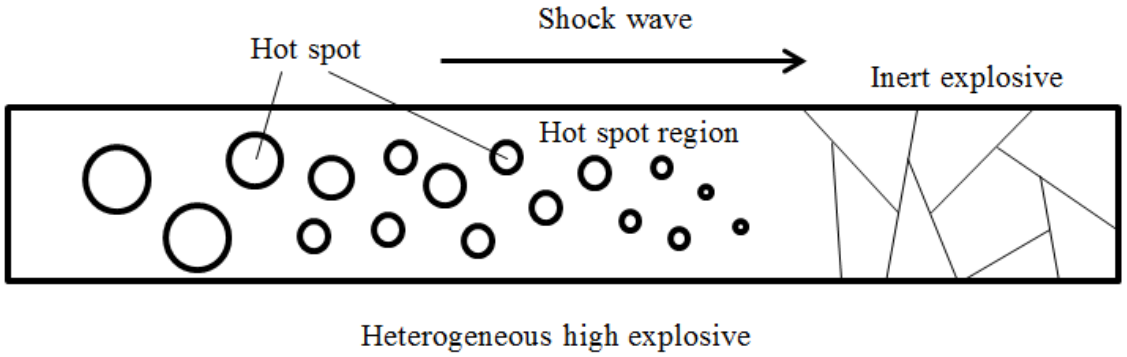

Figure 7.2 Scheme of hot spots formation

It is generally accepted that the initiation of detonation of heterogeneous explosives by shock can be divided into two distinct stages [128]:

(I) Ignition of a small fraction of the explosive at random sites (zone where strong shock wave passes by) due to the creation of hot spots.

(II) Growth to detonation from the coalescence of the energy released from individual hot spots.

To numerically simulate the shock initiation of high explosive in macroscopic scale, appropriate models need to be established.

A classic one-dimensional Zeldovich-von Neumann-Döring (ZND) detonation model is often used to describe the detonation of heterogeneous high explosive by shock wave [130-132], as shown in Figure 7.3: first, an infinitely thin shock wave travelling at subsonic speed compresses the explosive to a high pressure called von Neumann spike. The sudden change in pressure initiate the chemical energy release. Then, the energy release accelerates the flow behind the spike to local speed of sound, which is known as CJ state. After CJ point, the detonation products expand backward and form a rarefaction wave.

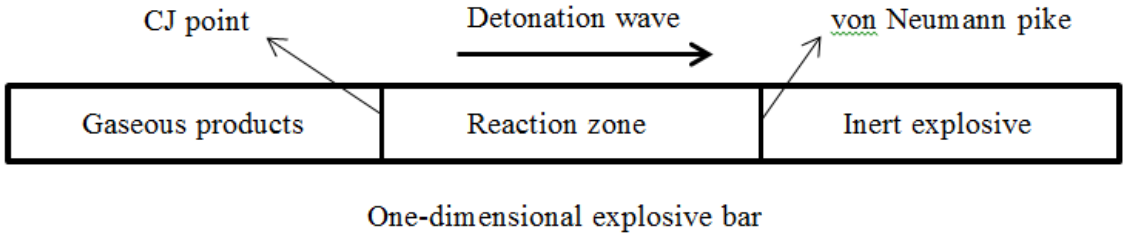

Figure 7.3 Scheme of one-dimensional ZND detonation model

The typical particle velocity histories recorded by embedded gauges during detonation of heterogeneous high explosive are shown in Figure 7.4. It can be seen from Figure 7.4 that shock wave is continuously strengthened while propagating in explosive bar till a stable detonation wave is formed. The distance before a shock wave transits to stable detonation wave is so-called run-to-detonation distance.

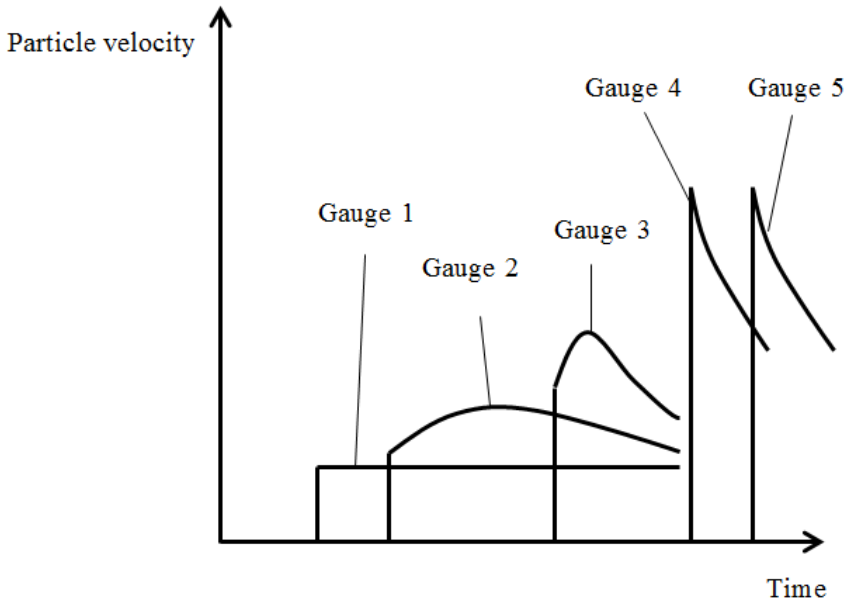

Figure 7.4 Typical particle velocity histories recorded by embedded gauges

Based on ZND detonation model, several numerical models have been proposed to describe the detonation of high explosive. The most popular model is ignition and growth model, which is incorporated in our SPH code.

Compared with the standard JWL model which includes only a single EoS for explosive gases, ignition and growth model uses JWL EoSs for both solid explosive and gaseous products of explosives [24]:

$$\begin{cases} p_s = A_s e^{-R_{1s}V_s} + B_s e^{-R_{2s}V_s} + \frac{\omega_s C_{Vs} T_s}{V_s} \\ p_g = A_g e^{-R_{1g}V_g} + B_g e^{-R_{2g}V_g} + \frac{\omega_g C_{Vg} T_g}{V_g} \end{cases} \quad \text{Eqn. 7.1}$$

where p is pressure, V is relative volume ($V = V/V_0 = \rho_0/\rho$), T is temperature, C_V is average heat capacity, and A, B, R_1, R_2 , ω are parameters fitted based on experiment. s represents solid explosive and g represents gaseous products of explosive.

The speed of sound is given by the approximation

$$c = \sqrt{\frac{\mathrm{d}p}{\mathrm{d}\rho}} \quad \text{Eqn. 7.2}$$

where p is pressure of solid explosive or gaseous products of explosive, ρ is density.

Two physical assumptions are introduced in the ignition and growth model, which are temperature equilibrium and pressure equilibrium, as shown as follow [24]:

$$\begin{cases} p_s = p_g \\ T_s = T_g \end{cases} \quad \text{Eqn. 7.3}$$

Temperature equilibrium is often used as a standard approach for closure of the problem. Temperature is calculated using the following formula:

$$T_s = T_g = \frac{e}{C_V} = \frac{e}{(1-\lambda)C_{Vs}+\lambda C_{Vs}} \quad \text{Eqn. 7.3a}$$

where e is the specific internal energy of the particle, C_V is the specific heat of the particle, λ is reaction progress.

The scheme of the two physical assumptions is shown in Figure 7.5.

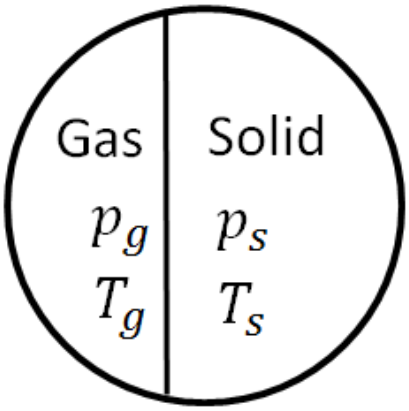

Figure 7.5 Scheme of pressure equilibrium and temperature equilibrium for an explosive particle

It is assumed that each explosive particle consists of two phases, one solid phase and the other gas phase. Since the mass of an explosive particle is fixed, the mass fraction of solid phase and gas phase should be carefully chosen so that the pressure of solid phase and gas phase will be equal. The temperature of explosive particle is determined by the specific internal energy and the average specific heat.

The reaction rate equation in ignition and growth model has the following form:

$$\frac{\mathrm{d}\lambda}{\mathrm{d}t} = \lambda_1 + \lambda_2 + \lambda_3 \quad \text{Eqn. 7.4}$$

$$\begin{cases} \lambda_1 = I(1-\lambda)^b \left(\frac{\rho}{\rho_0} - 1 - a\right)^x, 0 < \lambda \le \lambda_{ig\max} \\ \lambda_2 = G_1(1-\lambda)^c \lambda^d p^y, 0 < \lambda \le \lambda_{G1\max} \\ \lambda_3 = G_2(1-\lambda)^e \lambda^g p^z, \lambda_{G2\min} \le \lambda < 1 \end{cases} \quad \text{Eqn. 7.4a}$$

where I, a, b, x, c, d, y, e, g, z, G_1, G_2, λ_{igmax} , λ_{G1max}, λ_{G2min} are rate constant fitted based on experiment, ρ is the real-time density of explosive particle during simulation. λ_1 is ignition item, λ_2, λ_3 are growth items. Different hot spot models lead to different values for constant x. Constants c, d, e, g are related to the choice of the geometry for the hot spot combustion process. Hot spot can be considered to burn outwards from to void center, or inward over the total grain surface. The remaining constants I, G_1, G_2, z are found by fitting simulated pressure-time records to experimentally measured embedded gauge records.

In the implementation of ignition and growth model, the state of explosive can be described by reaction progress λ, which is a number between 0 and 1. 0 represents inert explosive, and 1 represents fully reacted explosive products. The number between 0 and 1 represents explosion products in mixing state.

7.2 Molecular dynamics with reactive force field

Molecular dynamics method is a powerful tool to investigate the physical movements of atoms and molecules. The trajectories of atoms and molecules are determined by Newton's equations of motion.

The idea of molecular dynamics is derived from quantum chemistry (QC), which is used to predict geometries, energies and vibrational energies for small molecules. However, QC is not practical for studying the dynamic properties of larger molecules and solids. It would be useful to have accurate force fields to quickly evaluate the forces and other dynamical properties such as the effects of mechanical shock waves or diffusion of small molecules in polymer and mesoporous zeolites [18]. Indeed, a number of FFs, such as MM3 [133-135], provide accurate predictions of geometries, conformational energy differences and heat of formation. Generic FF such as DREIDING [136] and UFF [137] allow predictions for broad classes of compounds, particularly when coupled to charge equilibration (QEq) [138] or other methods for predicting charges. However, those force fields are not capable to describe chemical reactivity. Brenner force field is an exception because it is formulated to describe bond breaking. However, it does not include van der Waals and Coulomb interactions which are critical in predicting structures and properties of many systems. In addition, the Brenner force field does not repair fundamental problems in the shapes of dissociation and reactive potential curves. A method that has the full chemistry of the breaking and forming bonds and a proper description of the fully bonded equilibrium geometry of complex molecules is in great need.

Thus, a general bond-order-dependent potential named ReaxFF is developed in which van der Waals and Coulomb forces are included and the dissociation and reaction curves are derived from QC calculations [18]. With ReaxFF, quantum phenomena such as resonance, unsaturated valences in radical systems and chemical reactivity can be accurately described.

Similar to empirical nonreactive force field, the reactive force field divides the system energy into various energy contributions (atom under/overcoordination, valence angle terms, torsion angles, conjugated systems, nonbonded van der Waals interactions, Coulomb interactions), as follow [18]:

$$E_{\text{system}} = E_{\text{bond}} + E_{\text{over}} + E_{\text{under}} + E_{\text{val}} + E_{\text{pen}} + E_{\text{tors}} + E_{\text{conj}} + E_{\text{vdWaals}} + E_{\text{Coulomb}} \quad \text{Eqn. 7.5}$$

where E_{bond} is the bond energy, E_{over} and E_{under} is the energy penalty caused by over-/undercoordinated atom, E_{val} is the energy contribution from valence angle terms, E_{pen} is the additional energy penalty for system with two double bonds sharing an atom in a valency angle, E_{tors} is the energy of torsion angle,

E_{conj} is the energy contributed by conjugation effects, E_{vdWaals} is the energy resulting from van der Waals interactions, E_{Coulomb} is the energy resulting from Coulomb interactions.

Since the introduction of ReaxFF, it has been successfully applied in a variety of reactive dynamics simulations of hydrocarbon organic compounds [139], polymers [21], energetic materials [140-144], shock process [142, 143, 145] and combustion [139, 146]. However, when dealing with solids, ReaxFF does not account adequately for long-range London dispersion (van der Waals attraction) which is significantly important in molecular solids, resulting in equilibrium volumes about $10\sim15\%$ higher than its normal density, which is unacceptable. Therefore, an additional vdW-like interaction is introduced in the original ReaxFF to account for long-range London dispersion [19]. The corrected reactive force field is named ReaxFF-lg.

In ReaxFF-lg, the total energy of the system can be expressed as [19]:

$$E_{\mathrm{Reax-lg}} = E_{\mathrm{Reax}} + E_{\mathrm{lg}} \qquad \text{Eqn. 7.6}$$

where E_{Reax} is the energy evaluated from previous ReaxFF, E_{lg} is the long-range-correction terms.

In the work, an updated ReaxFF-lg (ReaxFF-d3) trained by QC is used to calculate the EoSs of solid explosive and gaseous products of $\beta-$ HMX.

7.3 Smoothed particle hydrodynamics method

7.3.1 Function approximation in SPH

SPH was formulated to solve hydrodynamics problems that are governed in form of partial differential equations (PDEs) with primary field variables of density, velocity, and energy [36]. It was also extended to solve problems such as solid mechanics. In SPH method, the entire domain is discretized by a finite number of particles that carry individual mass and occupy individual space. Any field function $f(\boldsymbol{x})$ in the problem domain can be approximated in SPH as follow [38]:

$$\langle f(\boldsymbol{x})\rangle = \int_{\Omega} f(\boldsymbol{x}')W(\boldsymbol{x}-\boldsymbol{x}',h)d\boldsymbol{x}' \qquad \text{Eqn. 7.7}$$

where Ω is problem domain, f is a field function related to the three-dimensional position vector $\boldsymbol{x}$, $W(\boldsymbol{x}-\boldsymbol{x}',h)$ is smoothing kernel function, h is smoothing length which defines influence area of the smoothing function W. Various smoothing kernel functions have been proposed with the development of SPH method, such as cubic spline kernel [147], Gaussian kernel [148], quartic and quantic splines [149].

Smoothing function W should be chosen to satisfy a number of conditions. The first is called the normalization condition:

$$\int_{\Omega} W(\boldsymbol{x}-\boldsymbol{x}',h)d\boldsymbol{x}' = 1 \qquad \text{Eqn. 7.8}$$

The second is called the Delta function property:

$$\lim_{h\to 0} W(\boldsymbol{x}-\boldsymbol{x}',h) = \delta(\boldsymbol{x}-\boldsymbol{x}') \qquad \text{Eqn. 7.9}$$

The last is called the compact condition:

$$W(\boldsymbol{x}-\boldsymbol{x}',h)=0 \text{ when } |\boldsymbol{x}-\boldsymbol{x}'|>\kappa h \quad \text{Eqn. 7.10}$$

where κ is a scalar factor associated with smoothing function κh which defines the effective area of the smoothing area. The effective area is called support domain for the point at $\boldsymbol{x}$.

Gaussian kernel is chosen for the SPH simulation in the work, which is written as:

$$W(R,h)=\alpha_d e^{-R^2} \quad \text{Eqn. 7.11}$$

where

$$R=\frac{|\boldsymbol{x}-\boldsymbol{x}'|}{h} \quad \text{Eqn. 7.11a}$$

$$\alpha_d=\begin{cases}\frac{1}{\pi^{1/2}h}, & one-dimenional\\ \frac{1}{\pi h^2}, & two-dimensional\\ \frac{1}{\pi^{3/2}h^3}, & three-dimensional\end{cases} \quad \text{Eqn. 7.11b}$$

Based on product rule for derivatives and Gauss's Law, the derivative of function $f(\boldsymbol{x})$ can be derived as follow:

$$\langle\nabla\cdot f(\boldsymbol{x})\rangle=\int_S f(\boldsymbol{x}')W(\boldsymbol{x}-\boldsymbol{x}',h)\cdot\vec{\boldsymbol{n}}dS-\int_\Omega f(\boldsymbol{x}')\cdot\nabla W(\boldsymbol{x}-\boldsymbol{x}',h)d\boldsymbol{x}' \quad \text{Eqn. 7.12}$$

where $\vec{\boldsymbol{n}}$ is the unit vector normal to the surface S. If the support zone is within problem domain, according to compact condition of smoothing kernel function, we have:

$$W(\boldsymbol{x}-\boldsymbol{x}',h)|_S=0 \quad \text{Eqn. 7.13}$$

Therefore,

$$f(\boldsymbol{x}')W(\boldsymbol{x}-\boldsymbol{x}',h)=0 \quad \text{Eqn. 7.14}$$

Thus, Eqn. 7.12 can be rewritten as:

$$\langle\nabla\cdot f(\boldsymbol{x})\rangle=-\int_\Omega f(\boldsymbol{x}')\cdot\nabla W(\boldsymbol{x}-\boldsymbol{x}',h)d\boldsymbol{x}' \quad \text{Eqn. 7.15}$$

To calculate the integration of Eqn. 7.7 and Eqn. 7.15, a summation over all particles within the support domain is implemented, as shown in Figure 7.6.

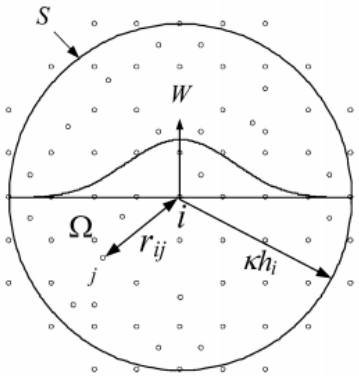

Figure 7.6 Support zone of particle i

Therefore, Eqn. 7.7 and Eqn 7.15 can be rewritten as:

$$\langle f(\boldsymbol{x}_i)\rangle = \sum_{j=1}^{N} \frac{m_j}{\rho_j} f(\boldsymbol{x}_j) W_{ij} \qquad \text{Eqn. 7.16}$$

$$\langle \nabla \cdot f(\boldsymbol{x}_i)\rangle = -\sum_{j=1}^{N} \frac{m_j}{\rho_j} f(\boldsymbol{x}_j) \cdot \nabla W_{ij} \qquad \text{Eqn. 7.17}$$

where m is the mass of particle, ρ is the density of particle, and W_{ij} can be written as

$$W_{ij} = W(\boldsymbol{x_i} - \boldsymbol{x}_j, h) \qquad \text{Eqn. 7.17a}$$

7.3.2 Discretization of governing equations

The governing equations for hydrodynamics problems are Navier-Stokes equations. The standard Lagrangian form of the Navier-Stokes equations consists of, first, the continuity equation [38]:

$$\frac{\mathrm{d}\rho}{\mathrm{d}t} = -\rho \frac{\partial \boldsymbol{v}^{\beta}}{\partial \boldsymbol{x}^{\beta}} \qquad \text{Eqn. 7.18}$$

Second, the momentum equation:

$$\frac{\mathrm{d}\boldsymbol{v}^{\alpha}}{\mathrm{d}t} = \frac{1}{\rho} \frac{\partial \sigma^{\alpha\beta}}{\partial \boldsymbol{x}^{\beta}} \qquad \text{Eqn. 7.19}$$

Third, the energy equation:

$$\frac{\mathrm{d}e}{\mathrm{d}t} = \frac{\sigma^{\alpha\beta}}{\rho} \frac{\partial \boldsymbol{v}^{\alpha}}{\partial \boldsymbol{x}^{\beta}} \qquad \text{Eqn. 7.20}$$

where ρ is density, e is specific internal energy, $\boldsymbol{v}^{\alpha}$ is velocity, and $\sigma^{\alpha\beta}$ is the total stress tensor, which are all dependent variables. $\boldsymbol{x}^{\alpha}$ is spatial coordinate and t is time , which are independent variables. The total stress tensor $\sigma^{\alpha\beta}$ consists of two parts, one is isotropic pressure p and the other is shear stress $\tau^{\alpha\beta}$:

$$\sigma^{\alpha\beta} = -p\delta^{\alpha\beta} + \tau^{\alpha\beta} \qquad \text{Eqn. 7.21}$$

where $\delta^{\alpha\beta}$ is Kronecker delta, which can be written as

$$\delta^{\alpha\beta} = \begin{cases} 0 & if\ \alpha \neq \beta \\ 1 & if\ \alpha = \beta \end{cases} \qquad \text{Eqn. 7.21a}$$

For explosive gas, the viscous shear stress can be neglected compared with the isotropic pressure. For solid materials, shear stress can be obtained from constitutive equations of material. In implementation of SPH method, to approximate density of particle, an approach called continuity density is adopted. After manipulation, Eqn. 7.18 can be rewritten as:

$$\frac{\mathrm{d}\rho}{\mathrm{d}t} = \rho_i \sum_{j=1}^{N} \frac{m_j}{\rho_j} \boldsymbol{v}_{ij}^{\beta} \frac{\partial W_{ij}}{\partial \boldsymbol{x}_i^{\beta}} \qquad \text{Eqn. 7.22}$$

Similarly, Eqn. 7.19 and Eqn. 7.20 can be respectively rewritten as follow:

$$\frac{\mathrm{d}\boldsymbol{v}_i^{\alpha}}{\mathrm{d}t} = \sum_{j=1}^{N} m_j \left(\frac{p_i}{\rho_i^2} + \frac{p_i}{\rho_j^2} + \Pi_{ij} \right) \frac{\partial W_{ij}}{\partial \boldsymbol{x}_i^{\beta}} \qquad \text{Eqn. 7.23}$$

$$\frac{\mathrm{d}e_i}{\mathrm{d}t} = \frac{1}{2} \sum_{j=1}^{N} m_j \left(\frac{p_i}{\rho_i^2} + \frac{p_j}{\rho_j^2} + \Pi_{ij} \right) \boldsymbol{v}_{ij}^{\beta} \frac{\partial W_{ij}}{\partial \boldsymbol{x}_i^{\beta}} \qquad \text{Eqn. 7.24}$$

where Π_{ij} is artificial viscosity, p_i is hydrostatic pressure of particle i, which will be obtained from EoS.

Considering the release of chemical heat in detonation, a source item is added to the energy equation. Thus, the modified energy equations used in SPH can be expressed as follow:

$$\frac{\mathrm{d}e_i}{\mathrm{dt}} = \frac{1}{2}\sum_{j=1}^{N} m_j \left(\frac{p_i}{\rho_i^2} + \frac{p_j}{\rho_j^2} + \Pi_{ij}\right) \boldsymbol{v}_{ij}^{\beta} \frac{\partial W_{ij}}{\partial \boldsymbol{x}_i^{\beta}} + \dot{q} \qquad \text{Eqn. 7.25}$$

where $\dot{q}$ is heat release rate, which plays critical role in transition of shock wave to detonation wave. Leap-frog algorithm is applied to integrate the governing equations over time.

7.3.3 Artificial viscosity

In order to suppress unphysical fluctuation in the simulation of discontinuity such as shock waves, artificial viscosity is introduced in the beginning development of SPH. Actually, shock wave is not real physical discontinuity but a very narrow zone where the status of medium experiences sudden change. To conserve mass, momentum and energy across the shock wave front, the simulation of transformation of kinetic energy to heat is required. Physically the transformation is done in the form of energy dissipation, which inspires researchers to introduce artificial viscosity in SPH [150-153]. Monaghan type artificial viscosity Π_{ij} is implemented in the following SPH simulation, which can be written as:

$$\Pi_{ij} = \begin{cases} \dfrac{-\alpha \bar{c}_{ij}\phi_{ij} + \beta\phi_{ij}^2}{\bar{\rho}_{ij}}, & \boldsymbol{v}_{ij}\cdot\boldsymbol{x}_{ij} < 0 \\ 0, & \boldsymbol{v}_{ij}\cdot\boldsymbol{x}_{ij} > 0 \end{cases} \qquad \text{Eqn. 7.26}$$

where

$$\phi_{ij} = \frac{h_{ij}\boldsymbol{v}_{ij}\boldsymbol{x}_{ij}}{|\boldsymbol{x}_{ij}|^2 + \varphi^2} \qquad \text{Eqn. 7.26a}$$

$$\bar{c}_{ij} = \frac{1}{2}(c_i + c_j) \qquad \text{Eqn. 7.26b}$$

$$\bar{\rho}_{ij} = \frac{1}{2}(\rho_i + \rho_j) \qquad \text{Eqn. 7.26c}$$

$$h_{ij} = \frac{1}{2}(h_i + h_j) \qquad \text{Eqn. 7.26d}$$

$$\boldsymbol{v}_{ij} = \boldsymbol{v}_i - \boldsymbol{v}_j \qquad \text{Eqn. 7.26e}$$

$$\boldsymbol{x}_{ij} = \boldsymbol{x}_i - \boldsymbol{x}_j \qquad \text{Eqn. 7.26f}$$

where α and β are constants, φ is used to prevent numerical divergences between two particles, c and v represent the speed of sound and velocity of particle, respectively. The viscosity term associated with α produces a bulk viscosity, while the second term associated with β is intended to suppress particle interpenetration at high Mach number. Generally, α, β, φ are set to be 1, 1 and 0.1 respectively.

7.3.4 Smoothing length update

Smoothing length h plays significant role in SPH simulation, which has direct influence on computation efficiency and accuracy of the solution. If h is too small, there may be insufficient particles in the support domain to exert force on a given particle. Instead, if h is too large, all details of the particle

or local properties may be smoothed out, and computation efficiency is reduced, too. The particle approximation in SPH depends on sufficient number of particles within the support of domain of a particle.

In the early development of SPH, the global particle smoothing length was used which depended on the initial average density of the system. Later, variable smoothing length is adopted to maintain consistent accuracy throughout the space [148-153].

The following method is used to update the smoothing length of each particle during the implementation [38]:

$$\frac{\mathrm{d}h_i^n}{\mathrm{d}t} = -\frac{h_i^n}{\rho_i^n d}\frac{\mathrm{d}\rho_i^n}{\mathrm{d}t} \qquad \text{Eqn. 7.27}$$

where h_i^n, $\rho_i^n$are smoothing length, density of particle i at time step n. For convenience, Eqn. 7.27 can be further written in the following form:

$$\frac{\mathrm{d}h_i^n}{\mathrm{d}t} = -\frac{h_i^n}{\rho_i^n d}\sum_{j=1}^{N} m_j \boldsymbol{v}_{ij}^n \cdot \nabla_i^n W_{ij} \qquad \text{Eqn. 7.28}$$

where $\boldsymbol{v}_i^n$ and $\nabla_i^n \mathrm{W}_{ij}$ are velocity and kernel gradient of particle i at time step n.

Thus, the smoothing length at the next step becomes

$$h_i^{n+1} = h_i^n + \frac{\mathrm{d}h_i^n}{\mathrm{d}t}\Delta t \qquad \text{Eqn. 7.29}$$

7.3.5 Constitutive model of copper

Johnson-Cook (JC) model is a popular empirical constitutive model which was proposed by Johnson and Cook in 1985 [154] to account for factors that are significant when materials are loaded into plastic range in shock or impact. The factors include large strain, large strain rates, high pressure and high temperature.

For materials with incompressible plasticity (such as copper), the von Mises stress is given by:

$$\sigma_y = \sqrt{3J_2} \qquad \text{Eqn. 7.30}$$

where J_2 stands for second deviatoric stress invariant that can be written as:

$$J_2 = \frac{1}{6}[(\sigma_1 - \sigma_2)^2 + (\sigma_2 - \sigma_3)^2 + (\sigma_3 - \sigma_1)^2] \qquad \text{Eqn. 7.30a}$$

where σ_1, σ_2, σ_3 are principal stresses.

According to Johnson-Cook model, the flow stress (yield stress) can be expressed as a function of plastic strain, strain rate and temperature as follow:

$$\sigma_y = \left(A + B\left(\varepsilon_p\right)^n\right)\left(1 + C\ln \dot{\varepsilon}_p{}^*\right)(1 - (T^*)^m) \qquad \text{Eqn. 7.31}$$

where A, B, C, m are material constants, ε_p is equivalent plastic strain, $\dot{\varepsilon}_p{}^*$ is the normalized equivalent plastic strain rate that can be expresses as:

$$\dot{\varepsilon}_p{}^* = \frac{\dot{\varepsilon}_p}{\dot{\varepsilon}_{p0}} \quad \text{Eqn. 7.31a}$$

where $\dot{\varepsilon}_p$ is equivalent plastic strain rate, $\dot{\varepsilon}_{p0}$ is equivalent plastic strain rate of the quasi-static test. T^* is expressed as:

$$T^* = \frac{T-T_0}{T_m-T_0} \quad \text{Eqn. 7.31b}$$

where T_0 is reference temperature and T_m is reference melt temperature.

7.3.6 Mie-Gruneisen EoS of copper

Traditionally, an EoS is equation which describes the pressure of a material as a function of density and temperature. It is needed to solve the continuity, momentum and energy equations that govern the thermodynamics transition of a material [155]. For high-velocity impact problems, thermodynamics states often change so rapidly that there is little time for heat transfer. Thus it is reasonable to consider high-velocity impact an adiabatic process. Mie-Gruneisen EoS is often used in hydrocodes to simulate shock-compressed solids, which can be expressed as [156]:

$$p = \begin{cases} \frac{\rho_0 {c_0}^2 \varphi}{(1-s\varphi)^2}\left[1-\frac{\mathcal{G}}{2\upsilon}(\upsilon_0-\upsilon)\right]+\mathcal{G}\frac{e}{\upsilon}, & if\ \upsilon \le \upsilon_0 \\ {c_0}^2\left(\frac{1}{\upsilon}-\frac{1}{\upsilon_0}\right)+\mathcal{G}\frac{e}{\upsilon}, & if\ \upsilon > \upsilon_0 \end{cases} \quad \text{Eqn. 7.32}$$

where $\mathcal{G}$ is Gruneisen parameter, c_0 is reference sound velocity, ρ_0 is reference density, υ is specific volume, s is constant, φ is expressed as:

$$\varphi = 1-\frac{\upsilon}{\upsilon_0} \quad \text{Eqn. 7.32a}$$

where

$$\upsilon = \frac{1}{\rho} \quad \text{Eqn. 7.32b}$$

7.4 Benchmark test of the SPH method with artificial viscosity

A one-dimensional shock tube problem is used as benchmark to validate the SPH algorithm. The initial conditions of the shock tube problem is described as [157]

$$\begin{cases} \rho = 1, \upsilon = 0, e = 2.5, p = 1 & when\ x \le 0 \\ \rho = 0.25, \upsilon = 0, e = 1.795, p = 0.1795 & when\ x > 0 \end{cases} \quad \text{Eqn. 7.33}$$

800 particles are used in the simulation. All particles have the same mass of $m_i = 0.001875$. 640 particles are distributed in the high-density area ranging from -0.6 to 0, while 160 particles are distributed in the low-density area ranging from 0 to 0.6. Time step is $0.005s$ and total steps are 40. Artificial viscosity is applied when using the traditional SPH. The comparison of theoretical solution with results obtained by traditional SPH is shown in Figure 7.7.

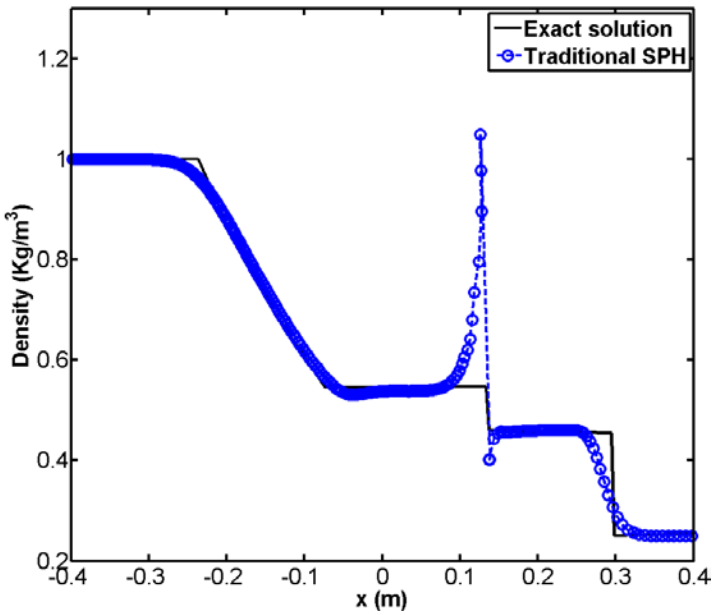

(a) Comparison of density calculated by traditional SPH with exact solution

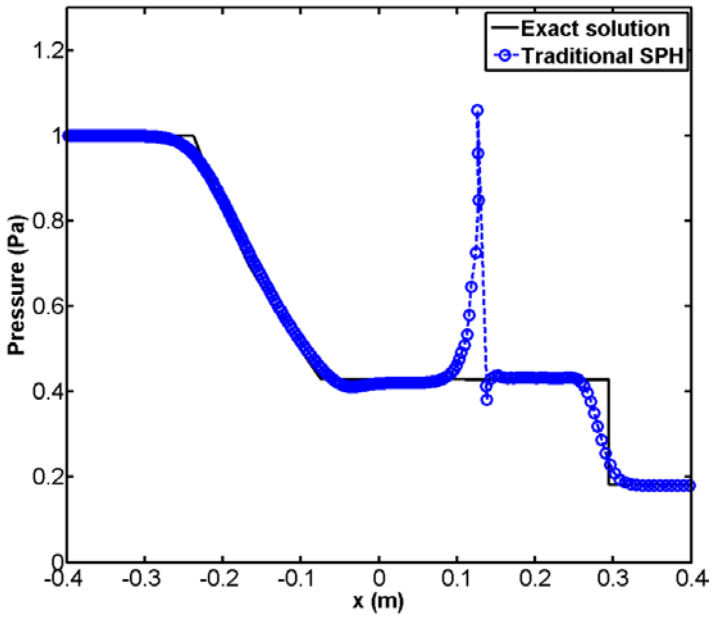

(b) Comparison of pressure calculated by traditional SPH with exact solution

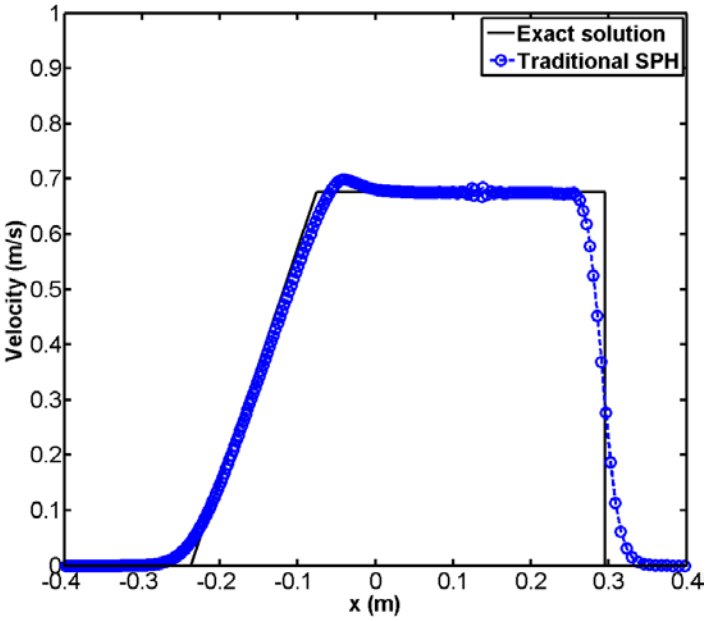

(c) Comparison of velocity calculated by traditional SPH with exact solution

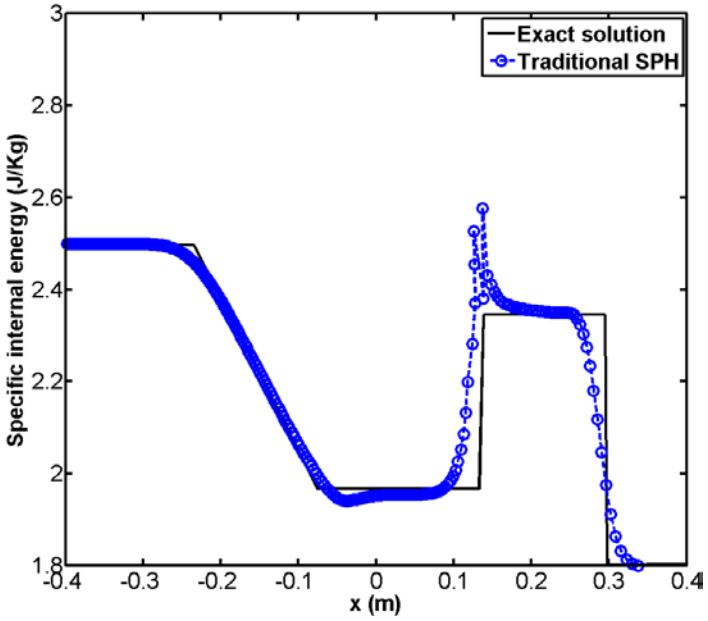

(d) Comparison of specific internal energy calculated by traditional SPH with exact solution

Figure 7.7 One-dimensional shock tube problem. Comparison of characteristics calculated by traditional SPH with exact solution

It can be seen from Figure 7.7(a), (b) that there is obvious fluctuation at the shock front when using traditional SPH, which indicates that artificial viscosity cannot thoroughly eliminate fluctuation.

7.5 Detonation of a 1D PBX 9501 bar

The following experiment [24] is studied using proposed SPH method: A 100 *mm* diameter, 12.5 *mm* thick aluminum flyer plate impacts a target consisting of: a 90 *mm* diameter, 6 *mm* thick aluminum plate, a 90 *mm* diameter, 20 *mm* thick PBX 9501 charge, and a 90 *mm* diameter, 6 *mm* thick aluminum back plate. Scheme of the experimental configuration is shown in Figure 7.8. Pressure gauges are embedded in the explosive to record the variation of pressure during detonation.

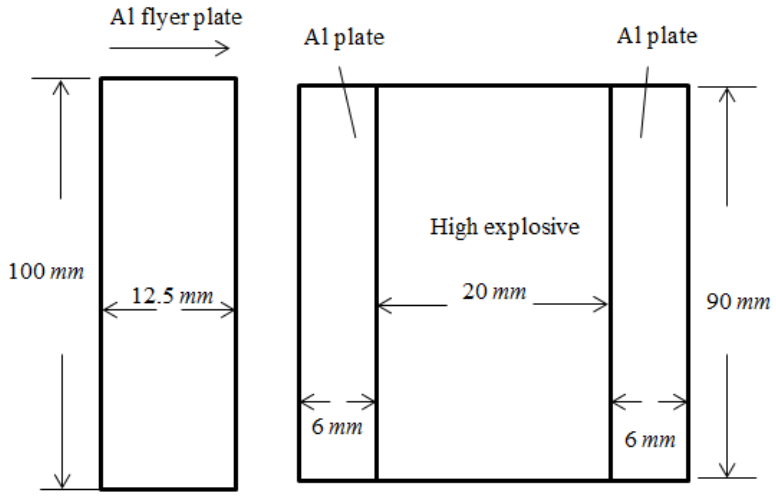

Figure 7.8 Scheme of the configuration of flyer plate impact experiment

7.5.1 Case 1

The experiment mentioned above is simplified to a one-dimensional PBX 9501 model as shown in Figure 7.9. The simplified one-dimensional PBX 9501 model is 0.02 *m* long. On the left there is a rigid wall, the explosive bar will impact against the rigid wall at certain velocity. In all the cases, particles are distributed uniformly and smoothing length of each particle is set to be 1.5 times the distance between two neighboring particles. The model consists of 4000 particles.

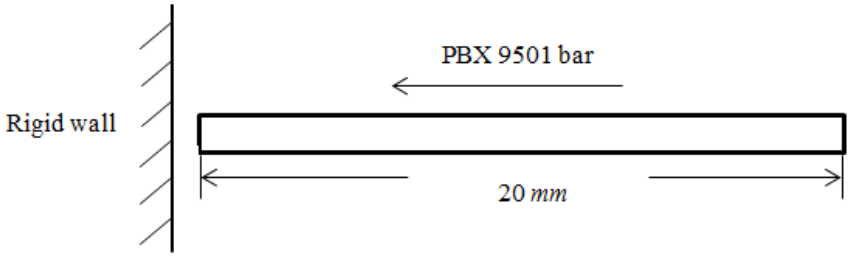

Figure 7.9 Scheme of simplified flyer plate impact experiment

The parameters of JWL EoS of solid PBX 9501 and gaseous products of PBX 9501, and JWL EoS of solid β-HMX and gaseous products of β-HMX are listed in Table 6.4 and Table 6.5. The parameters for reaction rate are as follow:

Table 7.1 Reaction rate parameters of PBX 9501 [24]

Reaction rate parameters of PBX 9501	
I	$1.4 \times 10^{17} s^{-1}$
a	0.0
b	0.667
x	20.0
c	0.667
d	0.277
y	2.0
e	0.333
g	1.0
z	2.0
G_1	$130 \times 10^{-16} Pa^{-y} s^{-1}$
G_2	$400 \times 10^{-16} Pa^{-z} s^{-1}$
$\lambda_{ig\max}$	0.3
$\lambda_{G1\max}$	0.5
$\lambda_{G2\max}$	0.5

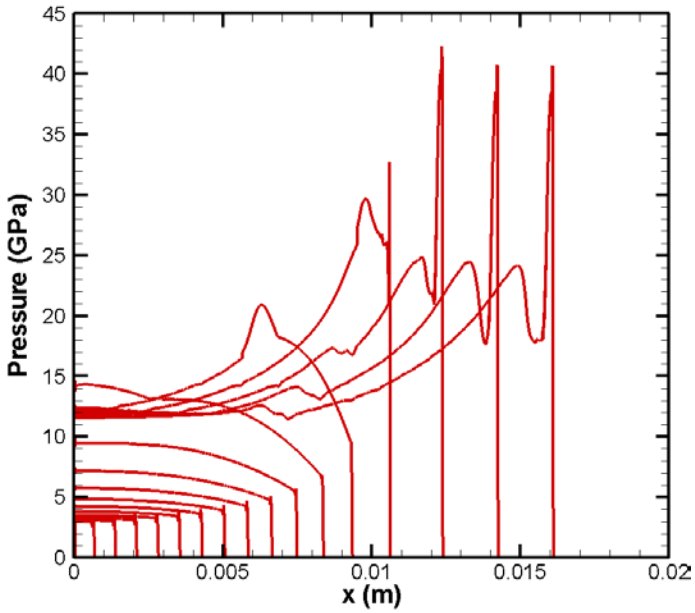

Figure 7.10 The variation of shock wave on the explosive bar with time.

The v_x is set to be 480 $/s$. The resulting impact pressure on detonation end is around 3.4 GPa. Ambient temperature is 25 ℃. The variation of shock wave on the explosive bar with time is shown in Figure 7.10, The time interval between two adjacent curves is 0.25 μs.

It can be clearly seen from Figure 7.10 that the shock wave increasingly builds up while propagating from left to right. When shock wave arrives at around 0.01 m, the explosive is detonated and the shock wave transforms into a self-sustained detonation wave. The detonation wave stabilizes at around 0.011 m. This build-up effect is contributed by the release of heat in detonation. According to experiment [24], the experimental run-to-detonation distance is 11 mm, which agrees very well with simulation.

The distribution of reaction, v_x and density along the one-dimensional PBX 9501 bar at 3.5 μs is shown in Figure 7.11.

The comparison of SPH simulation using original EoSs, fitted EoSs, FVM [24] and experiment [24] is shown in Figure 7.12, where the legend represents the distance of pressure gauge from detonation end.

It can be seen from Figure 7.12(b) that the calculated arrival time of shock wave is very close to experiment. The peak pressure calculated from fitted EoS is around 40 GPa, which also agrees well with experiment. However, all three simulations deviate from experiment somehow. It probably results from three reasons: first, detonation of high explosive is very complicated, though ignition and growth model can accurately predict arrival time and peak pressure of shock wave, it is not capable to present every detail of pressure history; second, the boundary conditions of the numerical model are simplified compared with experiment; third, the model is one-dimensional, which is different from the experiment in reality.

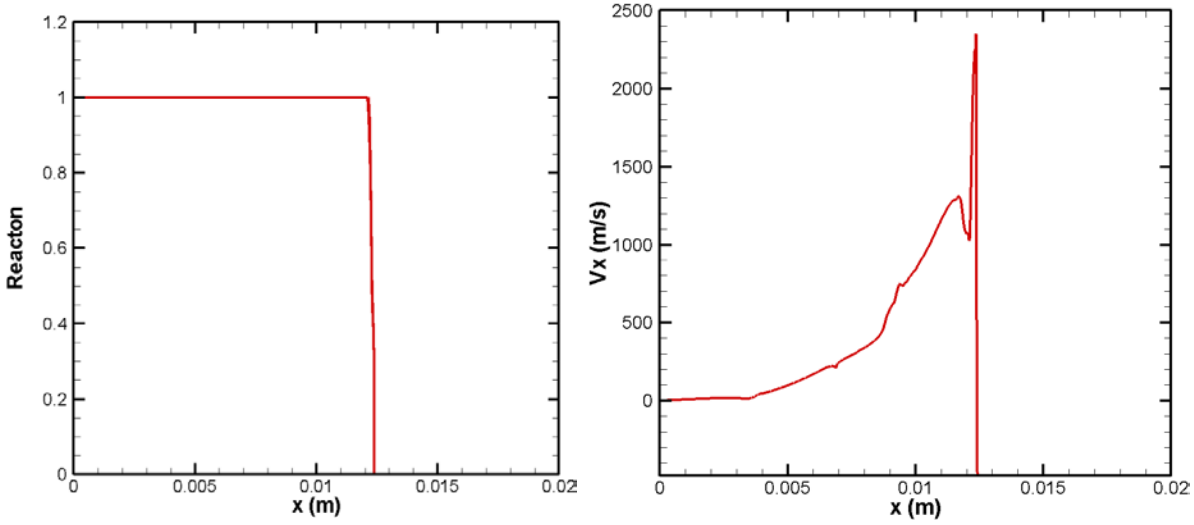

(a) Reaction (b) v_x

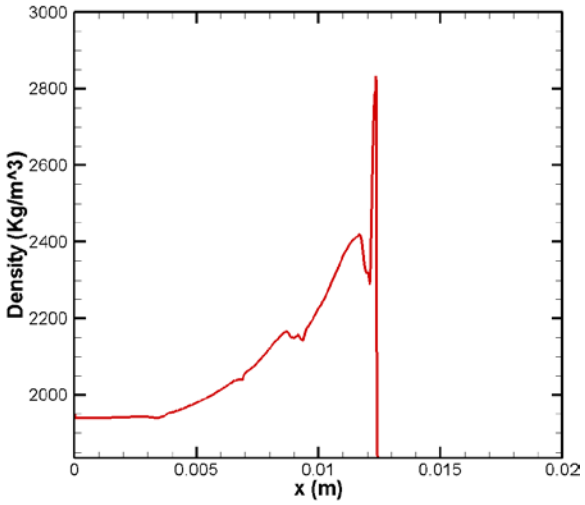

(c) Density

Figure 7.11 Reaction, v_x and density of the one-dimensional PBX 9501 bar at 3.5 μs

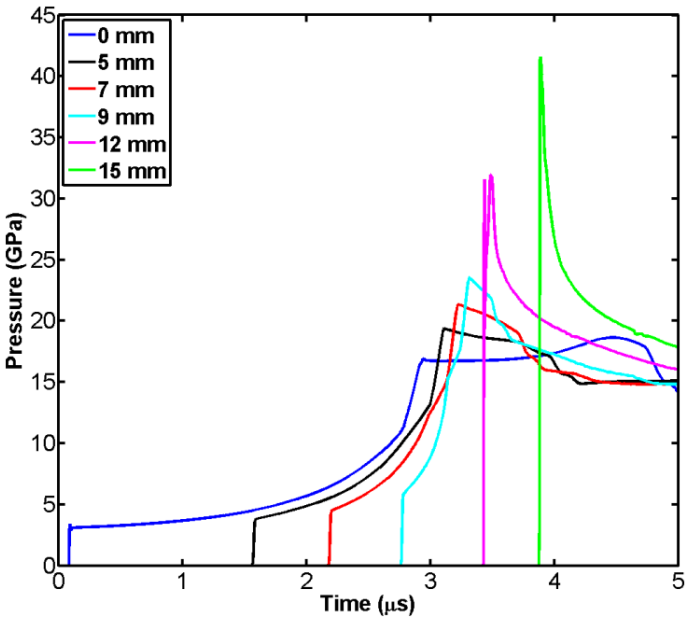

(a) SPH Simulation using original EoSs

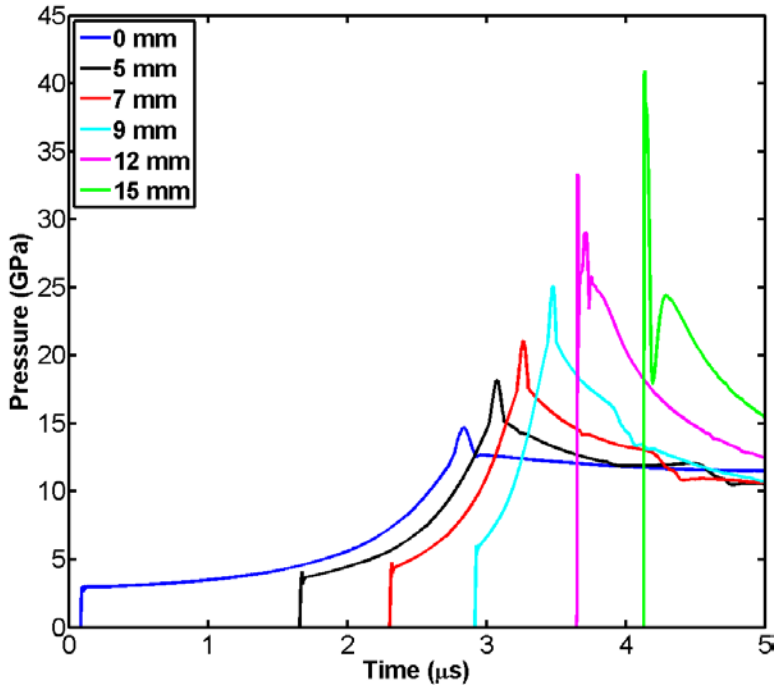

(b) SPH Simulation using fitted EoSs

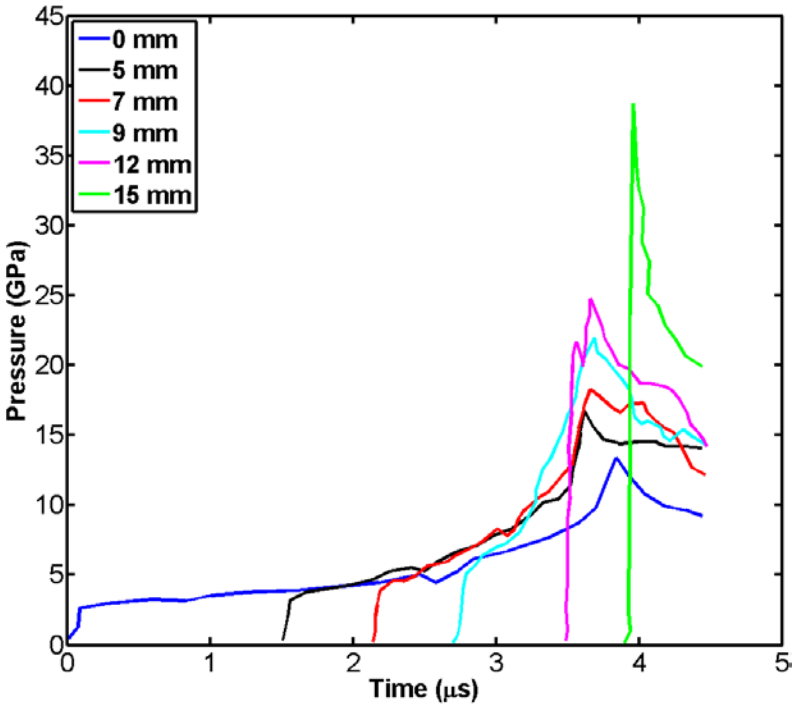

(c) FVM simulation using original EoSs

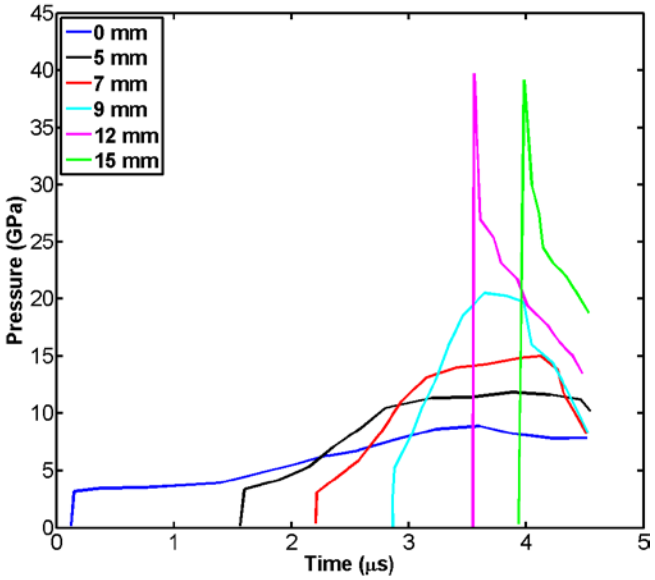

(d) Experiment

Figure 7.12 Comparison of SPH Simulation using original EoSs, fitted EoSs, FVM simulation and experiment.

7.5.2 Case 2

Configurations of the simulation are similar to case 1, except that the v_x is set to be 432 m/s. Ambient temperature is 50 ℃. Fitted EoSs obtained from MD simulations are used. The evolution of shock wave is shown in Figure 7.13.

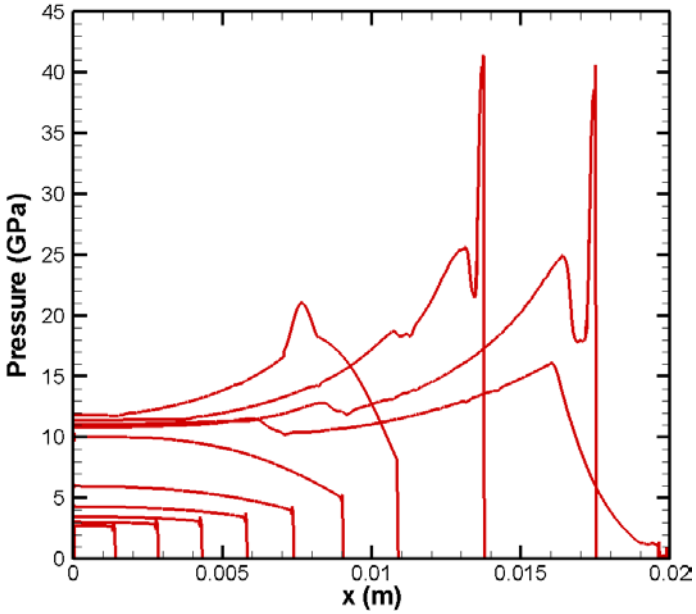

Figure 7.13 The variation of shock wave on the explosive bar with time. v_x is set to be 480 $/s$. Ambient temperature is 50 ℃.

It can be seen from Figure 7.13 that due to the decrease of impact velocity (thus impact pressure is reduced), the shock wave travels longer before transforming to detonation wave. According to experiment [24], the run-to-detonation distance is 13 mm, which agrees well with simulation. The comparison of SPH simulation using original EoSs, fitted EoSs, FVM [24] and experiment [24] is shown in Figure 7.14.

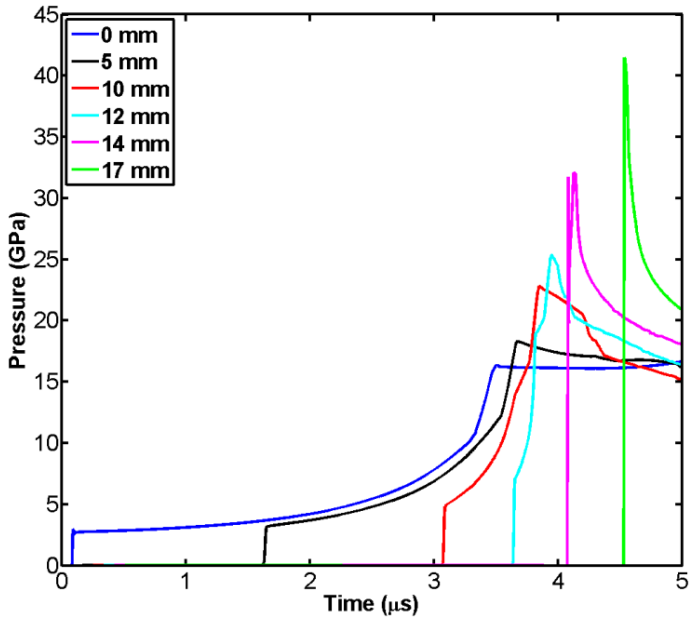

(a) SPH simulation using original EoSs

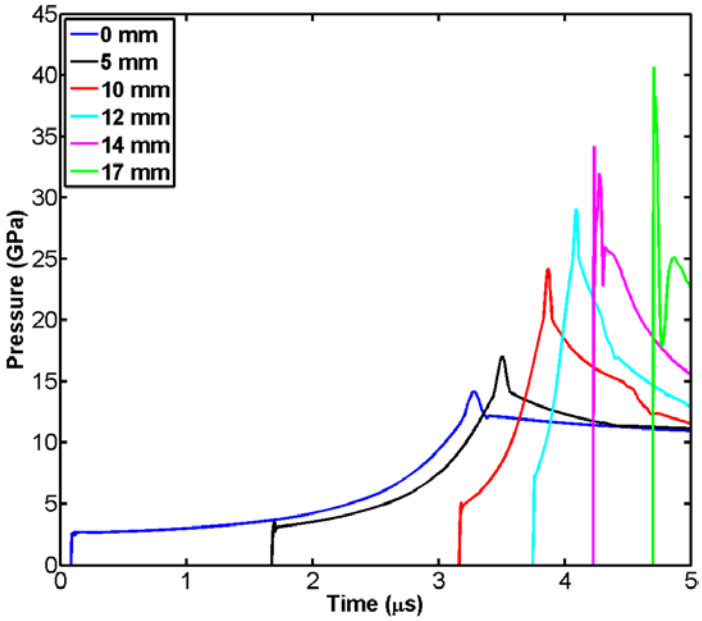

(b) SPH simulation using fitted EoSs

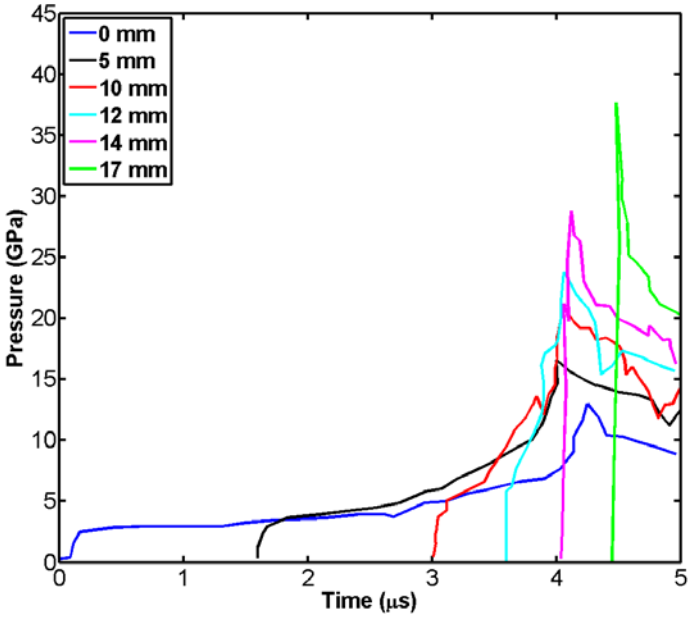

(c) Simulation using FVM

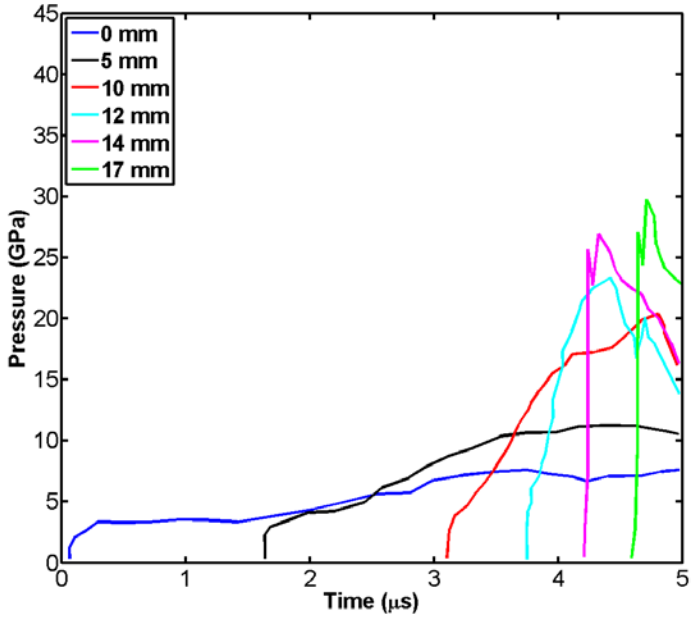

(d) Experiment

Figure 7.14 Comparison of SPH simulation using original EoSs, fitted EoSs, FVM and experiment

It can be seen from Figure 7.14 that the arrival time of shock wave calculated by SPH simulation using fitted EoSs agrees very well with experiment. However, all peak pressure (around 40 GPa) obtained in the three simulations, either SPH with original EoSs, fitted EoS or FVM, deviate from experiment (30 GPa) a lot. It indicates that though ignition and growth model is the most advanced model till today, it is still limited to depict all the details of detonation.

7.5.3 Case 3

Configurations of the simulation are similar to the other two, except that the v_x is set to be 540 m/s. Ambient temperature is 50 ℃. Fitted EoSs obtained from MD simulations are used. The evolution of shock wave is shown in Figure 7.15, where the time interval between two curves is 0.25 μs.

It can be seen from Figure 7.15 that as impact pressure increases, the shock wave travels shorter distance before transforming to detonation wave.

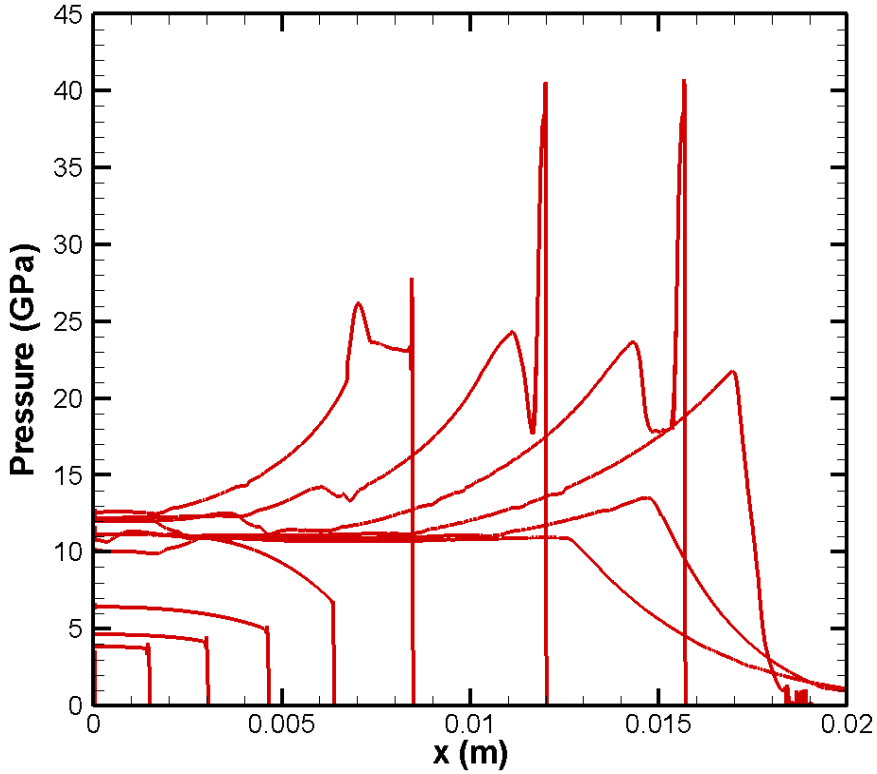

Figure 7.15 The variation of shock wave on the explosive bar with time. v_x is 540 m/s. Ambient temperature is 50 ℃.

The comparison of SPH simulation using original EoSs, fitted EoSs, FVM [24] and experiment [24] is shown in Figure 7.16.

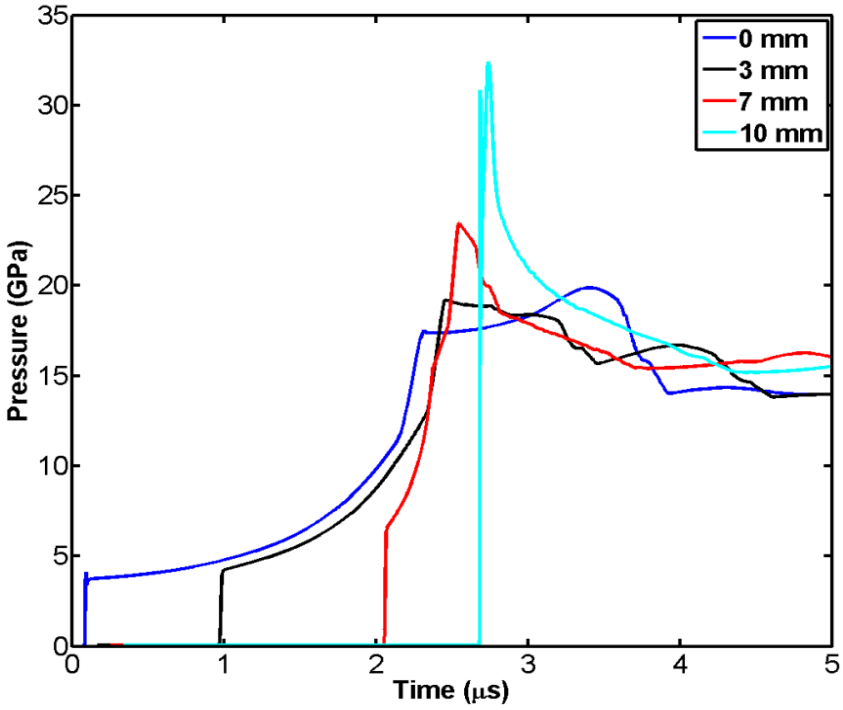

(a) SPH simulation using original EoSs

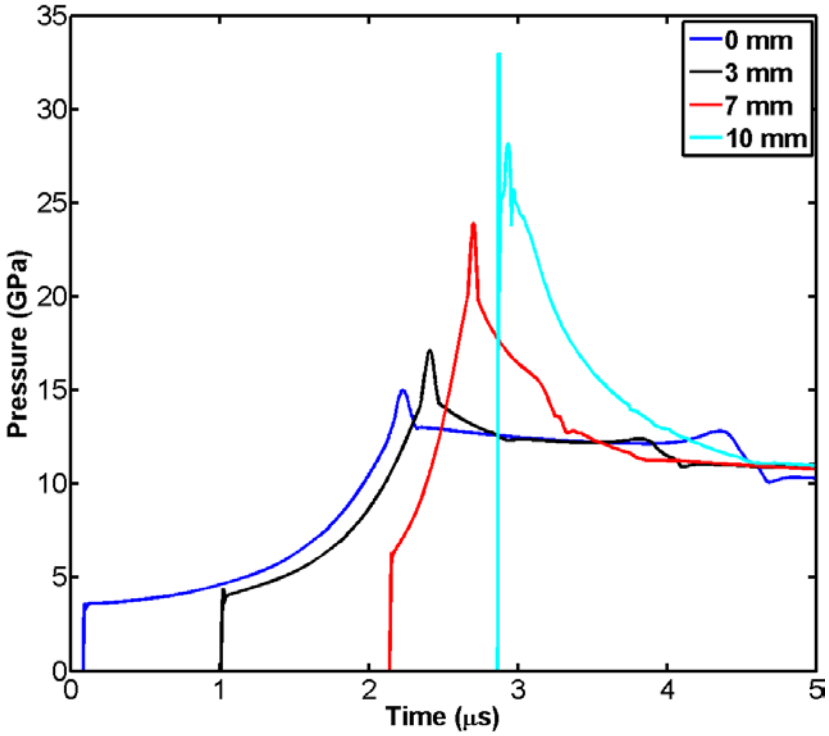

(b) SPH simulation using fitted EoSs

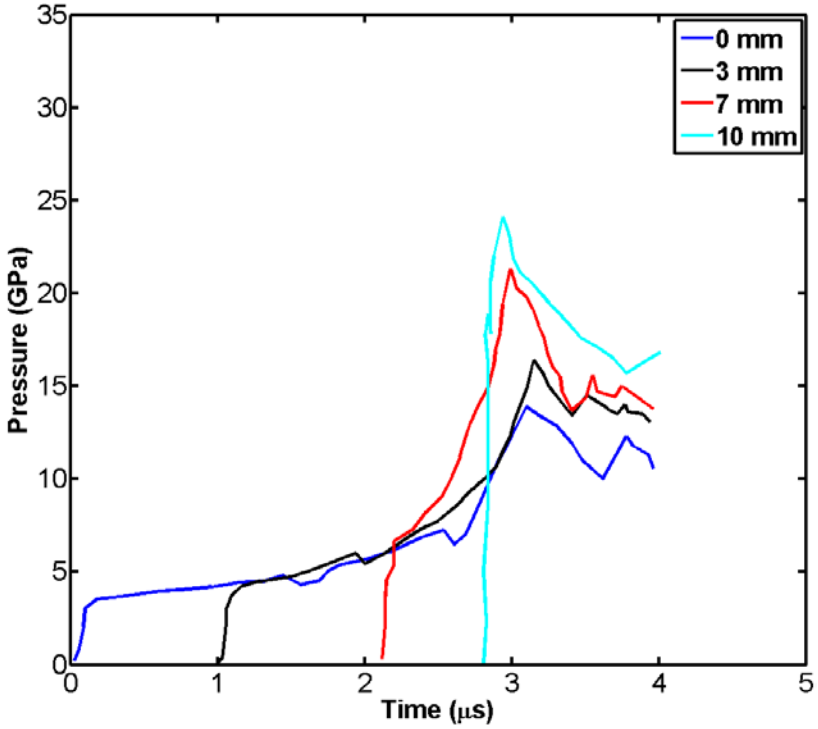

(c) Simulation using FVM

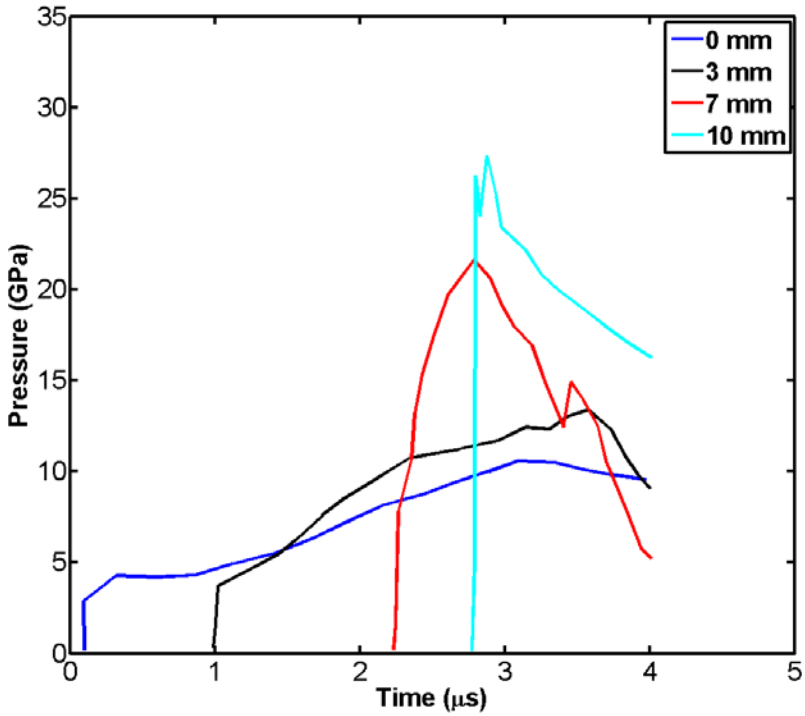

(d) Experiment

Figure 7.16 Comparison of SPH simulation using original EoSs, fitted EoSs, FVM and experiment

Similarly, the arrival time of shock wave calculated by SPH using fitted EoSs agrees well with experiment, except peak pressure and details of pressure history.

7.6 Influence of various factors on SPH

The artificial viscosity in SPH enables it to suppress oscillation in hydrodynamics problems. It is necessary to investigate the influence of artificial viscosity on simulation results. In addition, the influence of number of particles on simulation is also investigated. Original JWL EoSs are applied in all simulations in the section.

7.6.1 Influence of shear viscosity α on simulation

In this section, shear viscosity α is set to be 1.0, 2.0, 3.0 respectively. Bulk viscosity β is set to be 1.0. The model consists of 4000 particles in all. Smoothing length is fixed and set to be 1.5 times the distance between two adjacent particles. The v_x is set to be 480 m/s. Resulting impact pressure on detonation end is around 3.4 GPa. Ambient temperature is 25℃.

The simulation is shown in Figure 7.17(a), (b), (c), where shear viscosity α set to be 1.0, 2.0, 3.0 respectively.

It can be seen from Figure 7.17 that shear viscosity α has significant influence on simulation. As α increases , the oscillation at the peak is obviously suppressed. When α is set to be 3.0, the curves become quite smooth and the calculated peak pressure is close to experiment [24]. The calculated run-to-detonation distance is not obviously effected by variation of α.

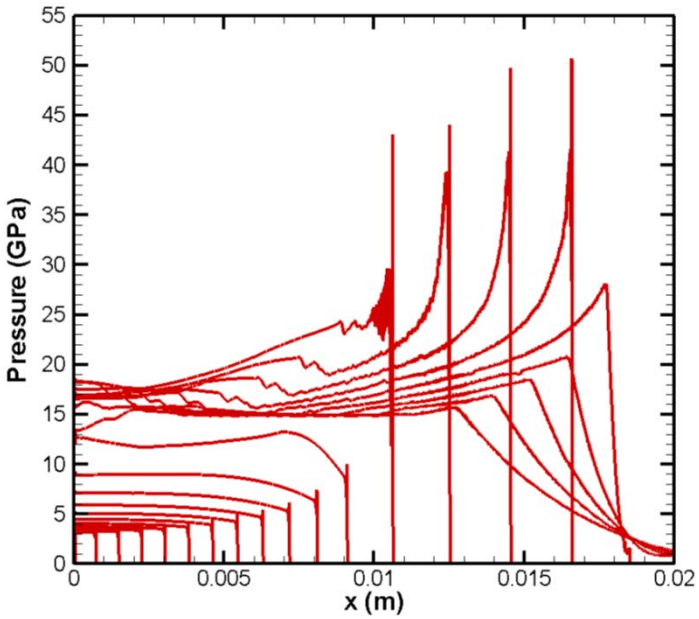

(a) $\alpha = 1.0, \beta = 1.0$

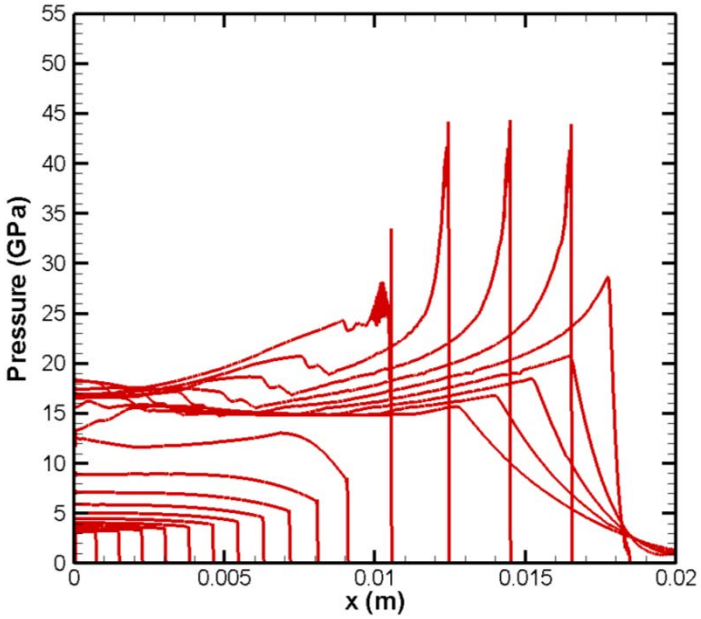

(b) $\alpha = 2.0, \beta = 1.0$

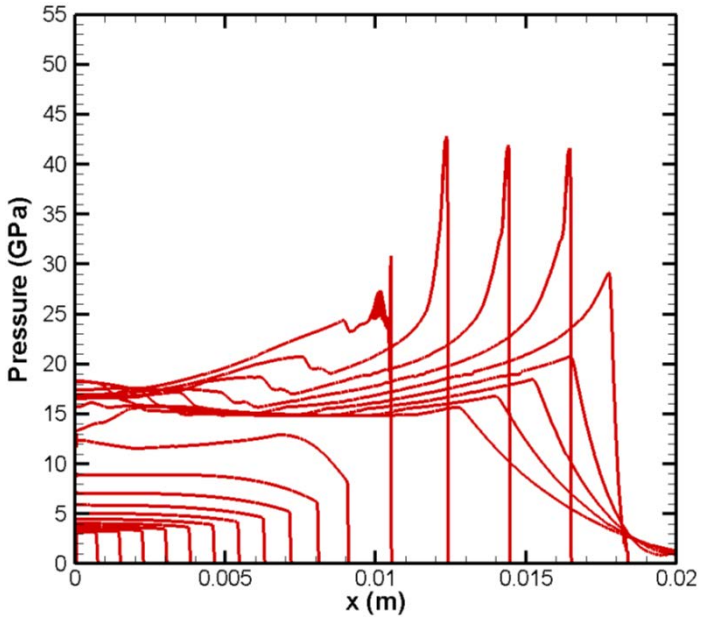

(c) $\alpha = 3.0, \beta = 1.0$

Figure 7.17 Influence of shear viscosity α on simulation. Impact velocity is 480 m/s. Ambient temperature is 25℃.

7.6.2 Influence of bulk viscosity β on simulation

In this section, bulk viscosity β is set to be 1.0, 2.0, 3.0 respectively. Shear viscosity α is set to be 1.0. Other configurations remain the same. The simulation is shown in Figure 7.18(a), (b), (c).

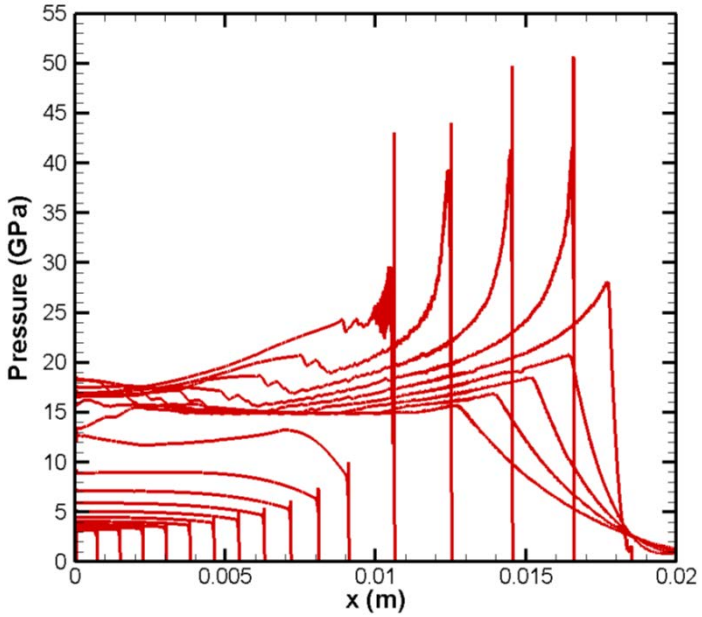

(a) $\alpha = 1.0, \beta = 1.0$

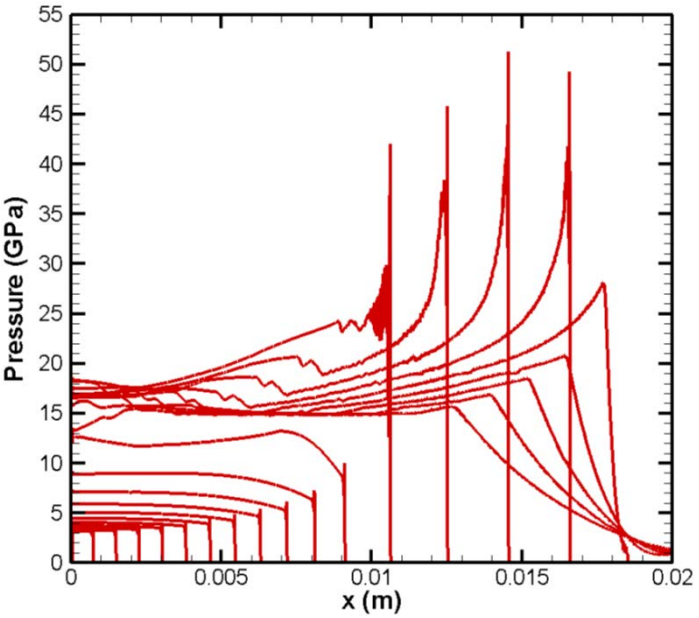

(b) $\alpha = 1.0, \beta = 2.0$

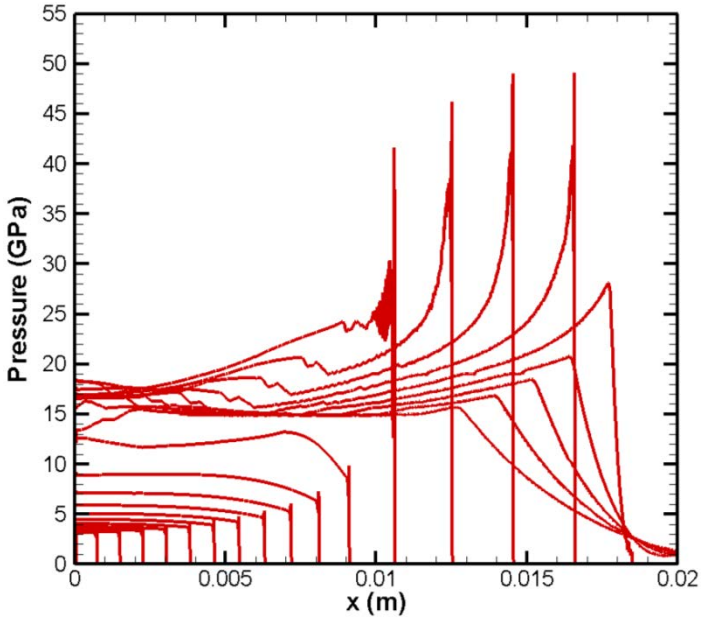

(c) $\alpha = 1.0, \beta = 3.0$

Figure 7.18 Influence of bulk viscosity β on SPH simulation. Impact velocity is 480 m/s. Ambient temperature is 25 ℃.

It can be seen from Figure 7.18 that bulk viscosity β has much less influence on simulation than shear viscosity α. Though β increases from 1 to 3, there is no significant reduction of oscillation at the peak. The calculated run-to-detonation distance is not obviously affected by variation of β.

7.6.3 Influence of number of particles on simulation

In this section, shear viscosity α is set to be 3.0, bulk viscosity β is set to be 1.0. The models consist of 2000, 4000, 8000 particles respectively. The other configurations are the same as mentioned in the previous sections. The simulation is shown in Figure 7.19(a), (b), (c).

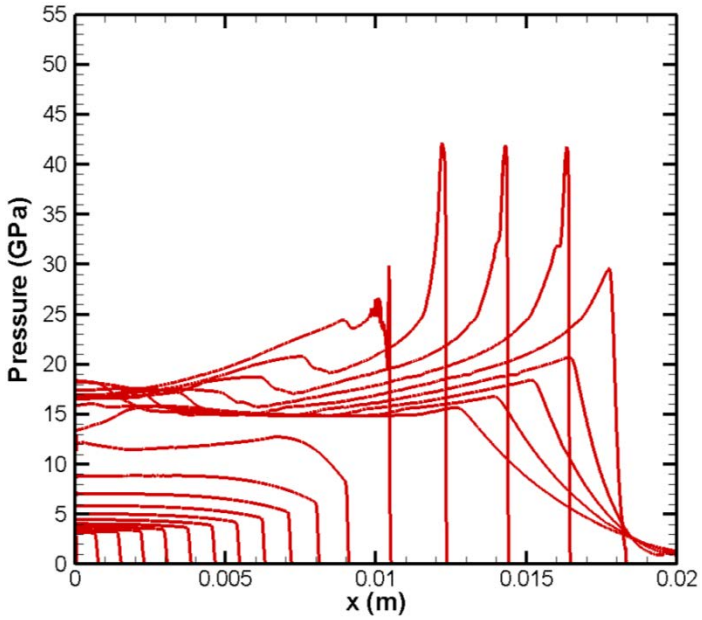

(a) Number of particles is 2000

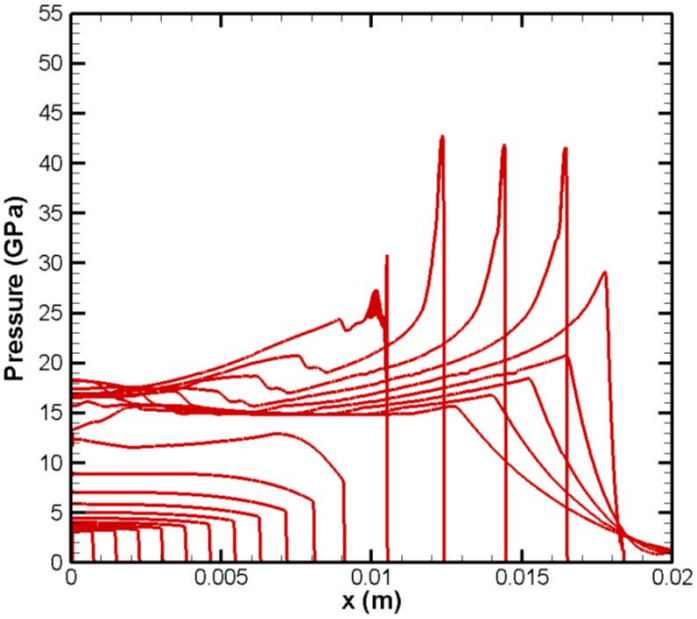

(b) Number of particles is 4000

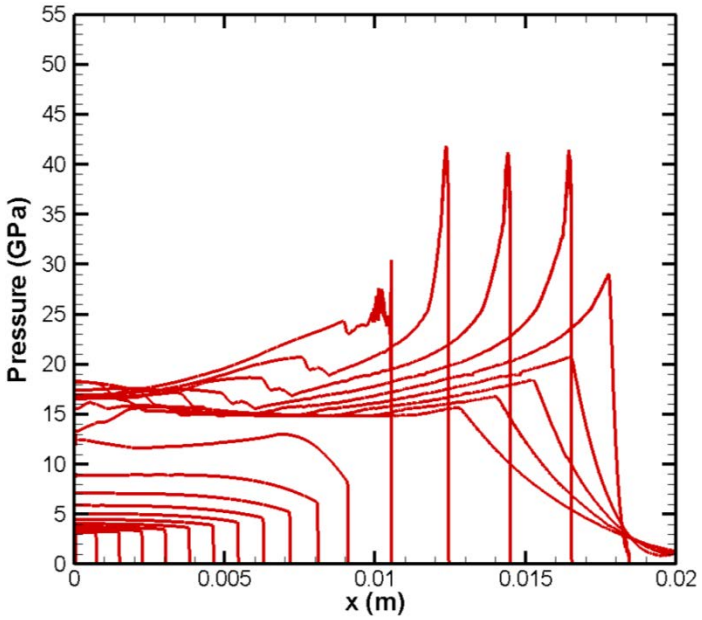

(c) Number of particles is 8000

Figure 7.19 Influence of number of particles on simulation. Impact velocity is 480 m/s. Ambient temperature is 25 ℃.

It can be seen from Figure 7.19 that the number of particles has substantial influence on the smoothness of the calculated curves. As the number of particles increases, the calculated curves become smoother. However, increasing particles can also decrease computational efficiency. Thus it needs to be balanced between accuracy and computational efficiency. According to Figure 7.19, 4000 particles is a reasonable choice for the one-dimensional model.

7.7 2D QM-MD-SPH simulation of high explosives

The EoSs of solid and gaseous of products of HMX obtained from MD simulation are applied in a two-dimensional SPH model of PBX 9501 bar. The fitted parameters of ignition and growth model are listed in Table 3.4 and Table 3.5. The model is 0.45 m in length, 0.025 m in radius. Initial smoothing length is set to be 1.5 times the distance between two neighboring particles. The v_x of leftmost particles are set to be 1000 m/s to detonate the explosive bar, as shown below. It should be noted that EoSs of solid and gaseous of products of HMX obtained from MD simulation are applied in the model.

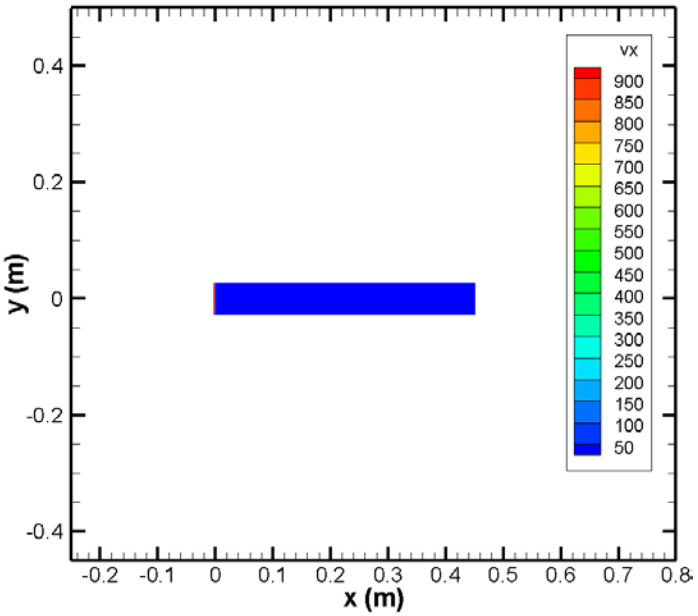

Figure 7.20 Two-dimensional SPH simulation using calculated EoSs.

The profile of the two-dimensional SPH model at different time is shown in Figure 7.21. The calculated peak pressure (~43 GPa) agrees well with experiment [24].

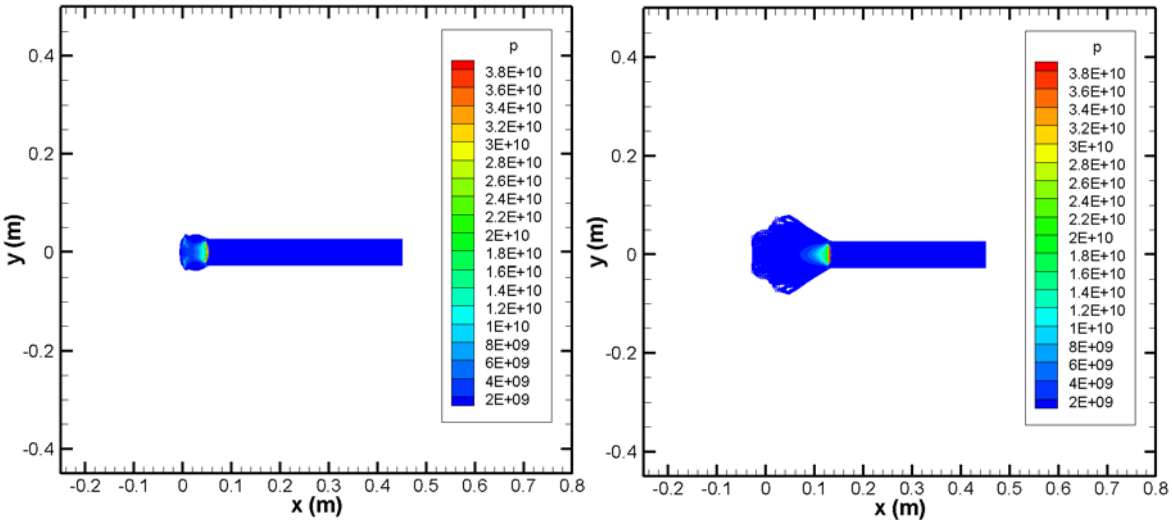

(a) 10 μs (b) 20 μs

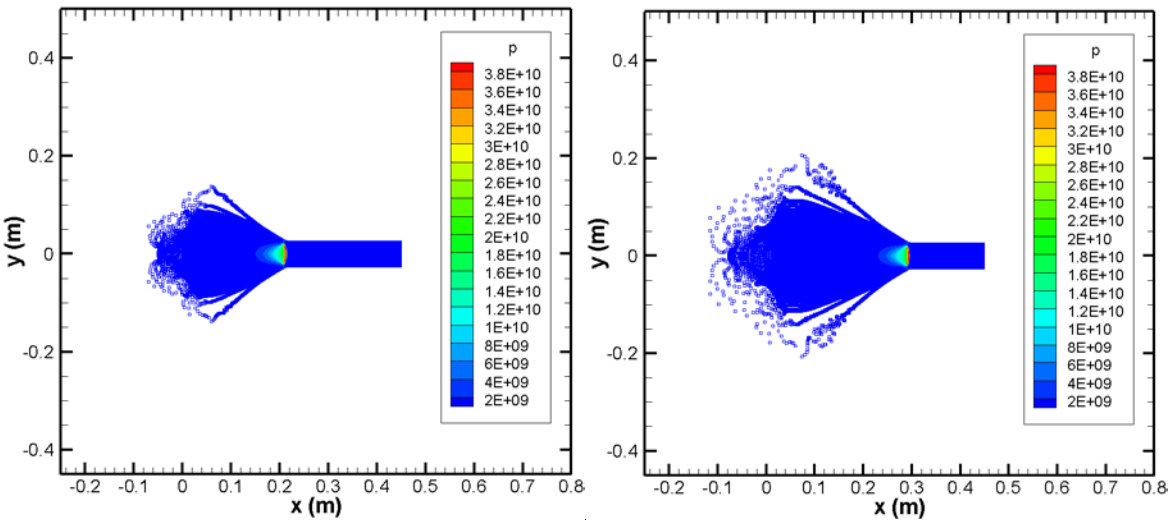

(c) 30 μs (d) 40 μs

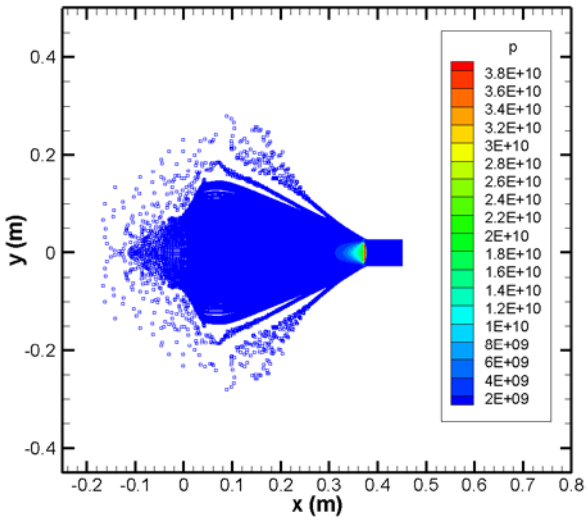

(e) 50 μs

Figure 7.21 The profile of the two-dimensional SPH model at different time

The distribution of reaction, v_x, density and smoothing length calculated by SPH at 50 μs is shown in Figure 7.22.

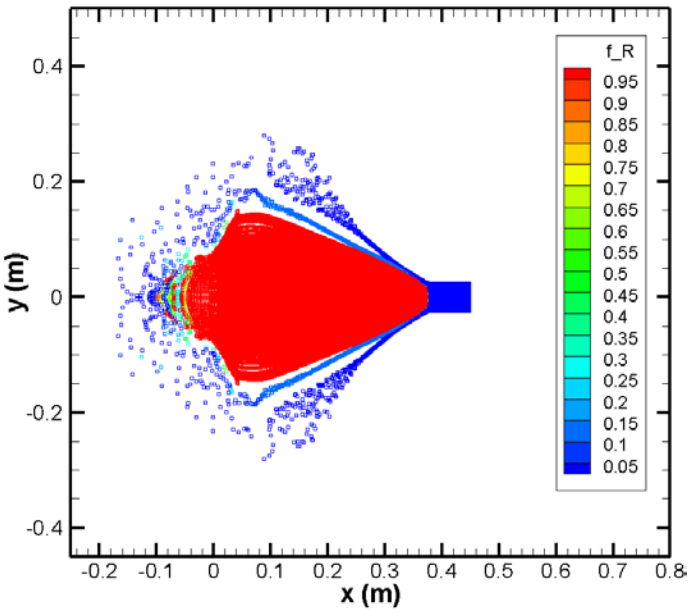

(a) Reaction

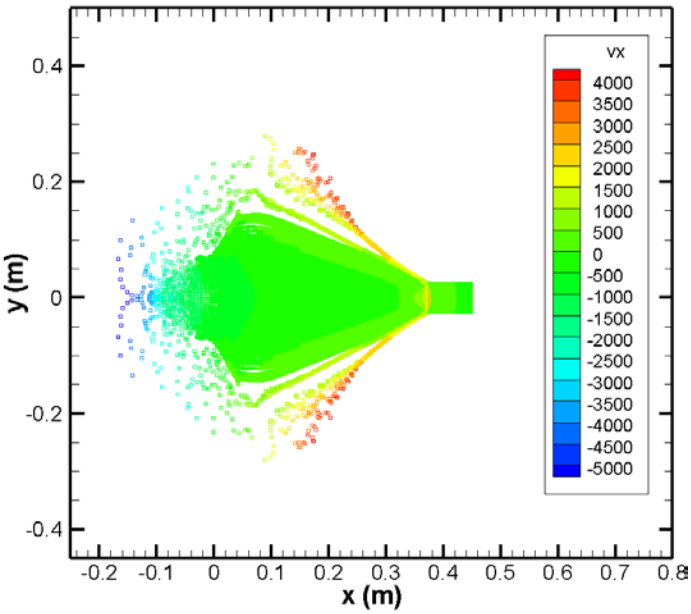

(b) v_x

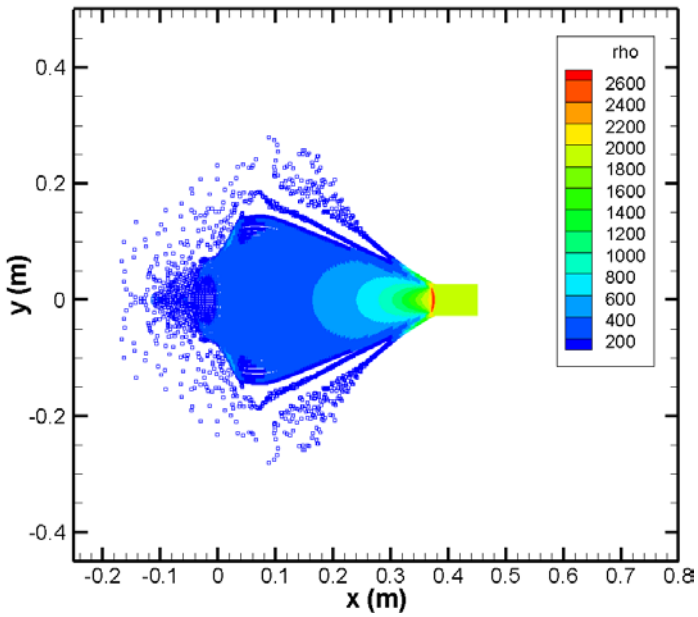

(c) Density

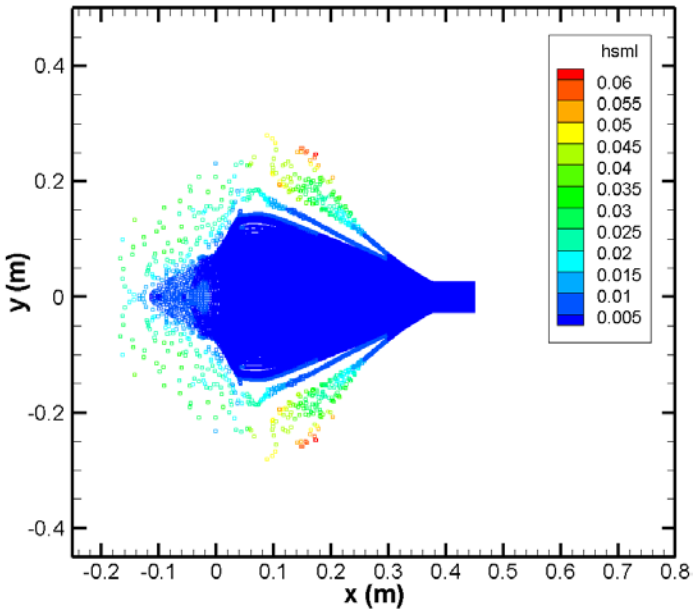

(d) Variable smoothing length

Figure 7.22 The distribution of reaction, v_x, density and smoothing length at 50 μs

7.8 QM-MD-SPH simulation of aluminized explosives

The addition of metal particles to energetic materials is a well-known means to improve detonation performance. Aluminum (Al) powders are widely used in pyrothchnics, rocket propellants and explosives, as shown in Figure 7.23. Al is added to propellants to increase thrust, while in explosive it enhances air blast and incendiary effect.

Figure 7.23 Fine aluminum powder (diameter ~20 μm).

Aluminized explosives are high explosives using micrometer-scale (5~10 μm) aluminum particles as additive. The mass fraction of aluminum particles ranges from 20% to 40% or even higher. Aluminized explosives feature both fast detonation and slow metal combustion. The detonation of high explosives occurs in microseconds, however, the combustion of aluminum particles generally takes milliseconds or even longer to finish. Thus, combustion of Al particles in aluminized explosives is assumed to occur behind detonation front, in other words, during the expansion of gaseous products. Al particles act as inert ingredients in the beginning stage of detonation [158]. According to the experiment conducted by Trzcinski et al. [159, 160], detonation velocity measurement of aluminized RDX shows that Al behaves in the reaction zone in the same manner as a chemical inert admixture. Therefore, different from ideal explosives like TNT, HMX, RDX, TATB, aluminized explosive is classified as non-ideal explosive. The high degree of secondary exothermal reactions occurring when the detonation products expand behind the detonation zone is a characteristic feature of non-ideal explosive. Due to the addition of aluminum particles, aluminized explosives have relatively low brisance but high blast potential [25].

The blast performance of energetic materials can be measured by *P-I* diagram, where *P* is peak pressure and *I* is the impulse, which is the time integral of the pressure generated by energetic materials. Explosion will be enhanced by Al powder since pressure will be prolonged in time compared with ordinary explosive. In addition, the heated surrounding air by gaseous products will also increase the pressure. When a warhead is detonated, for example, in a confined room, the structure will first experience a shock loading then a quasi-static pressure, which is determining factor for the structure damage. Optimal performance will be achieved when quasi static pressure is sufficiently high to breach

the structure. When gaseous products expand and turbulently mix with surrounding air, the temperature of the gases will drop fast and the combustion will be terminated. Thus, refined metal particles are preferred because they burn faster.

The detonation of aluminized explosive is very complicated phenomenon. The process includes reactions between gaseous products with Al powder, Al powder with surrounding air, gaseous products with surrounding air. The mechanism of the chemical reactions is still not thoroughly understood till today. Modeling the detonation and subsequent combustion requires a detailed knowledge of the chemical kinetics. Abundant research has been conducted on the topics, experimentally and numerically. Wilkins et al. obtained the Chapman-Jouguet pressure and EoS of PBX 9404 through experiments [27]. Wackerle et al. investigated the pressure history of PBX 9404 through planar shock initiation [28]. Cook et al. measured detonation pressure and detonation velocity of TNT-Al and other aluminized explosives [25]. Due to the complexity of the phenomenon, it takes longer time for researchers to understand the mechanism theoretically.

7.8.1 Afterburning model for combustion of aluminum particles

Numerical modeling of metalized explosives poses great challenge to simulation community due to the nature of chemically reacting multiphase flow. Afterburning model is a simplified model to describe the combustion of gaseous products, which is common in the simulation of combustion and detonation. Miller proposed the idea to combine ignition and growth model with afterburning model [161]. According to Miller, ignition and growth model is used to describe the detonation of high explosive, meanwhile, the afterburning model is used to describe the combustion of gaseous products or aluminum particles. Kuhl, Howard proposed a different idea, which introduces temperature in their afterburning model [31]. Thermodynamics code Cheetah is used to calculate the constituent of gaseous products of explosive. In addition, the specific internal energy of components of explosive gases is set to be negative at the beginning of the simulation, which is incompatible with ignition and growth model. The model has been used to study various explosives such as SDF_1 (an aluminized explosive, consisting of 45% $C_4H_8N_8O_8$, 35% Al, 20% C_4H_6) , SDF_2 (a polyethylene-based fuel, consisting of 17% $C_5H_8N_4O_{12}$, 17% Al, 66% C_4H_6). The drawback is that it is way too complicated and requires Cheetah to obtain extra information (constituent of gaseous products) needed for the subsequent simulation.

The model proposed by Miller is used in the work. The EoS for the gaseous products is modified to the form [32-35, 161]:

$$p_g = A_g e^{-R_{1g}V_g} + B_g e^{-R_{2g}V_g} + \frac{\omega_g(C_{Vg}T_g+\alpha Q)}{V_g} \qquad \text{Eqn. 7.34}$$

where p is pressure, V is volume ratio, and A, B, R_1, R_2, ω are parameters fitted from experiment, Q is the energy released in the combustion of aluminum particles, α represents the process of combustion [33]:

$$\frac{d\alpha}{dt} = a(1-\alpha)^{1/2}\left(\frac{p}{p_0}\right)^{1/6} \qquad \text{Eqn. 7.35}$$

where a is parameter fitted according to experiment, p_0 is atmospheric pressure. a is set to be 1950 in all simulation of aluminized explosive.

7.8.2 Numerical model for simulation of aluminized explosive

The aluminized explosive we study is HMX-Al, which consists of 69% HMX, 15% Al, 7.5% GAP, 7.5% FomblinD and 1% isonate.

The model is one-dimensional, which is similar to the one described in Figure 7.9. There are totally 2000 particles ($0.0292m$) in the model. The initial velocity of the aluminized explosive bar is 1000 m/s. Afterburning model is combined with ignition and growth model for the simulation of aluminized explosive. It is assumed that combustion of aluminum particles only occurs during the expansion of gaseous products.

The variation of pressure with time along the aluminized explosive bar is shown in Figure 7.24. From left to right, there are 10 curves in total and the time ranges from 1 μs to 10 μs.

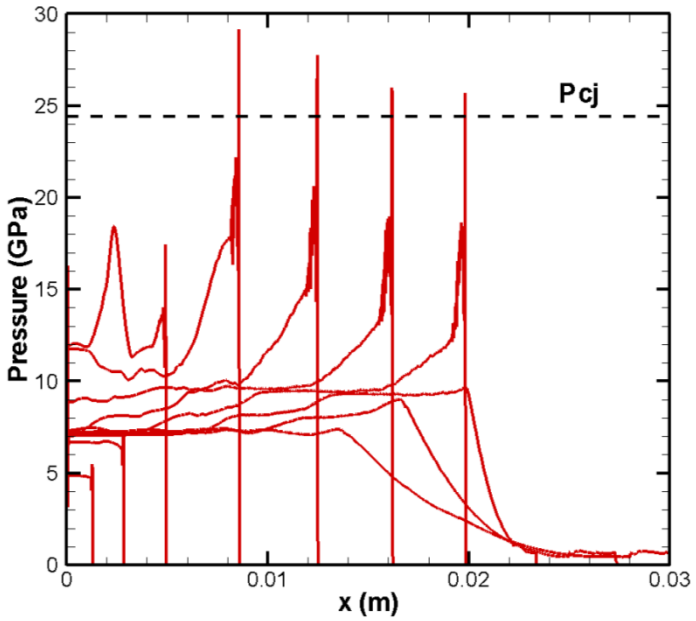

Figure 7.24 Variation of pressure with time along the aluminized explosive bar. Each curve represents the distribution of pressure at specific time.

The growth of shock wave can be clearly seen in Figure 7.24. From left to right, as shock wave propagates in explosive, chemical heat is gradually released and the shock wave is increasingly strengthened. Finally, the shock wave grows into self-sustained detonation wave. The calculated peak pressure is close to Chapman-Jouguet pressure obtained in experiment [162].

Compared to Figure 7.17(c), it can be seen from Figure 7.24 that peak pressure of aluminized explosive is reduced from 40 GPa to around 25 GPa. This is because Al powder does not engage in reaction in the beginning stage of detonation, it takes longer for Al powder to combust than that needed for the detonation of high explosive. Thus, during detonation of high explosive, Al powder does not contribute to peak pressure, as shown in Figure 7.25. However, Al powder is beneficial for the long-lasting heat release. The comparison of reaction progress of HMX and aluminum at 5 μs is shown in Figure 7.25.

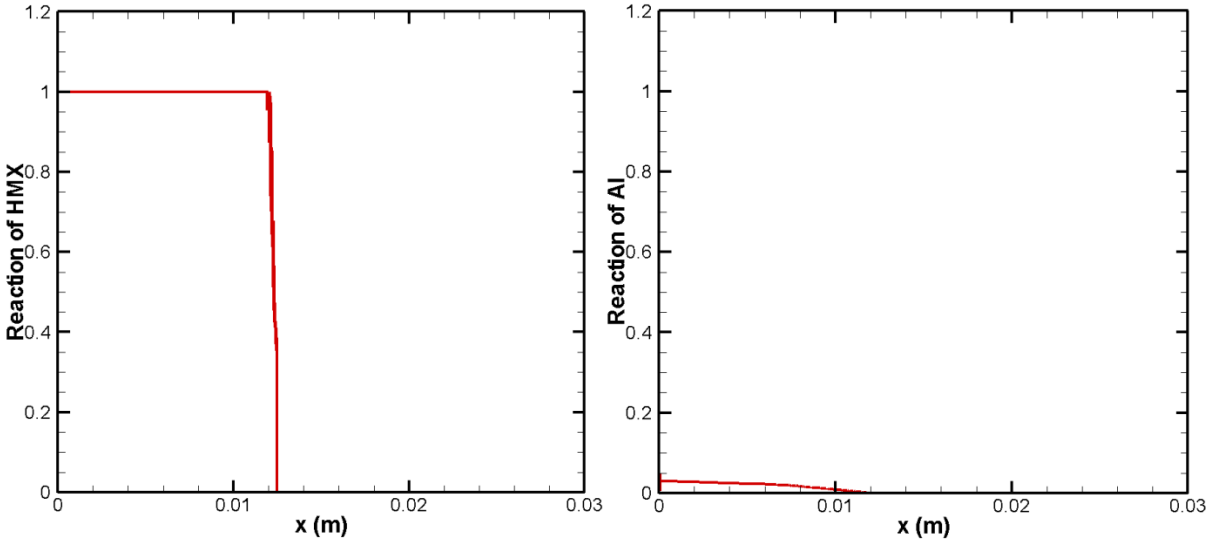

(a) Reaction of HMX (b) Reaction of aluminum particles

Figure 7.25 Comparison of reaction progress of HMX and aluminum particles at 5 μs

It can be seen that compared with high explosive, the reaction of aluminum particles is much slower. The distribution of pressure, x-velocity and density at 5 μs is shown in Figure 7.26.

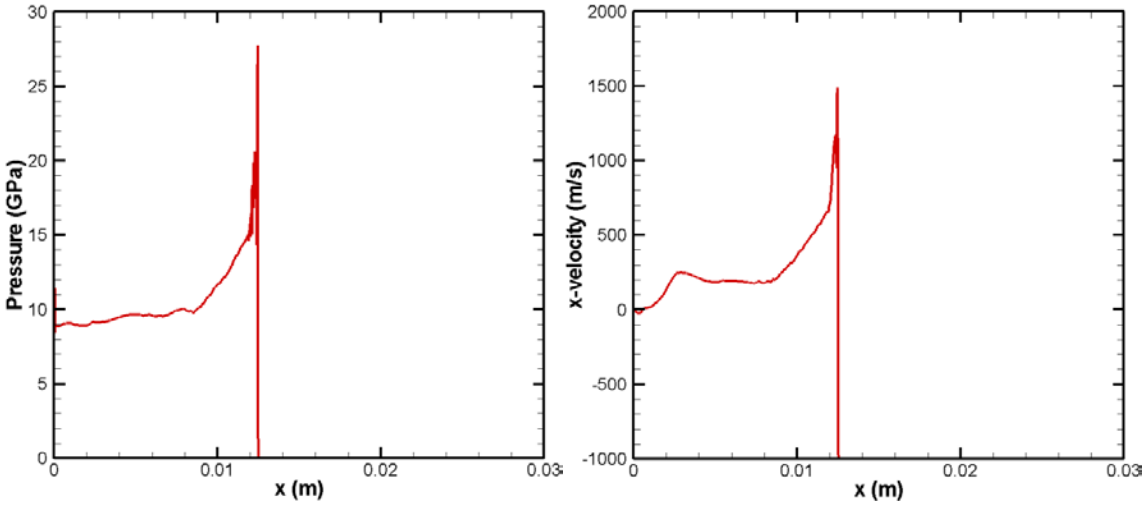

(a) Pressure (b) x-velocity

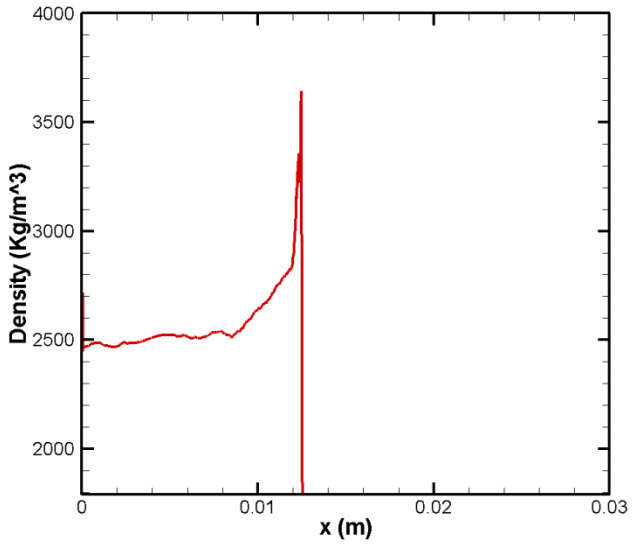

(c) Density

Figure 7.26 Distribution of pressure, x-velocity and density along the explosive bar

The pressure history at different locations away from detonation end is shown in Figure 7.27. It can be seen that the pressure decreases rapidly with distance.

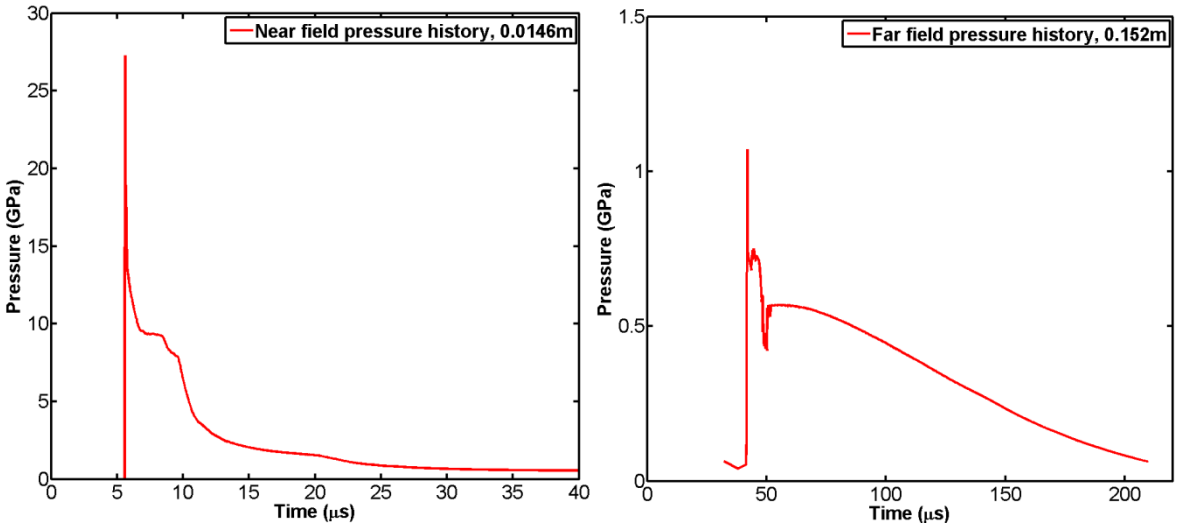

(a) Pressure history at near field (b) Pressure history at far field

Figure 7.27 Pressure history of HMX-Al at near field and far field

To investigate the influence of mass fraction of Al on performance of aluminized explosive, series of simulation is conducted, as shown in Table 7.2.

Table 7.2 Aluminized explosives with different mass fraction of Al

	HMX+0%Al	5%Al	10%Al	15%Al	20%Al
HMX (Kg)	1424.9	1363.4	1300.2	1234.9	1167.7
Al (Kg)	0	86.83	176.28	268.47	363.52
Others (Kg)	286.4	286.4	286.4	286.4	286.4

All the simulations have the same configuration except the mass fraction of aluminum.

The influence of mass fraction of Al on pressure history at near field and far field is shown in Figure 7.28.

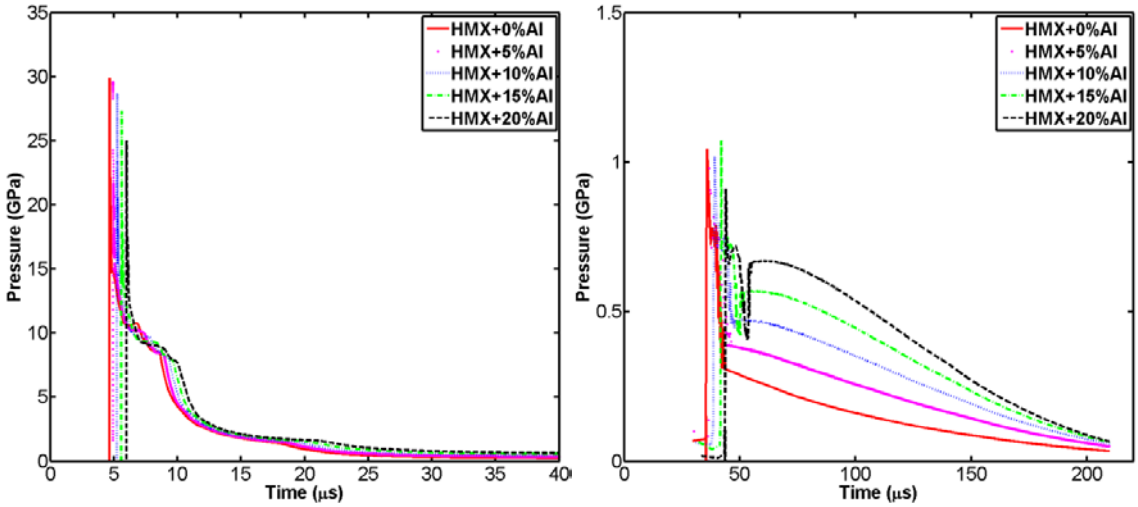

(a) 0.0146 m (b) 0.152 m

Figure 7.28 Influence of mass fraction of Al powder on pressure history at near field and far field

The variation of peak pressure with mass fraction of Al is shown in Figure 7.29.

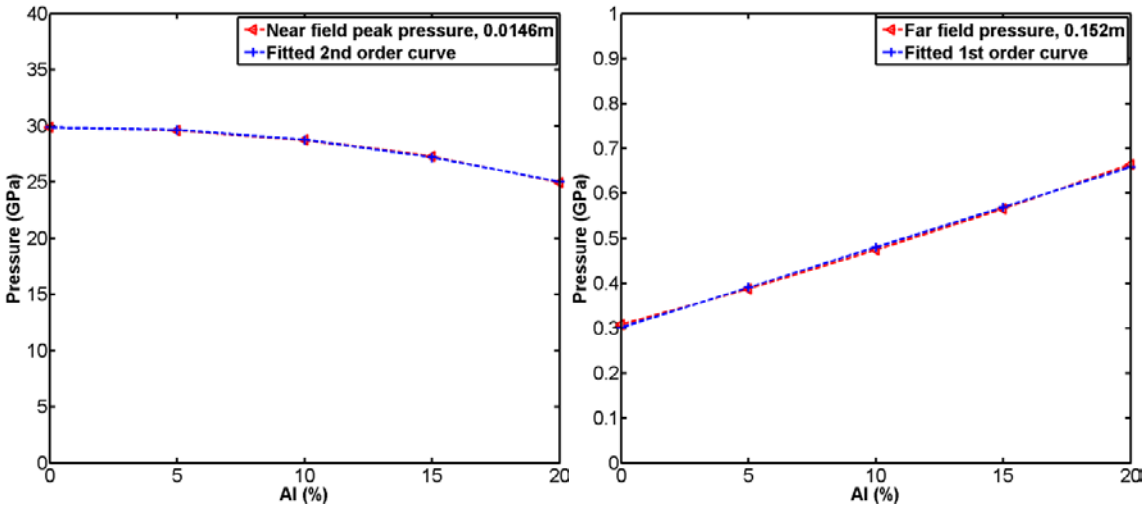

(a) Peak pressure in near field (b) Pressure in far field

Figure 7.29 Variation of peak pressure with mass fraction of aluminum

It can be seen from Figure 7.29(a) that with the increase of Al, the peak pressure at near field is reduced, which agrees with prior analysis. In the far field, the tendency is reversed, as shown in Figure 7.29(b). As time passes by, increasing number of Al particles start to combust and more heat is released, enhancing the pressure at far field. Second order curve and first order curve are used to fit the near field pressure and the far field pressure respectively as follow.

$$\begin{cases} p_{near} = -0.0133w^2 + 0.0215w + 29.8731, & 0 \le w \le 20 \\ p_{far} = 0.0179w + 0.3010, & 0 \le w \le 20 \end{cases} \quad \text{Eqn. 7.36}$$

The variation of impulse with mass fraction of aluminum is shown in Figure 7.30. Second order curve is used to fit the original curve. According to the fitted curve, the optimal performance (maximum impulse) is achieved when mass fraction of Al powder is 44.06%. The fitted formula is as below:

$$I_{far} = -26w^2 + 2291w + 22547, 0 \le w \le 20 \quad \text{Eqn. 7.37}$$

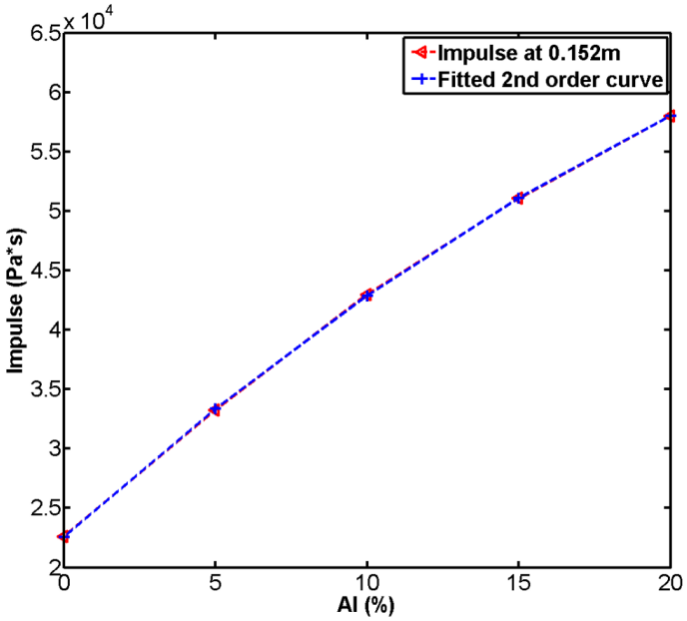

Figure 7.30 Variation of impulse with mass fraction of aluminum

The JWL EoSs of solid and gaseous products of HMX obtained from molecular dynamics simulations are applied to study the influence of mass fraction of Al powder on aluminized explosive, as shown in Figure 7.31. The configurations of the model are similar to the previous one.

Table 7.3 Aluminized explosives with different mass fraction of aluminum

	HMX+10%Al	11% Al	12%Al	13%Al	14%Al	15%Al
HMX (Kg)	1300.2	1287.3	1274.3	1261.3	1248.1	1234.9
Al (Kg)	176.28	194.50	212.82	231.26	249.81	268.47
Others (Kg)	286.4	286.4	286.4	286.4	286.4	286.4

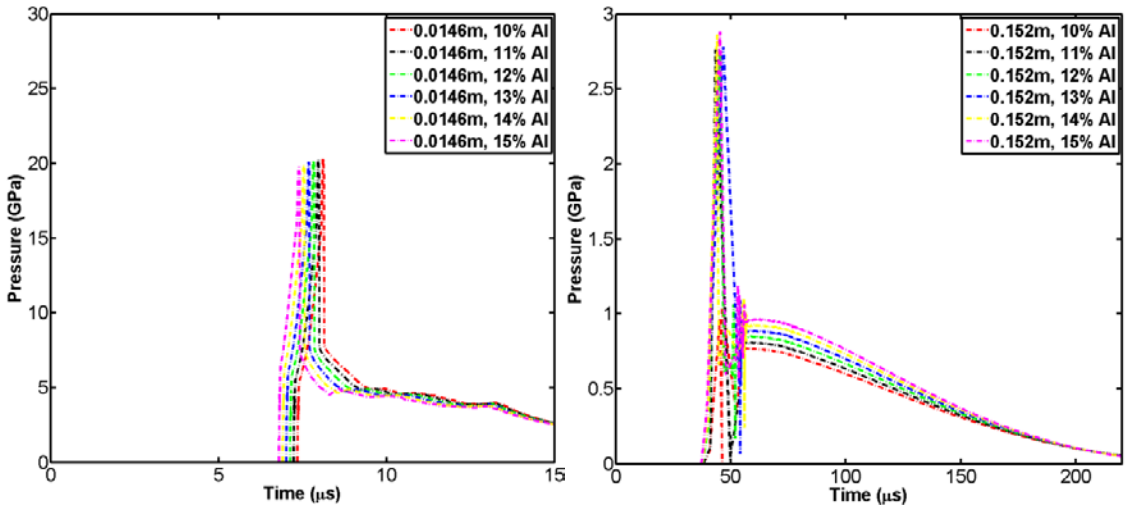

(a) 0.0146 m (b) 0.152 m

Figure 7.31 Influence of mass fraction of Al powder on pressure history at near field and far field.

7.9 SPH simulation of cylinder test

The cylinder test has long been the principal method to obtain EoS parameters for high explosives. In this section, a two-dimensional SPH model of cylinder test is built. The internal diameter of the cylinder-test device is 2.54 cm, the external diameter is 3.06 cm and the length is 31.00 cm. In the experiment, radial displacement of copper wall is recorded.

The two-dimensional model is shown in Figure 7.32(a), where red particles represent copper and blue particles represent PBX 9501. The v_x of PBX 9501 particles on the left side (red) are set to be 2000 m/s, as shown in Figure 7.32(b). In the simulation, the radial displacement of copper wall 0.2 m away from detonation end is recorded and compared with experiment.

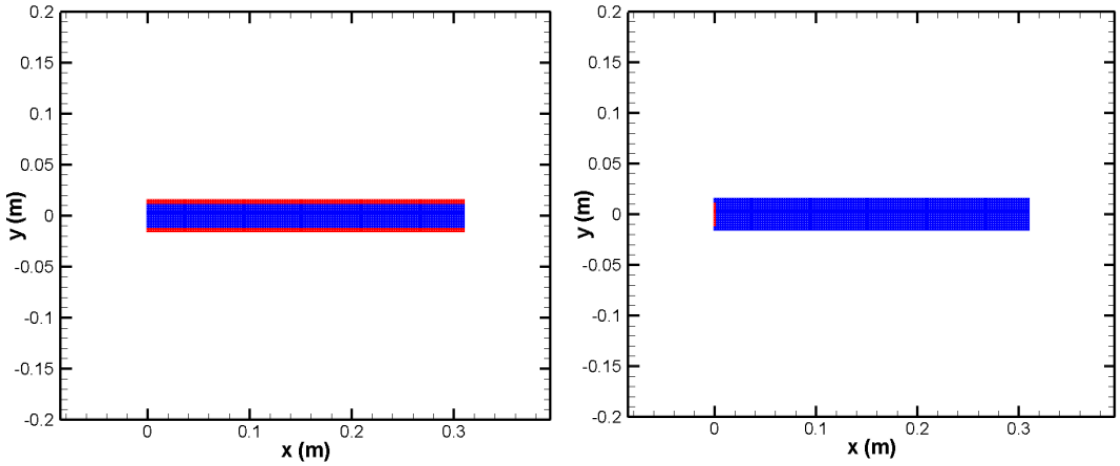

(a) Two-dimensional SPH model (b) Initial condition

Figure 7.32 Two-dimensional SPH model of cylinder test

The parameters of JWL EoSs of solid and gaseous products of PBX 9501 are listed in Table 6.1 and Table 6.2 respectively. The parameters of reaction rate equation are listed in Table 7.1.

Johnson-Cook constitutive model is used to describe the flow behavior of copper. Johnson-Cook model is an empirical model used to calculate flow stress of solid materials subject to large strains, high strain rates and high temperature [154]. The parameters in JC model for copper are listed as below:

Table 7.4 Parameters in the JC model for copper [154]

$A(MPa)$	$B(MPa)$	C	n	m	$T_{\mathrm{room}}(K)$	$T_{\mathrm{melt}}(K)$
89.63	291.6	0.025	0.31	1.09	294	1356

In the implementation of SPH code, Mie-Gruneisen EoS is used to calculate the pressure of copper under shock loading. The parameters in Mie-Gruneisen EoS for copper are listed in Table 7.5 [163, 164]:

Table 7.5 Parameters in the MG EoS for copper [163, 164]

$\rho_0(kg/m^3)$	$c(m/s)$	s	$G(GPa)$	γ
8940	3940	1.49	47.7	1.96

The simulation result is shown in Figure 7.33, where red particles represent copper and blue particles represent PBX 9501. Shear viscosity α is set to be 1, bulk viscosity β is set to be 1, φ is set to be 0.1.

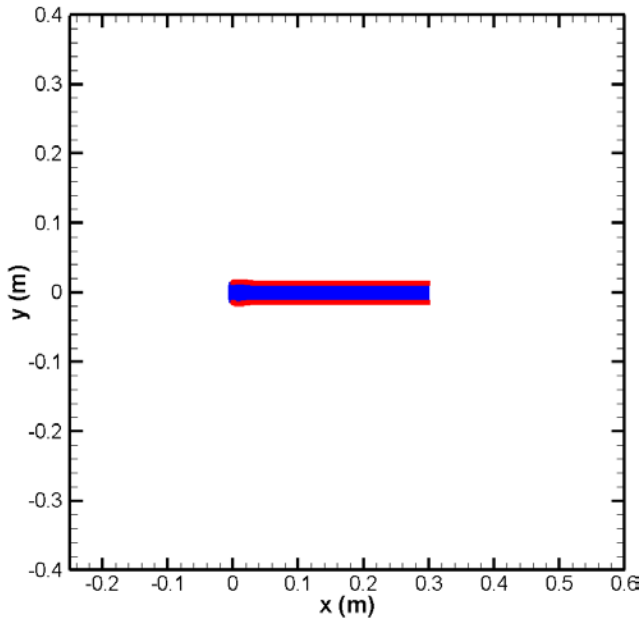

(a) 0.5 μs

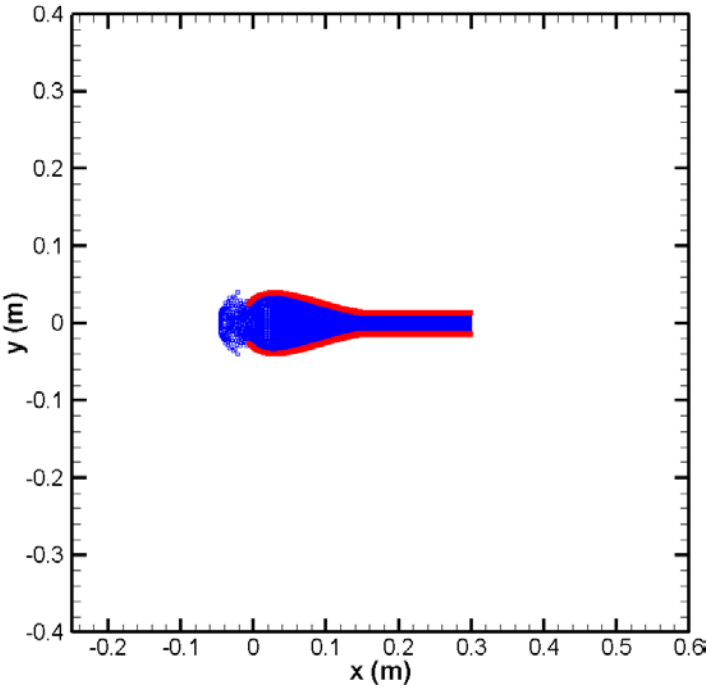

(b) 20 μs

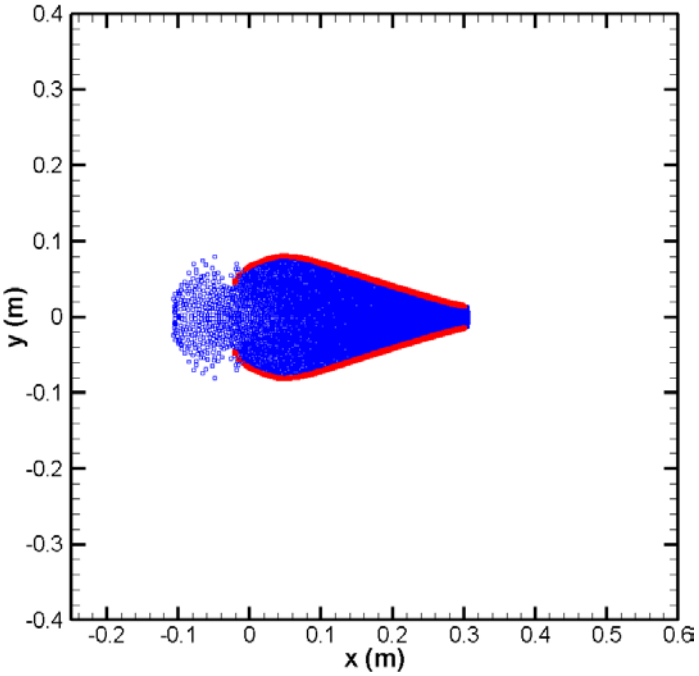

(c) 40 μs

Figure 7.33 Expansion of gaseous products and copper wall at different time

From Figure 7.33 it can be observed that with the expansion of explosive products, the copper wall is gradually dilated and breached.

The distribution of v_x, density ρ, pressure p at 40 μs are shown in Figure 7.34.

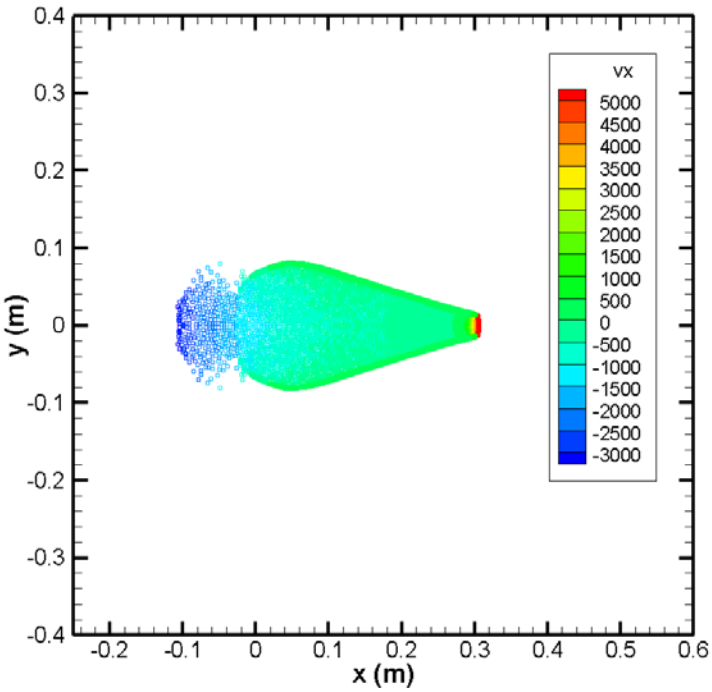

(a) Distribution of v_x

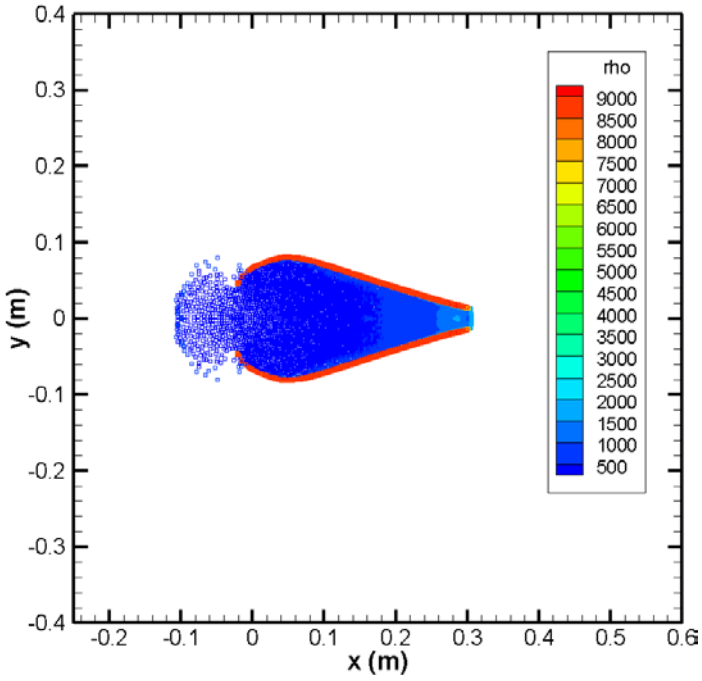

(b) Distribution of ρ

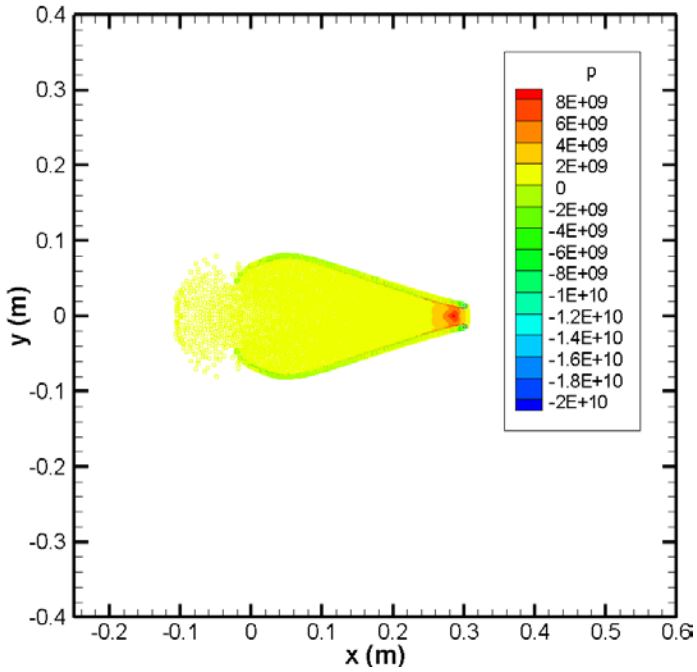

(c) Distribution of p

Figure 7.34 Distribution of various properties at 40 μs

The radial displacement of copper wall located at 0.2 m away from detonation point is compared with experiment [165], as shown in Figure 7.35.

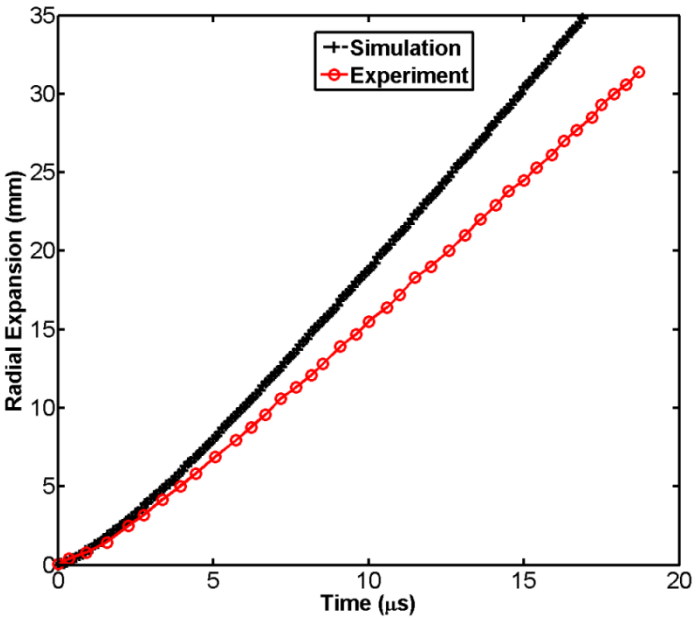

Figure 7.35 Comparison of calculated radial displacement of copper wall with experiment

According to Figure 7.35, the radial displacement of copper wall obtained from simulation does not agree very well with experiment. This is probably because the SPH model is two-dimensional. In addition, accurate simulation of cylinder test requires more complex models, such as failure model for copper wall.

Chapter 8-SPH using Godunov scheme

In the beginning development of SPH method, artificial viscosity is introduced to suppress unphysical fluctuation. Afterwards, it is widely accepted as a standard means to simulate discontinuous phenomenon such as shock waves. Abundant literature can be found on the application of SPH with artificial viscosity [166-170]. However, the parameters (shear viscosity and bulk viscosity) of artificial viscosity need to be tuned before each simulation, which can be quite time-consuming. Furthermore, artificial viscosity only suppresses unphysical fluctuation instead of eliminating them thoroughly. Under certain circumstances, artificial viscosity may not function and cause catastrophic failure. Therefore, an innovative technique is required to eliminate artificial viscosity in traditional SPH algorithm.

The Riemann solver in computational fluid dynamics (CFD) has inspired researchers a lot. Godunov proposed a numerical scheme to solve exact or approximate Riemann problem in CFD in 1959 [171].Various Riemann solvers have been proposed since then, such as Roe solver, HLLE solver, HLLC solver and so on [172], which inspires researchers to introduce Godunov's method in traditional SPH method to replace artificial viscosity. For example, Inutsuka proposed the idea to apply Godunov's method in SPH method [173, 174]. Afterwards, Monaghan discussed the feasibility of applying Riemann solver in SPH method [175]. Inspired by Monaghan's idea, Parshikov rearranged the governing equations and introduced approximate Riemann solver in traditional SPH method and his method yields reasonably good results [176, 177]. Cha et al. implemented and reviewed several types of Godunov SPH [178]. Since then, Godunov SPH has been increasingly applied in hydrodynamics and other problems, which can be found in [179-181].

Detonation of high explosives (such as HMX, PBX 9404, PBX 9501) is an extreme phenomenon containing complicated chemical reactions and strong discontinuity such as shock wave [2]. It is not only hazardous but also expensive to conduct experiment on explosives. Thus, numerical investigation of high explosive has long been the interest of researchers. Tarver and McGuire proposed ignition and growth model and applied the model in the study of detonation waves of high explosive such as TNT, TATB, LX-17, PBX 9404 [3, 4, 182-185]. Since the proposal of ignition and growth model, it has been the most popular mathematical model to describe detonation of high explosives and incorporated in commercial software such as ANSYS LS-DYNA. Kapila et al. described the ignition and growth model in a finite-volume method and applied the model in simulation of LX-17 [186]. Souers described a simplified reactive flow model (JWL++ model) and used the model to study size effect of ANFO K1 [6]. However, JWL++ model uses simple mixture rule instead of making real physical assumptions in the description of detonation, which makes it much less accurate than ignition and growth model. Garcia and Tarver further

described a three-dimensional ignition and growth reactive flow model of PBX 9502 and compared the simulation with experiment [187]. In this section, a Godunov SPH which integrates ignition and growth model is proposed to investigate the detonation of PBX 9501. The proposed method can be extended to other high explosives such as PBX 9404 and so on.

8.1 Governing equations of Godunov SPH

The governing equations in traditional SPH (viscous shear stress is neglected in the equations) can be written as

$$\frac{\mathrm{d}\rho_i}{\mathrm{d}t} = \sum_{j=1}^{N} \frac{m_j \rho_i}{\rho_j} (\boldsymbol{v}_i - \boldsymbol{v}_j) \cdot \nabla_i W_{ij} \qquad \text{Eqn. 8.1}$$

$$\frac{\mathrm{d}\boldsymbol{v}_i}{\mathrm{d}t} = -\sum_{j=1}^{N} \frac{m_j (p_i + p_j)}{\rho_j \rho_i} \nabla_i W_{ij} \qquad \text{Eqn. 8.2}$$

$$\frac{\mathrm{d}e_i}{\mathrm{d}t} = \frac{1}{2} \sum_{j=1}^{N} \frac{m_j (p_i + p_j)}{\rho_j \rho_i} (\boldsymbol{v}_i - \boldsymbol{v}_j) \cdot \nabla_i W_{ij} + \dot{q} \qquad \text{Eqn. 8.3}$$

where W_{ij} is kernel function, ρ is density, $\boldsymbol{v}$ is velocity, p is pressure, e is specific internal energy, $\dot{q}$ is heat release rate, t is time.

In SPH, the kernel W_{ij} is a function of $\left|\boldsymbol{r}_i - \boldsymbol{r}_j\right| / h$ (h is smoothing length), its gradient is written as

$$\nabla_i W_{ij}\left(\frac{\left|\boldsymbol{r}_i - \boldsymbol{r}_j\right|}{h}\right) = W_{ij}' \frac{\boldsymbol{r}_i - \boldsymbol{r}_j}{h\left|\boldsymbol{r}_i - \boldsymbol{r}_j\right|} \qquad \text{Eqn. 8.4}$$

where

$$\boldsymbol{v} = \frac{d\boldsymbol{r}}{dt} \qquad \text{Eqn. 8.4a}$$

To introduce Riemann solver in SPH, it is assumed that a discontinuity exists in the middle of each particle pair, for example, particle i and particle j, as shown in Figure 8.1.

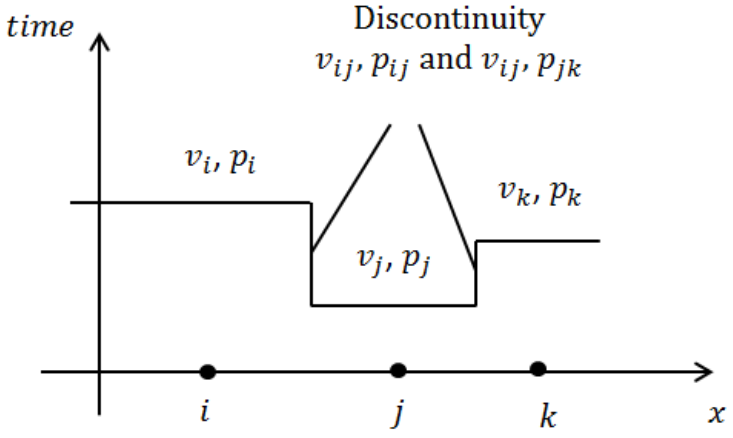

Figure 8.1 Scheme of one-dimensional Godunov method

The velocity and pressure at the discontinuity can be computed using the following approximations [177]:

$$v_{ij}^{*R} = \frac{v_j^R \rho_j c_j + v_i^R \rho_i c_i - p_j + p_i}{\rho_j c_j + \rho_i c_i} \qquad \text{Eqn. 8.5}$$

$$p_{ij}^{*} = \frac{p_j \rho_i c_i + p_i \rho_j c_j - \rho_j c_j \rho_i c_i (v_j^R - v_i^R)}{\rho_j c_j + \rho_i c_i} \qquad \text{Eqn. 8.6}$$

where c is sound velocity, v^R is written as

$$v^R = \boldsymbol{v} \cdot \frac{\boldsymbol{r}_j - \boldsymbol{r}_i}{\left|\boldsymbol{r}_j - \boldsymbol{r}_i\right|} \qquad \text{Eqn. 8.6a}$$

The Riemann solver is introduced in traditional SPH via the substitution:

$$\frac{1}{2}(v_i^R + v_j^R) \to v_{ij}^{*R} \qquad \text{Eqn. 8.7}$$

$$\frac{1}{2}(p_i + p_j) \to p_{ij}^{*} \qquad \text{Eqn. 8.8}$$

Thus, after rearrangements, the continuity, momentum, modified energy equations of Godunov SPH can be described as below [188]:

$$\frac{\mathrm{d}\rho_i}{\mathrm{d}t} = -\sum_{j=1}^{N} \frac{m_j \rho_i}{\rho_j h} \left(v_i^R - v_{ij}^{*R} + \frac{1}{2}(v_i^R - v_j^R) \right) W_{ij}' \qquad \text{Eqn. 8.9}$$

$$\frac{\mathrm{d}\boldsymbol{v}_i}{\mathrm{d}t} = 2\sum_{j=1}^{N} \frac{m_j p_{ij}^{*}}{\rho_j \rho_i h} W_{ij}' \frac{\boldsymbol{r}_j - \boldsymbol{r}_i}{\left|\boldsymbol{r}_j - \boldsymbol{r}_i\right|} \qquad \text{Eqn. 8.10}$$

$$\frac{\mathrm{d}e_i}{\mathrm{d}t} = -2\sum_{j=1}^{N} \frac{m_j p_{ij}^{*}}{\rho_j \rho_i h} (v_i^R - v_{ij}^{*R}) W_{ij}' + \dot{q} \qquad \text{Eqn. 8.11}$$

8.2 Artificial viscosity in traditional SPH

In traditional SPH, to simulate the transformation of kinetic energy to heat energy, Monaghan type artificial viscosity Π_{ij} is introduced [150, 151], which can be expressed as

$$\Pi_{ij} = \begin{cases} \dfrac{-\alpha \overline{c}_{ij} \phi_{ij} + \beta \phi_{ij}^2}{\overline{\rho}_{ij}} & , \quad \boldsymbol{v}_{ij} \cdot \boldsymbol{x}_{ij} < 0 \\ 0 & , \quad \boldsymbol{v}_{ij} \cdot \boldsymbol{x}_{ij} \geq 0 \end{cases} \qquad \text{Eqn. 8.12}$$

where

$$\phi_{ij} = \frac{h_{ij}\boldsymbol{v}_{ij}\boldsymbol{x}_{ij}}{\left|\boldsymbol{x}_{ij}\right|^2 + \varphi^2} \quad \text{Eqn. 8.12a}$$

$$\overline{c_{ij}} = \frac{1}{2}(c_i + c_j) \quad \text{Eqn. 8.12b}$$

$$\overline{\rho_{ij}} = \frac{1}{2}(\rho_i + \rho_j) \quad \text{Eqn. 8.12c}$$

$$h_{ij} = \frac{1}{2}(h_i + h_j) \quad \text{Eqn. 8.12d}$$

$$\boldsymbol{v}_{ij} = \boldsymbol{v}_i - \boldsymbol{v}_j \quad \text{Eqn. 8.12e}$$

$$\boldsymbol{x}_{ij} = \boldsymbol{x}_i - \boldsymbol{x}_j \quad \text{Eqn. 8.12f}$$

where α and β are constants. φ is used to prevent numerical divergences between two particles, c and $\boldsymbol{v}$ represent the speed of sound and particle velocity, respectively. The α and β need to be tuned before each simulation. In general cases, α and β are set to be 1, φ is set to be 0.1.

8.3 Ignition and growth model

The ignition and growth model is integrated in our SPH code. Compared with traditional JWL model which includes only a single equation of state for explosive gases, ignition and growth model employs JWL EoSs for both solid explosive and gaseous products of explosives [24]:

$$\begin{cases} p_s = A_s e^{-R_{1s}V_s} + B_s e^{-R_{2s}V_s} + \dfrac{\omega_s C_{Vs} T_s}{V_s} \\ p_g = A_g e^{-R_{1g}V_g} + B_g e^{-R_{2g}V_g} + \dfrac{\omega_g C_{Vg} T_g}{V_g} \end{cases} \quad \text{Eqn. 8.13}$$

where p is pressure, V is relative volume, T is temperature, C_V is average heat capacity, A, B, R_1 , R_2 and ω are parameters fitted based on experiment. s represents solid explosive and g represents gaseous products of explosive. The speed of sound is given by

$$c = \sqrt{\frac{\mathrm{d}p}{\mathrm{d}\rho}} \quad \text{Eqn. 8.14}$$

where p is pressure, ρ is density.

Two physical assumptions are introduced in ignition and growth model, which are temperature and pressure equilibrium, as shown below

$$\begin{cases} p_s = p_g \\ T_s = T_g \end{cases} \quad \text{Eqn. 8.15}$$

Temperature equilibrium is often used as a standard approach for closure in hydrocodes.

The reaction rate equation is written as [24]

$$\frac{\mathrm{d}\lambda}{\mathrm{d}t} = \underbrace{I(1-\lambda)^b\left(\frac{\rho}{\rho_0}-1-a\right)^x}_{0<\lambda\le\lambda_{ig\max}} + \underbrace{G_1(1-\lambda)^c\lambda^d p^y}_{0<\lambda\le\lambda_{G1\max}} + \underbrace{G_2(1-\lambda)^e\lambda^g p^z}_{\lambda_{G2\min}\le\lambda<1} \qquad \text{Eqn. 8.16}$$

where I, a, b , x, c, d, y , e, g, z, G_1 , G_2 , $\lambda_{ig\max}$, $\lambda_{G1\max}$, $\lambda_{G2\min}$ are rate constants fitted based on experiment, ρ is real-time density of explosive particle during simulation.

In the implementation of ignition and growth model, the state of explosive can be described by reaction progress λ , which is a number between 0 and 1. 0 represents solid explosive, while 1 represents fully reacted explosive products. The number between 0 and 1 represents explosion products in mixing state.

8.4 Benchmark test for Godunov SPH

A one-dimensional shock tube problem is used as benchmark to validate the Godunov SPH algorithm. The initial conditions of the shock tube problem is described as [157]

$$\begin{cases}\rho = 1, v = 0, e = 2.5, p = 1 & when\ x \le 0\\ \rho = 0.25, v = 0, e = 1.795, p = 0.1795 & when\ x > 0\end{cases} \qquad \text{Eqn. 8.17}$$

800 particles are used in the simulation. All particles have the same mass of $m_i = 0.001875$. 640 particles are distributed in the high-density area ranging from -0.6 to 0, while 160 particles are distributed in the low-density area ranging from 0 to 0.6. Time step is 0.005 s and total steps are 40. Artificial viscosity is applied when using the traditional SPH. The comparison of results obtained by traditional SPH with that obtained by Godunov SPH is shown below

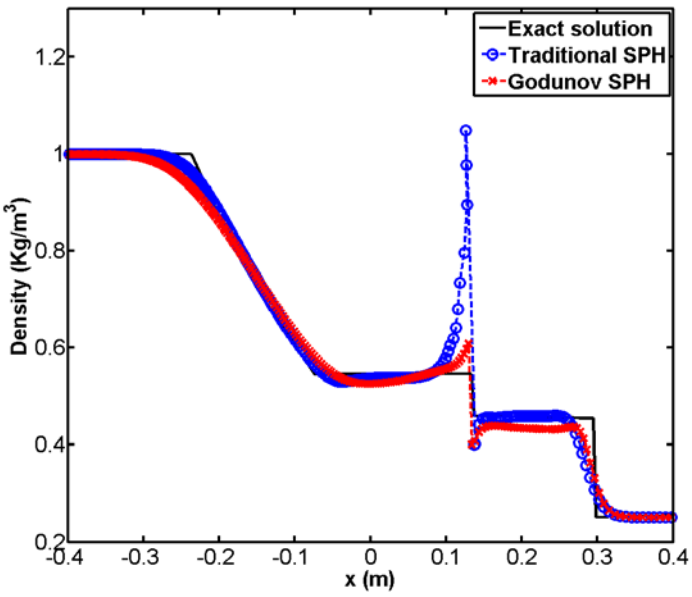

(a) Comparison of density calculated by traditional SPH with artificial viscosity, Godunov SPH with exact solution

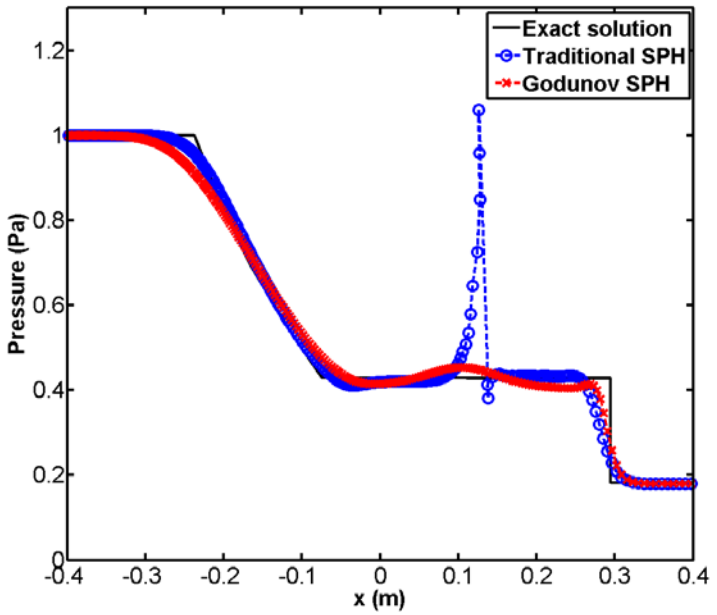

(b) Comparison of pressure calculated by traditional SPH with artificial viscosity, Godunov SPH with exact solution

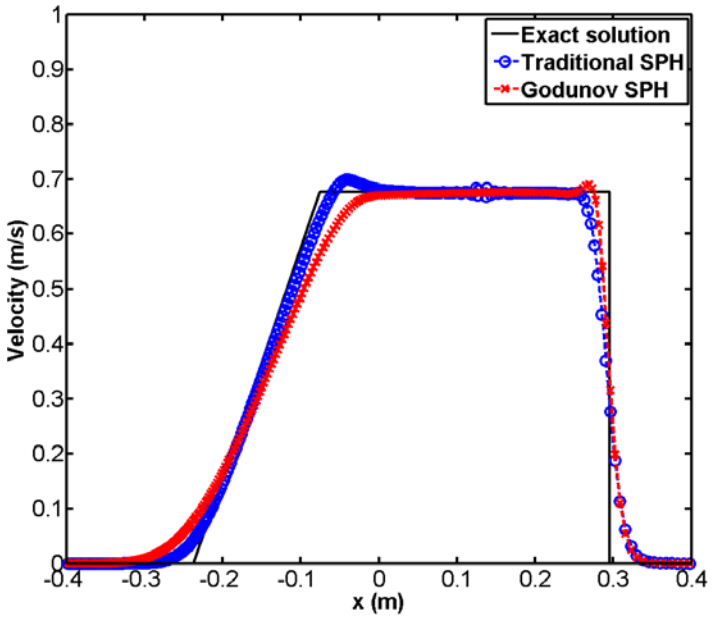

(c) Comparison of velocity calculated by traditional SPH with artificial viscosity, Godunov SPH with exact solution

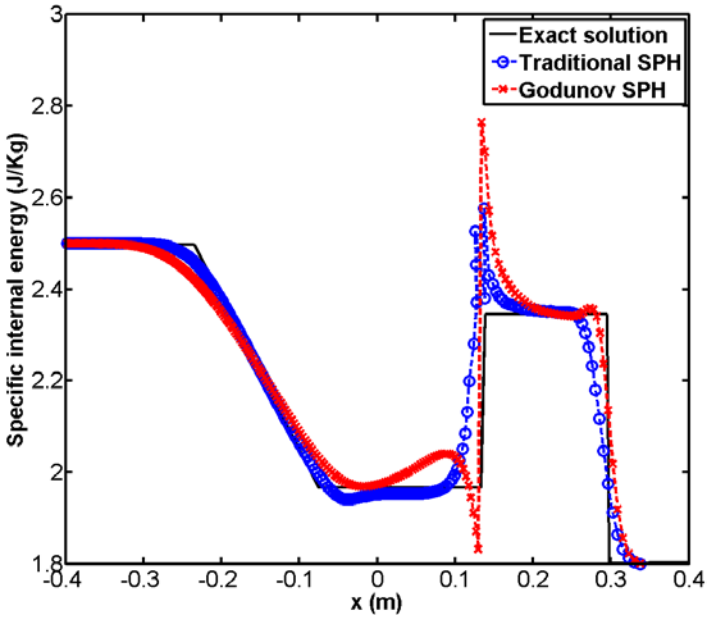

(d) Comparison of specific internal energy calculated by traditional SPH with artificial viscosity, Godunov SPH with exact solution

Figure 8.2 One-dimensional shock tube problem. Comparison of properties calculated by traditional SPH with artificial viscosity, Godunov SPH with exact solution

It can be seen from Figure 8.2(a), (b) that there is violent fluctuation at the discontinuity when using traditional SPH. Even artificial viscosity cannot thoroughly eliminate the phenomenon. However, when using Godunov scheme, the fluctuation is obviously smoothed. It indicates that Godunov scheme can effectively eliminate fluctuation at discontinuity while maintaining the accuracy of traditional SPH. Another advantage of Godunov SPH is that the time-consuming process of searching for appropriate values for artificial viscosity is no longer needed.

8.5 Detonation of a 1D PBX 9501 bar

The following experiment [24] is studied using SPH simulations:

A 100 mm diameter, 12.5 mm thick aluminum flyer plate impacts a target consisting of: a 90 mm diameter, 6 mm thick aluminum plate, a 90 mm diameter, 20 mm thick PBX 9501 charge, and a 90 mm diameter, 6 mm thick aluminum back plate. Pressure gauges are embedded in the explosive to record the variation of pressure during detonation.

8.5.1 Case 1

The simplified one-dimensional PBX 9501 model is 0.02 m long, as shown in Figure 7.9. On the left there is a rigid wall, the explosive bar impacts the rigid wall at certain velocity. Particles are uniformly distributed and smoothing length of each particle is set to be 1.5 times the distance between two adjacent

particles. The model consists of 4000 particles. The distribution of pressure along the explosive bar at $0.01\mu s$ is shown in Figure 8.3.

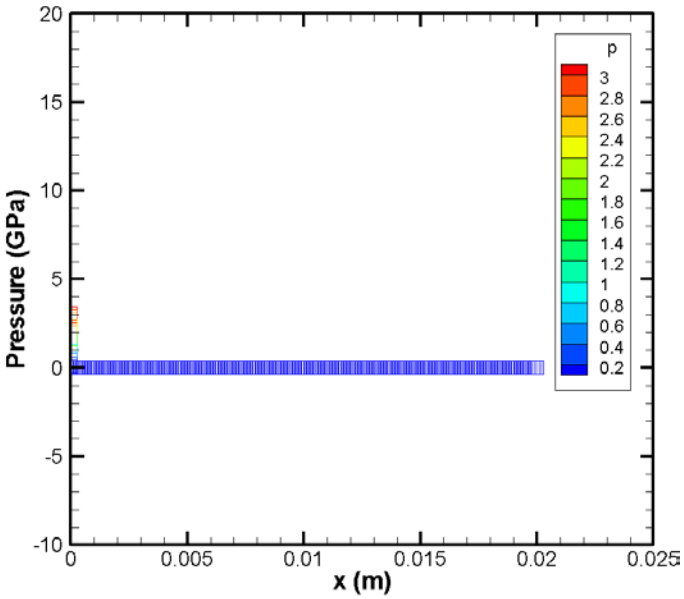

Figure 8.3 Distribution of pressure at $0.01\mu s$

The parameters of JWL EoS of solid PBX 9501 are listed in Table 6.1. The parameters of JWL EoS of gases products of PBX 9501 are listed in Table 6.2. The parameters of reaction rate are listed in Table 7.1.

The v_x is set to be 480 m/s. The variation of shock wave along the explosive bar with time obtained from Godunov SPH is shown in Figure 8.4, where each curve represents the profile of pressure on the explosive bar at a specific time:

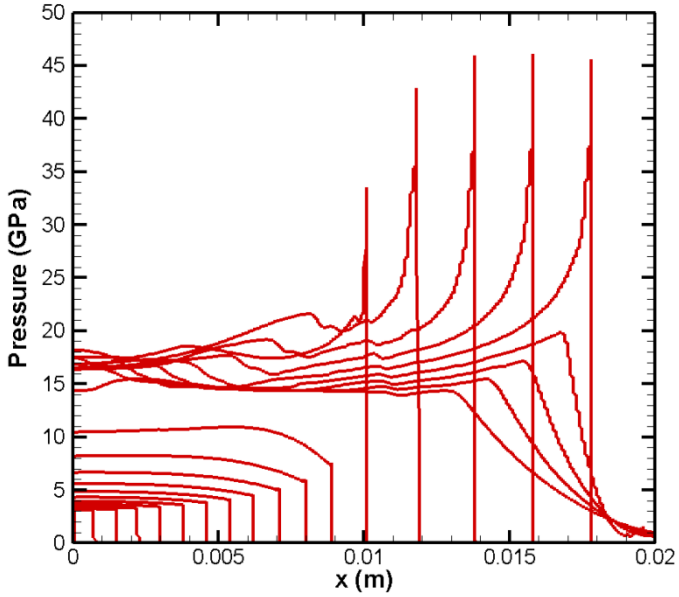

Figure 8.4 Calculated variation of shock wave along the explosive bar with time by Godunov SPH. v_x is set to be 480 m/s. Ambient temperature is 25 ℃.

It can be clearly seen from Figure 8.4 that the shock wave builds up while propagating from left to the right. When shock wave arrives at around 0.011 m, explosive bar is detonated and the shock wave transforms to self-sustained detonation wave. The detonation wave stabilizes at around 0.013 m. According to experiment [24], the experimental run-to-detonation distance is 11 mm, which agrees very well with simulation.

The profile of reaction and density of the one-dimensional PBX 9501 bar at 3.5 μs is shown in Figure 8.5.

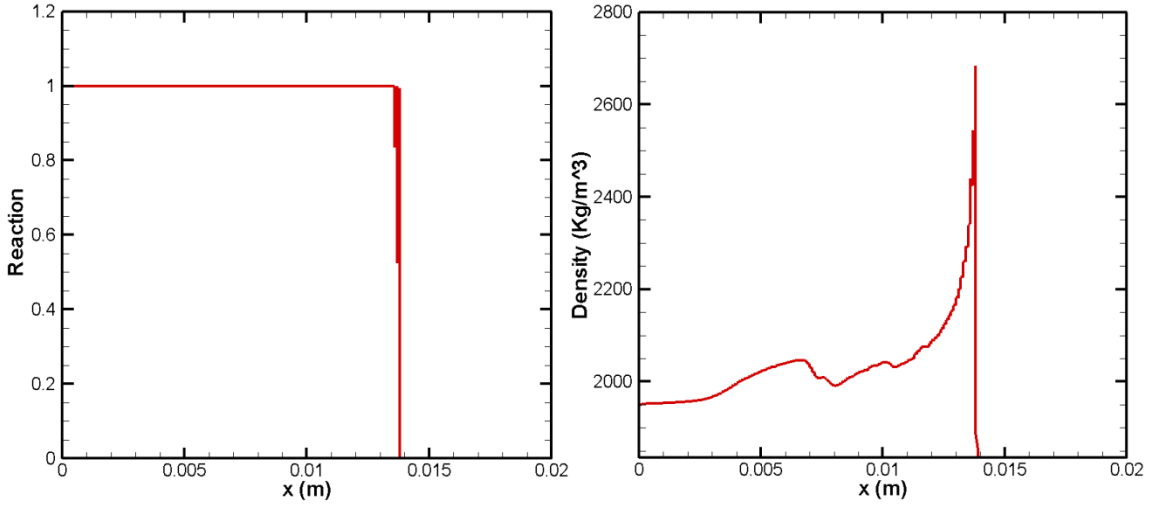

(a) Reaction (b) Density

Figure 8.5 Profile of reaction and density along the one-dimensional PBX 9501 bar at 3.5 μs

The comparison of pressure history calculated by traditional SPH, Godunov SPH, FVM [24] with experiment [24] is shown in Figure 8.6.

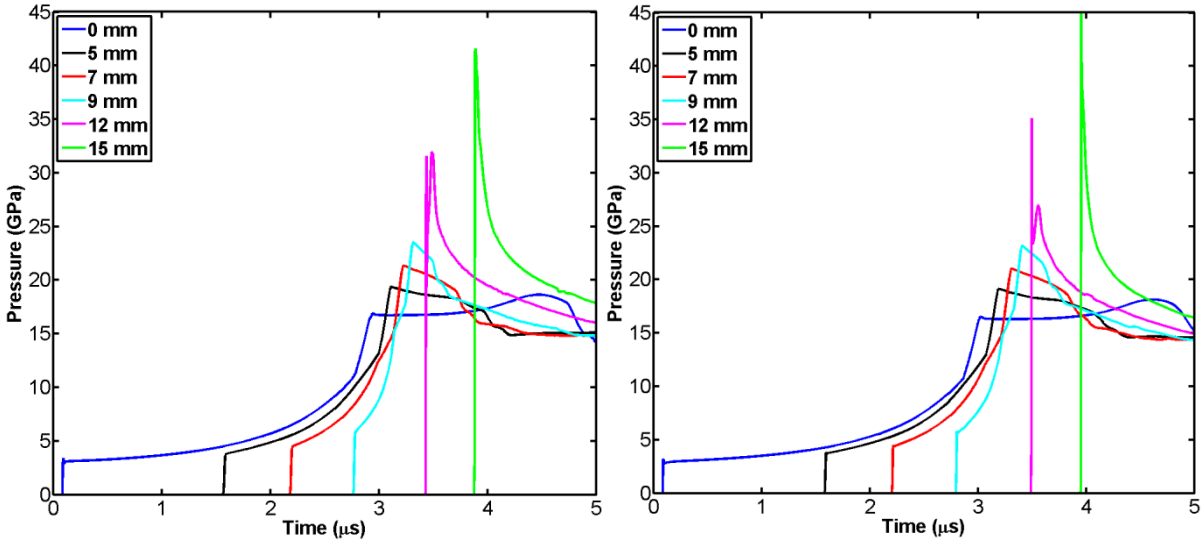

(a) Traditional SPH (b) Godunov SPH

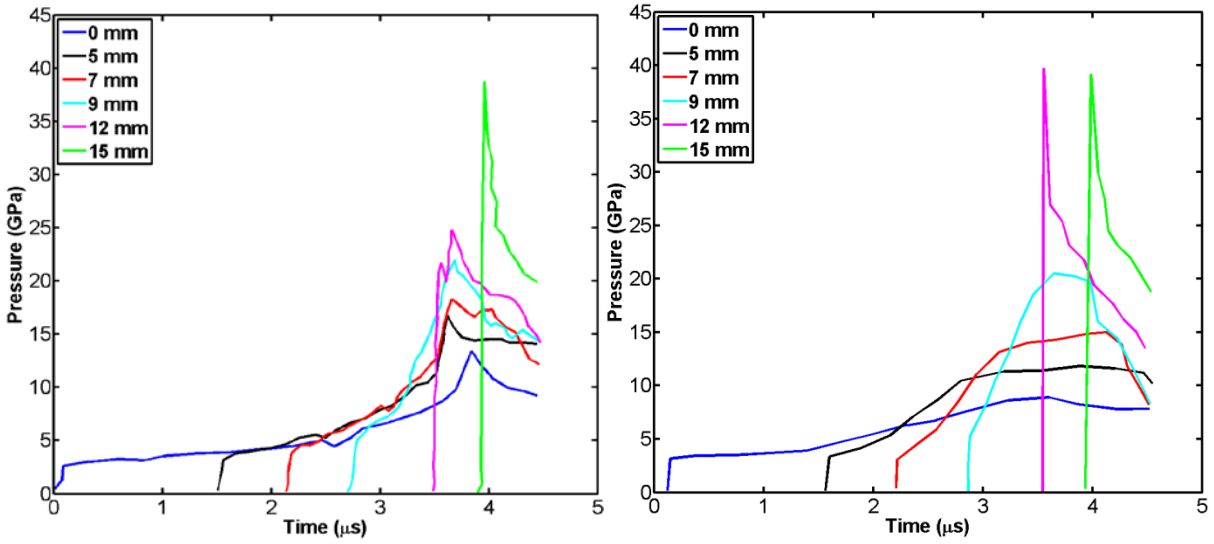

(c) FVM (d) Experiment

Figure 8.6 Case 1. Comparison of pressure history calculated by traditional SPH, Godunov SPH, FVM with experiment. Ambient temperature is 25 ℃. v_x is set to be 480 m/s.

According to Figure 8.6(a), (b), the calculated pressure histories using traditional SPH and Godunov SPH are very similar. Meanwhile, the curves calculated by both SPH methods are much smoother than those calculated by FVM. It is because SPH is Lagrangian method, which means that it is easier to track the interface of materials. The peak pressure calculated by both traditional SPH and Godunov SPH are very close to 40 GPa, which agrees well with experiment in Figure 8.6(d). In addition, it can be seen from Figure 8.6(a), (b) that the run-to-detonation time is around 3.5 μs , which is very close to experiment (3.4 μs). It also should be noted that the results calculated by traditional SPH and Godunov SPH are kind of different from experiment, which are probably because: firstly, the boundary condition of SPH simulations is simplified to rigid wall, which is different from experimental configuration; secondly, the SPH model is one-dimension, which is different from experiment; thirdly, though ignition and growth model is significantly improved compared with JWL++ model and JWL model, it cannot present all the details of detonation.

The calculated history of particle velocity is shown as below

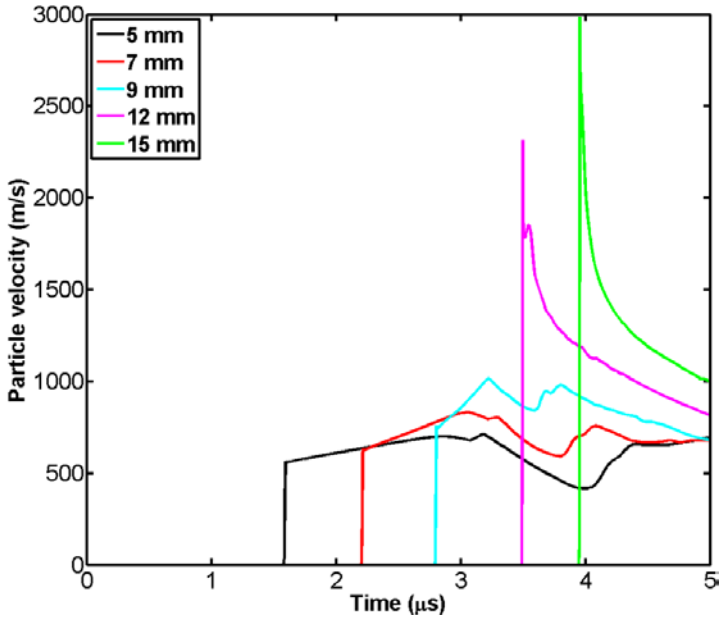

Figure 8.7 History of particle velocity calculated by Godunov SPH

It should be noted that in Figure 8.7 the benchmark of particle velocity is set to be 0.

8.5.2 Case 2

In case 2, all configurations remain unchanged except that v_x is set to be 432 m/s. The variation of shock wave along the explosive bar with time obtained from Godunov SPH is shown in Figure 8.8.

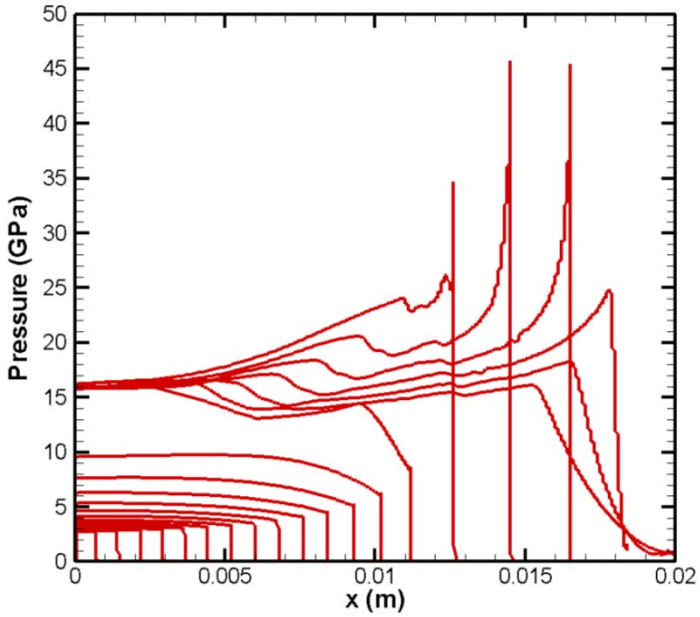

Figure 8.8 The variation of shock wave along the explosive bar with time obtained from Godunov SPH. v_x is set to be 432 m/s. Ambient temperature is 50 ℃.

It can be seen in Figure 8.8 that due to the decrease of impact velocity, the shock wave travels longer (at around 0.013 m) before transforming to detonation wave. According to experiment, the run-to-detonation distance is 0.013 m. The simulation agrees very well with experiment.

The comparison of pressure history calculated by traditional SPH, Godunov SPH, FVM [24] with experiment [24] is shown in Figure 8.9.

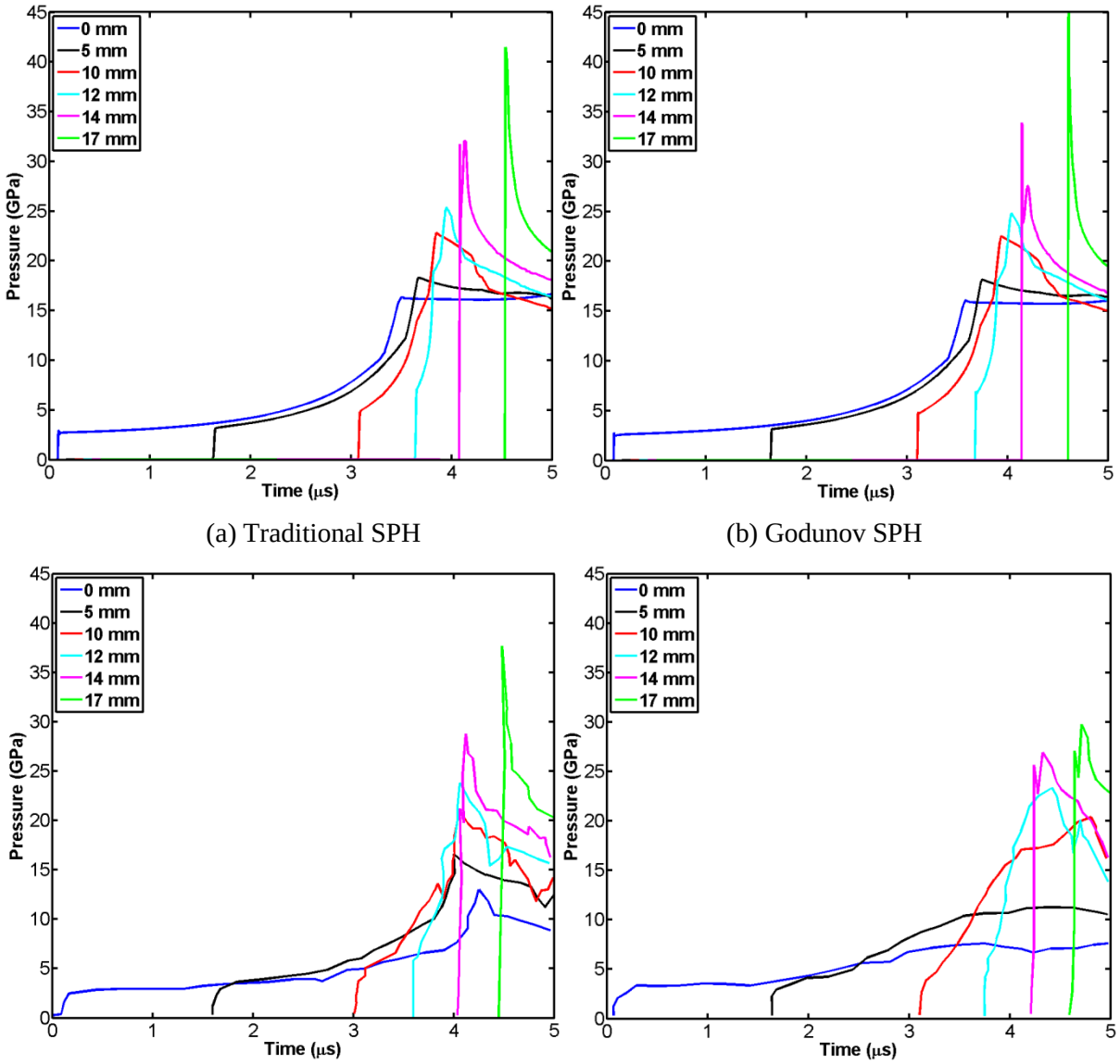

(a) Traditional SPH (b) Godunov SPH

(c) FVM (d) Experiment

Figure 8.9 Case 2. Comparison of pressure history calculated by traditional SPH, Godunov SPH, FVM with experiment. Ambient temperature is 50 ℃. v_x is set to be 432 m/s.

It can be seen from Figure 8.9(b), (d) that the pressure histories calculated by Godunov SPH are quite close to experiment in some ways, such as arrival time of shock wave and certain details. According to

Figure 8.9(b), the calculated run-to-detonation time is around 4.3 μs, which agrees well with experiment (4.3 μs).

The calculated history of particle velocity is shown as below

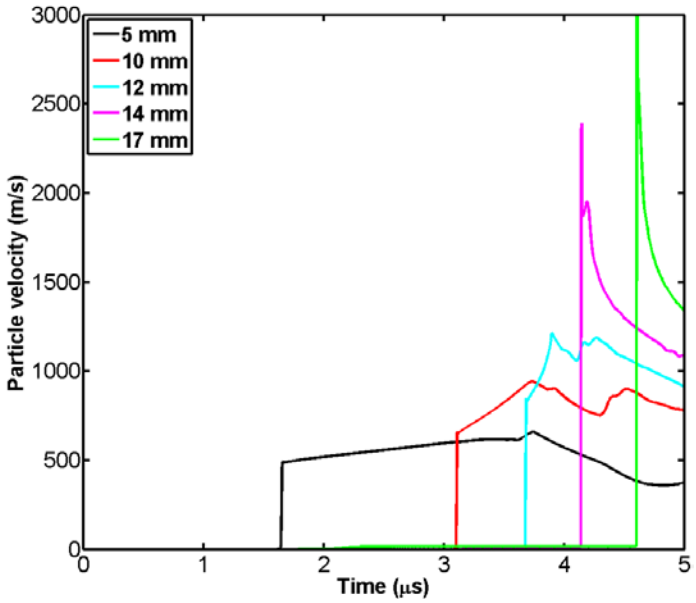

Figure 8.10 Calculated history of particle velocity calculated by Godunov SPH

8.5.3 Case 3

The configurations are similar to case 1 and case 2 except that the v_x is set to be 540 m/s. The calculated variation of shock wave along the explosive bar with time by Godunov SPH is shown in Figure 8.11.

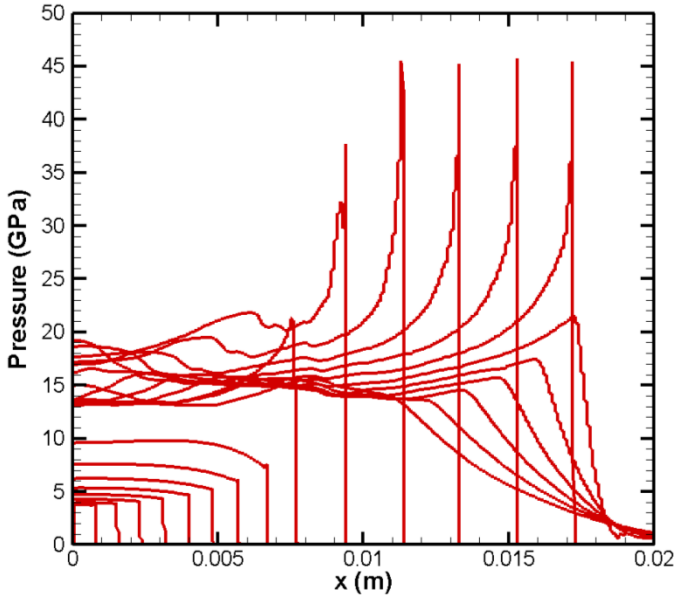

Figure 8.11 The variation of shock wave along the explosive bar with time obtained from Godunov SPH. v_x is set to be 540 m/s. Ambient temperature is 50 ℃.

It can be seen from Figure 8.11 that as impact velocity increases, the shock wave travels shorter before transforming to detonation wave. The calculated run-to-detonation distance is around 0.009 m, which is very close to experiment (0.008 m).

The comparison of pressure history calculated by traditional SPH, Godunov SPH, FVM [24] with experiment [24] is shown in Figure 8.12.

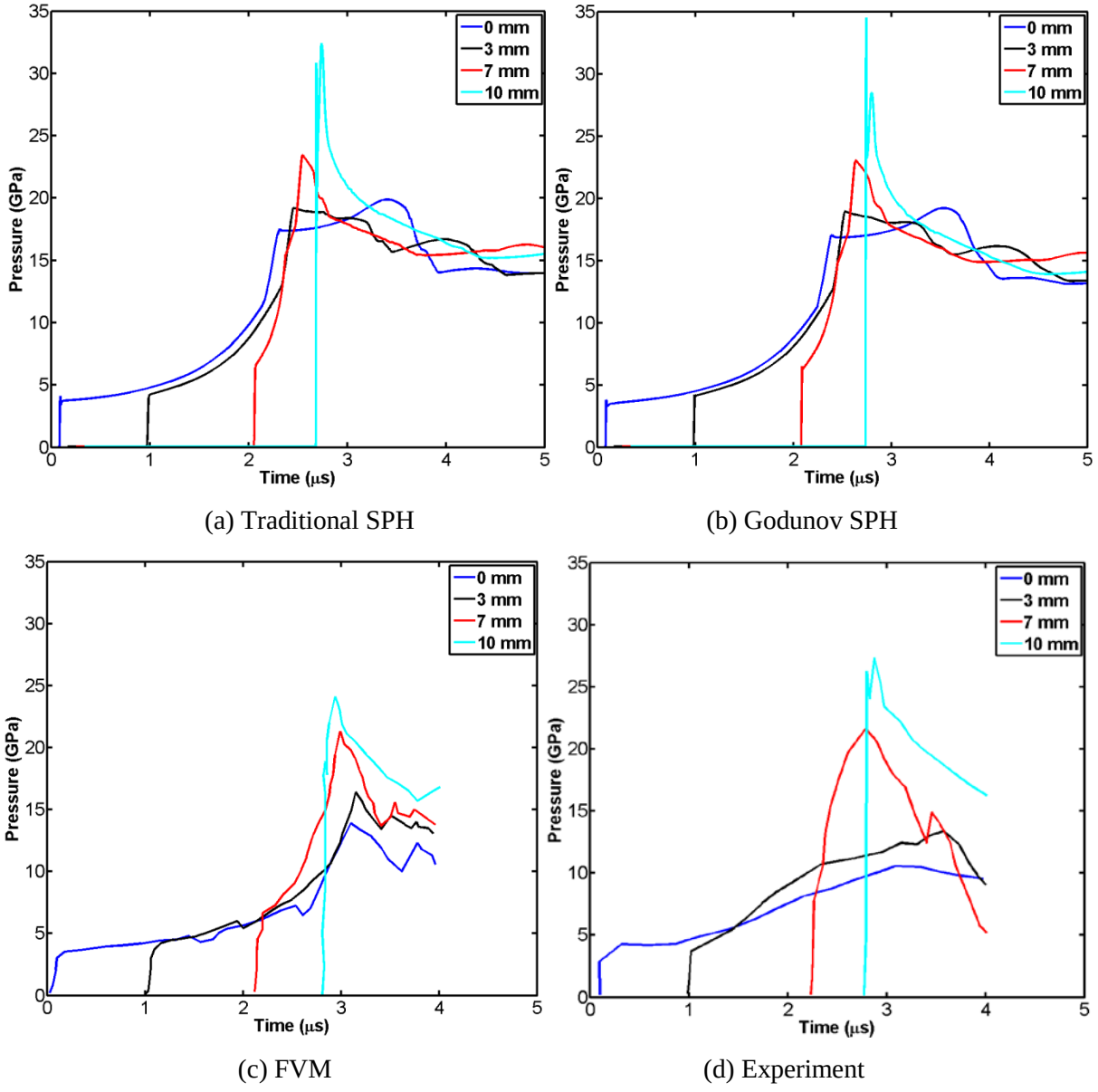

(a) Traditional SPH (b) Godunov SPH

(c) FVM (d) Experiment

Figure 8.12 Case 3. Comparison of pressure history calculated by traditional SPH, Godunov SPH, FVM with experiment. Ambient temperature is 50 ℃.v_x is set to be 540 m/s.

It can be seen from Figure 8.12(b) that the calculated peak pressure of gauge located at 10 mm is around 24 GPa, which is quite close to peak pressure recorded in experiment (around 27 GPa). According to Figure 8.12(b), the calculated run-to-detonation time is around 2.5 μs, which is close to experiment (2.4 μs).

The calculated history of particle velocity is shown as below

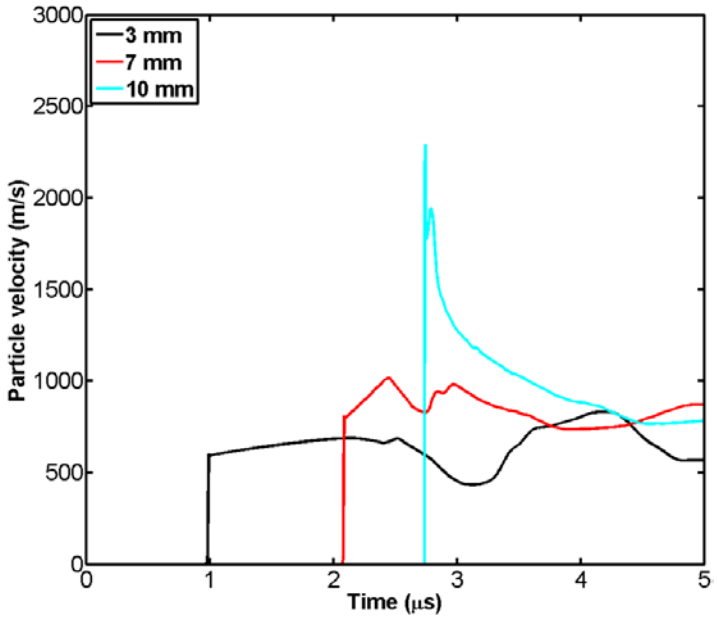

Figure 8.13 History of particle velocity calculated by Godunov SPH

8.6 2D simulation of PBX 9501 using Godunov SPH

A two-dimensional model of PBX 9501 bar is developed to investigate the stability and accuracy of the Godunov scheme. The parameters of ignition and growth model are the same as those mentioned in previous section. The model is 0.3 m in length, 0.0127 m in radius. Smoothing length is set to be 1.5 times the distance between two neighboring particles. The v_x of leftmost particles are set to be 2000 m/s to detonate the explosive bar, as shown below

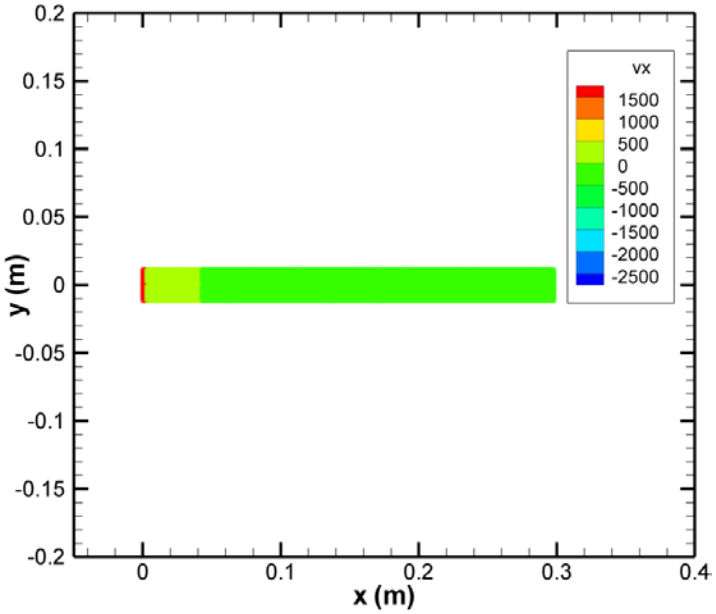

Figure 8.14 Profile of two-dimensional SPH model

The comparison of profiles calculated by traditional SPH (left) and Godunov SPH (right) at different time is shown in Figure 8.15.

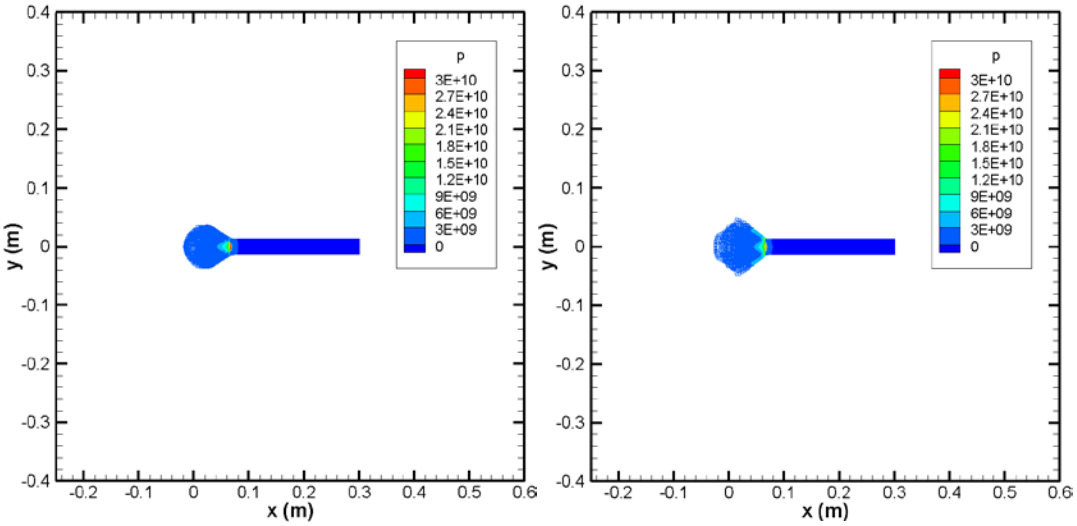

(a) Comparison of profiles calculated by traditional SPH (left) and Godunov SPH (right) at 10 μs

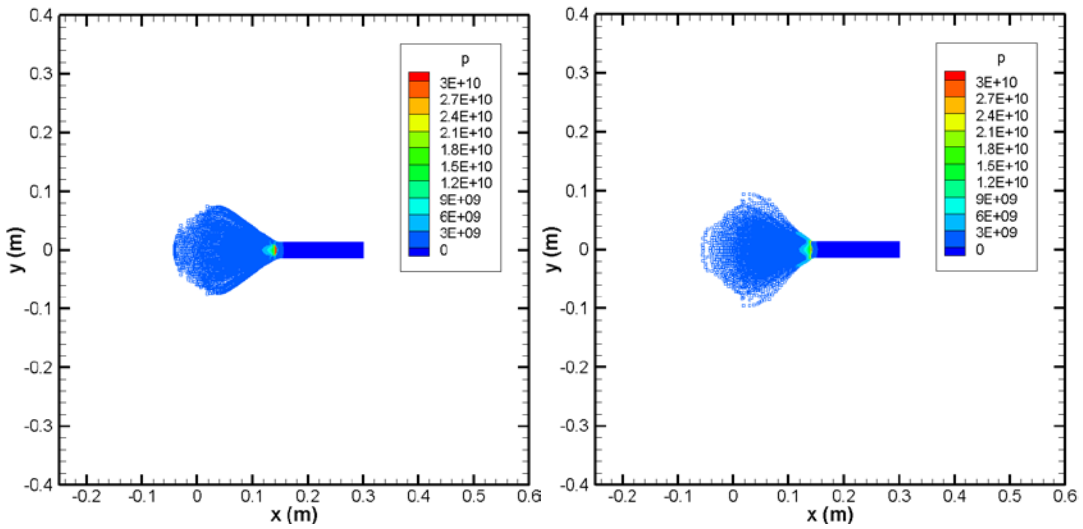

(b) Comparison of profiles calculated by traditional SPH (left) and Godunov SPH (right) at 20 μs

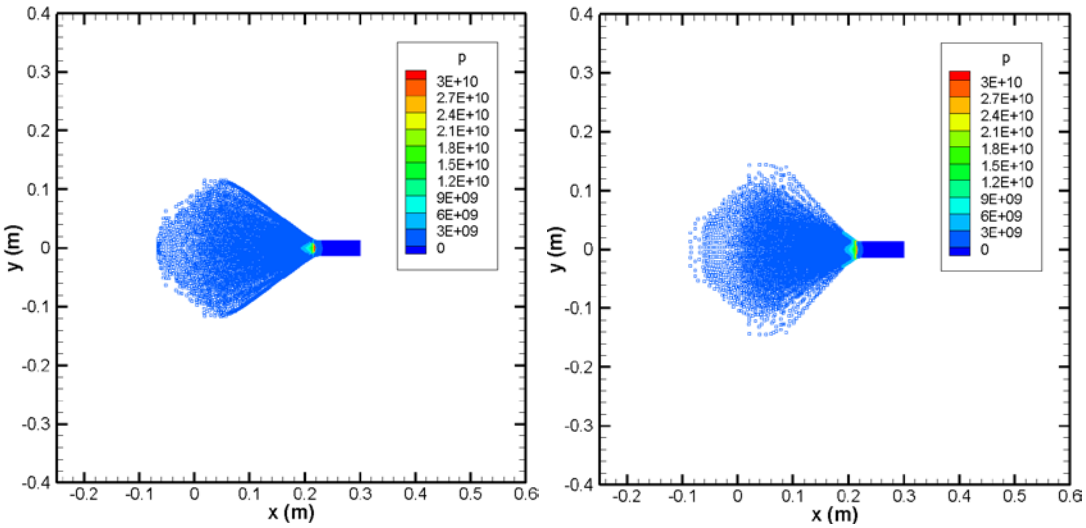

(c) Comparison of profiles calculated by traditional SPH (left) and Godunov SPH (right) at 30 μs

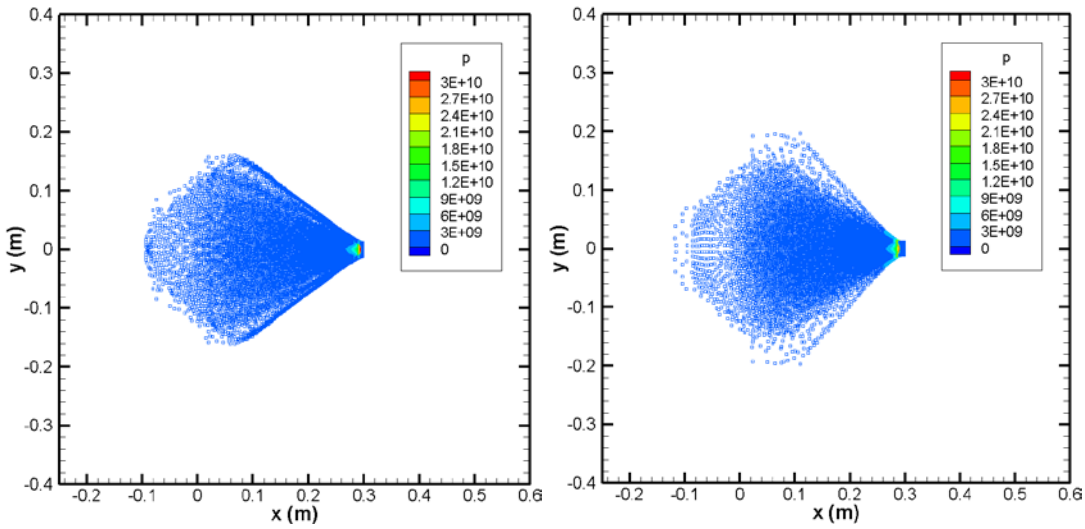

(d) Comparison of profiles calculated by traditional SPH (left) and Godunov SPH (right) at 40 μs

Figure 8.15 Comparison of profiles calculated by traditional SPH and Godunov SPH at different time

The comparison of reaction, v_x and density calculated by traditional SPH and Godunov SPH at 40 μs is shown in Figure 8.16.

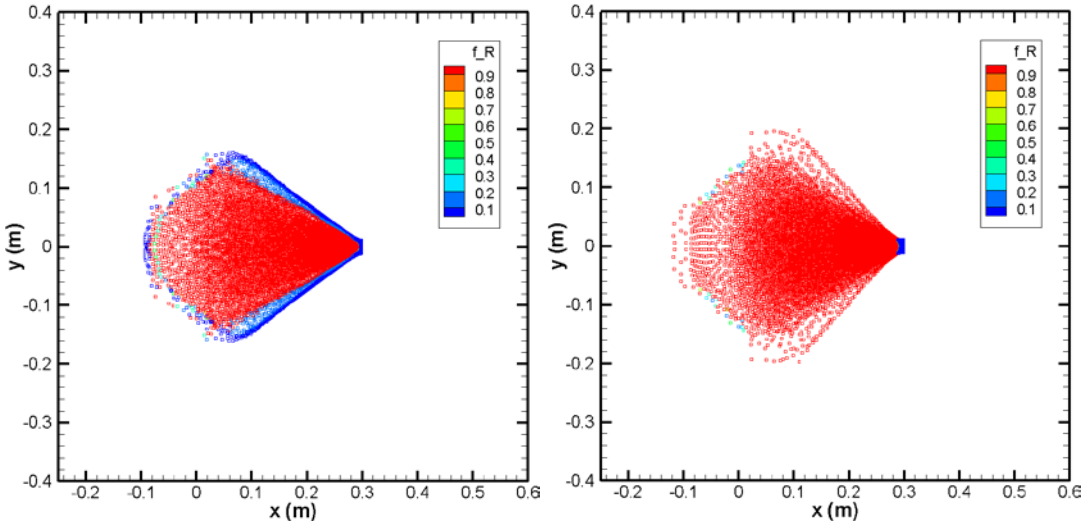

(a) Comparison of reaction calculated by traditional SPH (left) and Godunov SPH (right) at 40 μs

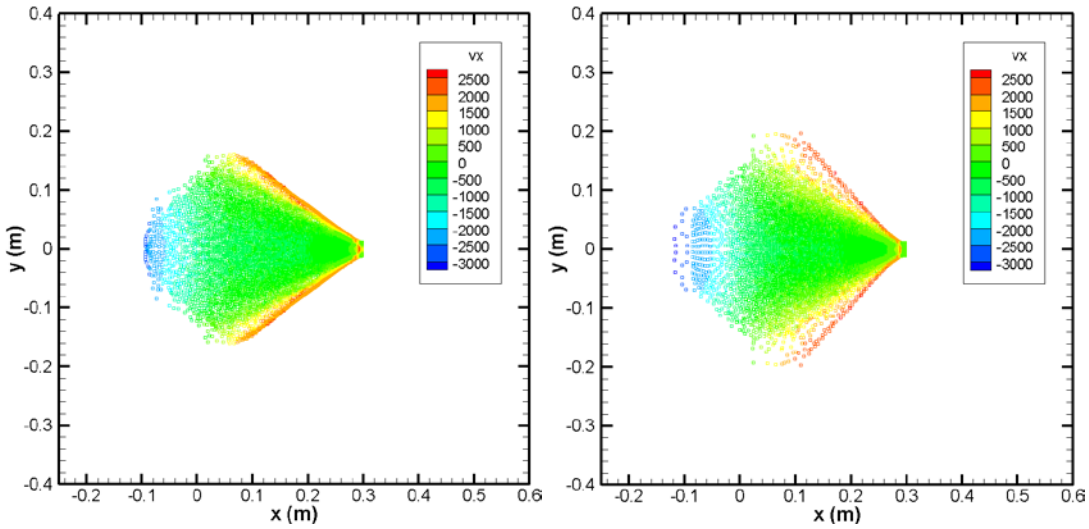

(c) Comparison of v_x calculated by traditional SPH (left) and Godunov SPH (right) at 40 μs

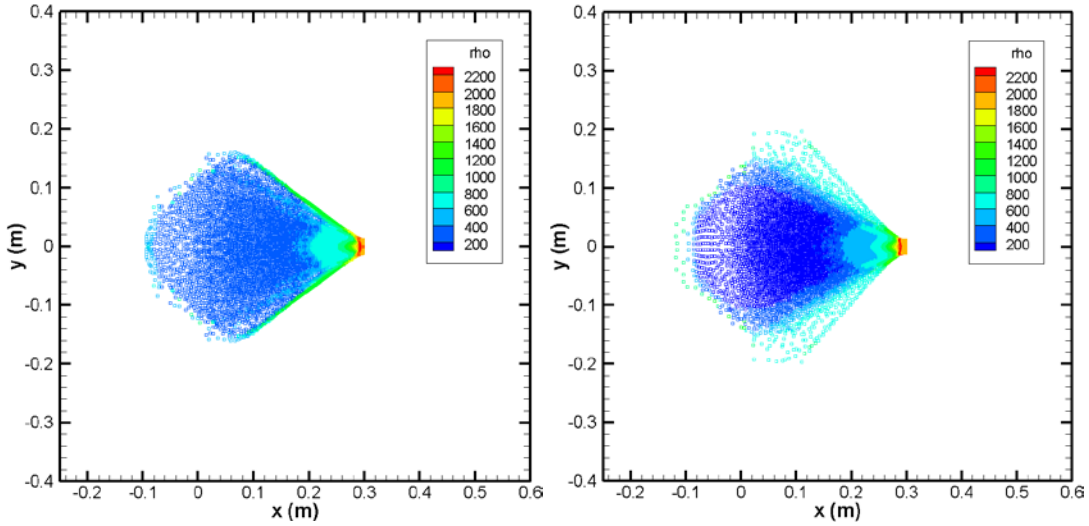

(c) Comparison of ρ calculated by traditional SPH (left) and Godunov SPH (right) at 40 μs

Figure 8.16 Comparison of reaction, v_x and density calculated by traditional SPH and Godunov SPH at 40 μs

Conclusion

Equation of state (EoS) plays a fundamental role in numerical modeling of high explosives based on hydrodynamic formulations. Traditionally, the EoS of explosives can only be obtained through experiments, which is not only costly and time-consuming, but also hazardous. This report presents a method to calculate the EoS of solid β−HMX and its gaseous products using a series of molecular dynamics (MD) simulations. The reactive force fields ReaxFF-d3 used in these MD simulations are obtained through quantum mechanics (QM) simulations. A QM-MD-SPH method has been successfully developed, coded and tested using a number of benchmark problems and experimental results for various types of high explosives.

The geometric structure of β−HMX is obtained from DFT-D2 study. It is found that the calculated lattice constants of β−HMX agree well with experiments. In addition, the mechanical properties, EoSs of Aluminum and its oxide are also studied through a series of first-principle MQ simulations. The stability, mechanical properties and EoSs of iron are obtained from the first principle.

The calculated EoSs are incorporated in our in-house QM-MD-SPH codes. The simulation using fitted EoSs is compared with experimental results (from the open literature), and results obtained by the other numerical methods. It is found that the QM-MD-SPH using the fitted EoSs from MD simulation results can well predict arrival time of shock waves and the peak pressure in many cases. However, due to the complexity of detonation problems, all numerical models can not accurately predict detailed pressure histories, though they can roughly predict the build-up process. Other reasons for the error may include 1) simplified boundary conditions and settings in the numerical model, which may be quite different from the experimental setup; 2) the purity of the materials may also contributes to the errors; 3) experimental error.

In addition, the influence of shear viscosity α, bulk viscosity β, and number of particles on simulation in QM-MD-SPH is analyzed, through the simulation of the explosion of one-dimensional PBX 9501 bar model ignited by impact. It is found that with the increase of α, the fluctuation at peak pressure is significantly reduced, and 3 is a reasonable choice for simulations. It is also found that bulk viscosity β has much less influence in reducing fluctuation at peak pressure. Both α and β do not have obvious influence on arrival time of shock waves. Moreover, when number of particles increases, the calculated curves becomes smoother and more details of the explosion events can be revealed. This is, of course, at the expenses of the computational resources. For the proposed one-dimensional PBX 9501 model, 4000 particles ($0.02\ m$) is a reasonable choice high explosives we have studied (on a normal PC without parallelization). For the high resolution solutions of 2D and 3D problems, more powerful computer with parallelization capabilities is needed.

In the study of aluminized explosives, an afterburning model is integrated with ignition and growth model and implemented in our SPH code for simulating the explosion of the aluminized explosive HMX-Al with various Al mass fractions. It is found that in the near field, with the increase of mass fraction of aluminum powder, the peak pressure is reduced. This is because the burning of Al is much slower compared with the detonation of the explosives. Therefore, at the early stage, the aluminum powder plays only a role of diluting the explosion power. In the far field, however, the pressure is strengthened. This is because the burning of the aluminum powder adds on the explosion power at the later time.

A Godunov SPH method is incorporated into our method, using the ignition and growth model. Godunov approach eliminates the need of using the artificial viscosity in traditional SPH to reduce the oscillations near the shock front. To validate the Godunov scheme, a one-dimensional shock tube problem is investigated using both traditional SPH with artificial viscosity and Godunov SPH. It is found that Godunov SPH can effectively reduce unphysical fluctuation, without the use of artificial viscosity. It is recommended for the simulation of high explosives where shocks always exist.

The Godunov SPH is also applied to investigate the detonation of a one-dimensional PBX 9501 bar. We found that the Godunov SPH performs better than traditional SPH with better accuracy. In addition, due to its advantage in describing interfaces of materials, the calculated pressure histories by Godunov SPH are smoother. Further, a two-dimensional model of PBX 9501 bar is developed to examine the accuracy of Godunov SPH with respect to traditional SPH. It is found that some unphysical behavior (observed on the outer particles of the two-dimensional SPH model) in the traditional SPH simulation is removed when using Godunov approach. Overall, Godunov SPH is a promising method compared with traditional SPH. The proposed Godunov SPH method can be extended to study other similar explosives.

Reference

[1] H G Gallagher, J N Sherwood, R M Vrcelj. "Growth and dislocation studies of β-HMX." Chemistry Central Journal 8.1 (2014): 75.

[2] P W Cooper. Explosives engineering. New York: VCH, 1996.

[3] E L Lee, and C M Tarver. "Phenomenological model of shock initiation in heterogeneous explosives." Physics of Fluids (1958-1988) 23.12 (1980): 2362-2372.

[4] C M Tarver. "Ignition and Growth Modeling of LX-17 Hockey Puck Experiments." Propellants, Explosives, Pyrotechnics 30.2 (2005): 109-117.

[5] P C Souers, L C Haselman Jr. Detonation equation of state at LLNL, 1993. No. UCRL-ID--116113. Lawrence Livermore National Lab., CA (United States), 1994.

[6] P C Souers, S Anderson, J Mercer, et al. (2000). JWL++: a simple reactive flow code package for detonation. Propellants, Explosives, Pyrotechnics, 25(2), 54-58.

[7] P C Souers, R Garza, P Vitello. (2002). Ignition & growth and JWL++ detonation models in coarse zones. Propellants, Explosives, Pyrotechnics, 27(2), 62-71.

[8] J M Walsh, R H Christian. Equation of state of metals from shock wave measurements. Phys Rev. 97, 1955:1544.

[9] R G McQueen, S P Marsh. Equation of State for Nineteen Metallic Elements from Shock-Wave Measurements to Two Megabars. Journal of Applied Physics 31.7 (1960): 1253-1269.

[10] R G McQueen, S P Marsh, J W Taylor, et al. The equation of state of solids from shock wave studies. High velocity impact phenomena 293 (1970).

[11] A C Mitchell,W J Nellis. Equation of state and electrical conductivity of water and ammonia shocked to the 100 GPa (1 Mbar) pressure range. The Journal of Chemical Physics 76.12 (1982): 6273-6281.

[12] E N Avrorin, B K Vodolaga, N P Voloshin, et al. Experimental confirmation of shell effects on the shock adiabats of aluminum and lead. JETP Lett.(USSR) 43.5 (1986): 308-311.

[13] L B Da Silva, P Celliers, G W Collins, et al. Absolute equation of state measurements on shocked liquid deuterium up to 200 GPa (2 Mbar). Physical review letters 78.3 (1997): 483.

[14] N L Coleburn, T P Liddiard Jr. Hugoniot equations of state of several unreacted explosives. The Journal of Chemical Physics 44.5 (1966): 1929-1936.

[15] J J Dick, C A Forest. The Hugoniot and shock sensitivity of a plastic-bonded TATB explosive PBX 9502. Journal of applied physics 63.10 (1988): 4881-4888.

[16] C S Yoo, H Cynn. Equation of state, phase transition, decomposition of β-HMX (octahydro-1, 3, 5, 7-tetranitro-1, 3, 5, 7-tetrazocine) at high pressures." The Journal of Chemical Physics 111.22 (1999): 10229-10235.

[17] L L Davis, L G Hill. ANFO cylinder tests. Shock Compression of Condensed Matter. AIP Conference Proceedings No.1. IOP Institute of Physics Publishing LTD, 2002.

[18] Adri CT van Duin, S Dasgupta, F Lorant, et al. ReaxFF: a reactive force field for hydrocarbons. The Journal of Physical Chemistry A 105.41 (2001): 9396-9409.

[19] L Liu, Y Liu, S V Zybin, et al. ReaxFF-lg: Correction of the ReaxFF reactive force field for London dispersion, with applications to the equations of state for energetic materials. The Journal of Physical Chemistry A 115.40 (2011): 11016-11022.

[20] A Strachan, E M Kober, A C van Duin, et al. Thermal decomposition of RDX from reactive molecular dynamics. J. Chem. Phys. 2005, 122, 054502.

[21] K Chenoweth, S Cheung, ACT Du Van, et al. "Simulations on the thermal decomposition of a poly (dimethylsiloxane) polymer using the ReaxFF reactive force field." Journal Of The American Chemical Society 127.19 (2005): 7192-7202.

[22] L Zhang, S V Zybin, ACT V Duin, et al. Thermal decomposition of energetic materials by ReaxFF reactive molecular dynamics. (2006): 589-592.

[23] Q Peng, Rahul, G Wang, G R Liu, and S De, "Structures, Mechanical Properties, Equations of State, and Electronic Properties of β-HMX under Hydrostatic Pressures: A DFT-D2 study", Physical Chemistry Chemical Physics, (2014), 16, 19972—19983.

[24] C M Tarver, J W Forbes, F Garcia, et al. Manganin Gauge and Reactive Flow Modeling Study of the Shock Initiation of PBX 9501. 12th American Physical Society Topical Conference, Atlanta, GA. 2001.

[25] M A Cook, A S Filler, R T Keyes, et al. "Aluminized explosives." The Journal of Physical Chemistry 61.2 (1957): 189-196.

[26] P W Cooper, S R Kurowski. Introduction to the Technology of Explosives. New York: VCH, 1996.

[27] M L Wilkins, B Squier, B Halperin. Equation of state for detonation products of PBX 9404 and LX04-01. Symposium (International) on Combustion. Vol. 10. No. 1. Elsevier, 1965.

[28] J Wackerle, R L Rabie, M J Ginsberg, et al. A shock initiaison study of PBX-9404. Shock 1.2 (1978): 5.

[29] V M Boiko, S V Poplavski. "Self-ignition and ignition of aluminum powders in shock waves." Shock Waves 11.4 (2002): 289-295.

[30] A L Kuhl, M Howard, L Fried. 34th International ICT Conference: Energetic Materials: Reactions of Propellants, Explosives and Pyrotechnics, Karlsruhe, Germany, 2003.

[31] A. L. Kuhl, J. B. Bell and V. E. Beckner, Heterogeneous Continuum Model of Aluminum Particle Combustion in Explosions, Combustion, Explosion and Shock Waves 46(4) (2010), pp. 433–448.

[32] A. L. Kuhl, J. B. Bell and V. E. Beckner, Gasdynamic Model of Turbulent Combustion in TNT Explosions, 33rd International Combustion Symposium, Beijing, China, August 1–6 (2010).

[33] F Togashi, J D Baum, E Mestreau, et al. "Numerical simulation of long-duration blast wave evolution in confined facilities." Shock Waves 20.5 (2010): 409-424.

[34] F Togashi, J D Baum, O A Soto, et al. Numerical Simulation of TNT-Al Explosives in Explosion Chamber. 7th International Conference on Computational Fluid Dynamics, Big Island, Hawaii. 2012

[35] Z Q Zhou, J X Nie, X Y Guo, et al. "A New Method for Determining the Equation of State of Aluminized Explosive." Chinese Physics Letters 32.1 (2015): 016401.

[36] R A Gingold, J J Monaghan. Smoothed particle hydrodynamics-theory and application to non-spherical stars. Mon. Not. R. Astron. Soc. 1977;181:375-389.

[37] L B Lucy. A numerical approach to the testing of the fission hypothesis. The Astronomical Journal. 1977;82:1013-1024.

[38] G R Liu, M B Liu. Smoothed particle hydrodynamics: a meshfree particle method. Singapore: World Scientific; 2003.

[39] M B Liu, G R Liu, Z Zong, K Y Lam. Computer simulation of high explosive explosion using smoothed particle hydrodynamics methodology. Computers & Fluids.2003. 32(3):305-322.

[40] M B Liu, G R Liu, K Y Lam, Z Zong. Smoothed particle hydrodynamics for numerical simulation of underwater explosion. Computational Mechanics. 2003. 30(2):106-118.

[41] M B Liu, G R Liu, K Y Lam, Z Zong. Meshfree particle simulation of the detonation process for high explosives in shaped charge unlined cavity configurations. Shock Waves.2003. 12(6):509-520.

[42] A.K Sikder and Nirmala Sikder. A review of advanced high performance, insensitive and thermally stable energetic materials emerging for military and space applications. J. Hazard. Mater., 112(1-2):1–15, 2004.

[43] D.M. Badgujar, M.B. Talawar, S.N. Asthana, and P.P. Mahulikar. Advances in science and technology of modern energetic materials: An overview. J. Hazard. Mater., 151(2-3):289–305, 2008.

[44] Betsy M. Rice, Jennifer J. Hare, and Edward F. C. Byrd. Accurate predictions of crystal densities using quantum mechanical molecular volumes. J. Phys. Chem. A, 111(42):10874–10879, 2007.

[45] A. C. Landerville, M. W. Conroy, M. M. Budzevich, Y. Lin, C. T. White, and I. I. Oleynik. Equations of state for energetic materials from density functional theory with van der Waals, thermal, and zero-point energy corrections. Appl. Phys. Lett., 97(25):251908, DEC 20 2010.

[46] H. J. Song and F. Huang. Accurately predicting the structure, density, and hydrostatic compression of crystalline beta-1,3,5,7-tetranitro-1,3,5,7-tetraazacyclooctane based on its wave-function-based potential. Europhys. Lett., 95(5):53001, SEP 2011.

[47] E. F. C. Byrd, G. E. Scuseria, and C. F. Chabalowski. An ab initio study of solid nitromethane, HMX, RDX, and CL20: Successes and failures of DFT. J. Phys. Chem. B, 108(35):13100–13106, SEP 2 2004.

[48] Edward F. C. Byrd and Betsy M. Rice. Ab initio study of compressed 1,3,5,7-tetranitro-1,3,5,7-tetraazacyclooctane (HMX), cyclotrimethylenetrinitramine (RDX), 2,4,6,8,10,12-hexanitrohexaazaisowurzitane (CL-20), 2,4,6-trinitro-1,3,5-benzenetriamine (TATB), and pentaerythritol tetranitrate (PETN). J. Phys. Chem. C, 111(6):2787–2796, FEB 15 2007.

[49] M. W. Conroy, I. I. Oleynik, S. V. Zybin, and C. T. White. First-principles anisotropic constitutive relationships in beta-cyclotetramethylene tetranitramine (beta-HMX). J. Appl. Phys., 104(5):053506, SEP 1 2008.

[50] Jeffrey R. Deschamps, Mark Frisch, and Damon Parrish. Thermal Expansion of HMX. J. Chem. Crystallogr., 41(7):966–970, JUL 2011.

[51] Jiri Klimes and Angelos Michaelides. Perspective: Advances and challenges in treating van der waals dispersion forces in density functional theory. J. Chem. Phys., 137(12):120901, 2012.

[52] M. Dion, H. Rydberg, E. Schröder, D. C. Langreth, and B. I. Lundqvist. Van der waals density functional for general geometries. Phys. Rev. Lett., 92:246401, Jun 2004.

[53] Kyuho Lee, Éamonn D. Murray, Lingzhu Kong, Bengt I. Lundqvist, and David C. Langreth. Higher-accuracy van der waals density functional. Phys. Rev. B, 82:081101, Aug 2010.

[54] Ji říKlimeš, David R. Bowler, and Angelos Michaelides. Van der waals density functionals applied to solids. Phys. Rev. B, 83:195131, May 2011.

[55] S Grimme. Accurate description of van der Waals complexes by density functional theory including empirical corrections. J. Comput. Chem., 25(12):1463–1473, SEP 2004.

[56] Neumann, Marcus A. and Perrin, Marc-Antoine. Energy ranking of molecular crystals using density functional theory calculations and an empirical van der waals correction. J. Phys. Chem. B, 109(32):15531–15541, 2005.

[57] Stefan Grimme. Semiempirical GGA-type density functional constructed with a long-range dispersion correction. J. Comput. Chem., 27(15):1787–1799, NOV 30 2006.

[58] Marcel Swart, Miquel Sol, and F. Matthias Bickelhaupt. Inter- and intramolecular dispersion interactions. J. Comput. Chem., 32(6):1117–1127, 2011.

[59] Alexandre Tkatchenko and Matthias Scheffler. Accurate molecular van der waals interactions from ground-state electron density and free-atom reference data. Phys. Rev. Lett., 102:073005, Feb 2009.

[60] Stefan Grimme, Jens Antony, Stephan Ehrlich, and Helge Krieg. A consistent and accurate ab initio parametrization of density functional dispersion correction (dft-d) for the 94 elements h-pu. J. Chem. Phys., 132(15):154104, 2010.

[61] Lars Goerigk and Stefan Grimme. A thorough benchmark of density functional methods for general main group thermochemistry, kinetics, and noncovalent interactions. Phys. Chem. Chem. Phys., 13:6670–6688, 2011.

[62] Stefan Grimme, Stephan Ehrlich, and Lars Goerigk. Effect of the damping function in dispersion corrected density functional theory. J. Comput. Chem., 32(7):1456–1465, 2011.

[63] Alexandre Tkatchenko, Robert A. DiStasio, Roberto Car, and Matthias Scheffler. Accurate and efficient method for many-body van der waals interactions. Phys. Rev. Lett., 108:236402, Jun 2012.

[64] Tomá š Bučko, S. Lebègue, Jürgen Hafner, and J. G. Ángyán. Tkatchenko-scheffler van der waals correction method with and without self-consistent screening applied to solids. Phys. Rev. B, 87:064110, Feb 2013.

[65] M. W. Conroy, I. I. Oleynik, S. V. Zybin, and C. T. White. Density functional theory calculations of solid nitromethane under hydrostatic and uniaxial compressions with empirical van der waals correction. J. Phys. Chem. A, 113(15):3610–3614, 2009.

[66] G. Kresse and J. Hafner. Ab initio molecular dynamics for liquid metals. Phys. Rev. B, 47:558, 1993.

[67] G. Kresse and J. Furthuller. Efficiency of ab-initio total energy calculations for metals and semiconductors using a plane-wave basis set. Comput. Mater. Sci., 6:15, 1996.

[68] P. Hohenberg and W. Kohn. Inhomogeneous electron gas. Phys. Rev., 136(3B):B864, Nov 1964.

[69] W. Kohn and L. J. Sham. Self-consistent equations including exchange and correlation effects. Phys. Rev., 140(4A):A1133, Nov 1965.

[70] J. P. Perdew, K. Burke, and M. Ernzerhof. Generalized gradient approximation made simple. Phys. Rev. Lett., 77:3865, 1996.

[71] P. E. Blöchl. Projector augmented-wave method. Phys. Rev. B, 50(24):17953–17979, Dec 1994.

[72] R. O. Jones and O. Gunnarsson. The density functional formalism, its applications and prospects. Rev. Mod. Phys., 61(3):689–746, Jul 1989.

[73] C. S. Choi and H. P. Boutin. A study of crystal structure of beta-cyclotetramethylene tetranitramine by neutron diffraction. Acta Crystallogr., Sect. B: Struct. Sci., B 26:1235, 1970.

[74] M Herrmann, W Engel, and N Eisenreich. Thermal-analysis of the phases of hmx using x-ray diffraction. Zeitschrift Fur Kristallographie, 204(1):121–128, 1993.

[75] B. Sun, J. M. Winey, Y. M. Gupta, and D. E. Hooks. Determination of second-order elastic constants of cyclotetramethylene tetranitramine (-hmx) using impulsive stimulated thermal scattering. J. Appl. Phys., 106(5):053505, 2009.

[76] Zhongqing Wu, Rajiv K. Kalia, Aiichiro Nakano, and Priya Vashishta. Vibrational and thermodynamic properties of -hmx: A first-principles investigation. J. Chem. Phys., 134(20):204509, 2011.

[77] Lai-Yu Lu, Dong-Qing Wei, Xiang-Rong Chen, Dan Lian, Guang-Fu Ji, Qing-Ming Zhang, and Zi-Zheng Gong. The first principle studies of the structural and vibrational properties of solid beta-HMX under compression. Mol. Phys., 106(21):2569–2580, 2008.

[78] Weihua Zhu, Xiaowen Zhang, Tao Wei, and Heming Xiao. Dft studies of pressure effects on structural and vibrational properties of crystalline octahydro-1,3,5,7-tetranitro-1,3,5,7-tetrazocine. Theor. Chem. Acc., 124(3-4):179–186, 2009.

[79] Hong-Ling Cui, Guang-Fu Ji, Xiang-Rong Chen, Wei-Hua Zhu, Feng Zhao, Ya Wen, and Dong-Qing Wei. First Principles Study of High Pressure Behavior of Solid beta HMX. J. Phys. Chem. A, 114(2):1082–1092, 2010.

[80] T. D. Sewell. Monte carlo calculations of the hydrostatic compression of hexahydro-1,3,5-trinitro-1,3,5-triazine and beta-octahydro-1,3,5,7-tetranitro-1,3,5,7-tetrazocine. J. Appl. Phys., 83(8):4142–4145, APR 15 1998.

[81] Dan C. Sorescu, Betsy M. Rice, and Donald L. Thompson. Theoretical studies of the hydrostatic compression of rdx, hmx, hniw, and petn crystals. J. Phys. Chem. B, 103(32):6783–6790, 1999.

[82] Hong-Ling Cui, Guang-Fu Ji, Xiang-Rong Chen, Qing-Ming Zhang, Dong-Qing Wei, and Feng Zhao. Phase transitions and mechanical properties of octahydro-1,3,5,7-tetranitro-1,3,5,7-tetrazocine in different crystal phases by molecular dynamics simulation. J. Chem. Eng. Data, 55(9):3121–3129, 2010.

[83] J. C. Gump and S. M. Peiris. Isothermal equations of state of beta octahydro-1,3,5,7-tetranitro-1,3,5,7-tetrazocine at high temperatures. J. Appl. Phys., 97(5):053513, MAR 1 2005.

[84] Hong Liu, Jijun Zhao, Dongqing Wei, and Zizheng Gong. Structural and vibrational properties of solid nitromethane under high pressure by density functional theory. J. Chem. Phys., 124(12):–, 2006.

[85] Francis Birch. Finite elastic strain of cubic crystals. Phys. Rev., 71:809–824, Jun 1947.

[86] Lewis L. Stevens and Craig J. Eckhardt. The elastic constants and related properties of beta-hmx determined by brillouin scattering. J. Chem. Phys., 122(17):174701, 2005.

[87] T D Sewell, D Bedrov, R Menikoff, and G D Smith. Elastic properties of HMX. In Furnish, MD and Thadhani, NN and Horie, Y, editor, Shock compression of condensed matter-2001, pts 1 and 2, proceedings, volume 620 of AIP Conference Proceedings, pages 399–402. Amer Phys Soc, SCCM Top Grp; Amer Phys Soc, Educ Div; Georgia Inst Technol, 2002. 12th International Conference of the American-Physical-Society Topical-Group-on-Shock-Compression-of-Condensed-Matter, ATLANTA, GA, JUN 24-29, 2001.

[88] J. M. Zaug. Elastic constants of beta-HMX and tantalum, equation of state of supercritical fluids and fluid mixtures and thermal transport determinations . pages 498–509. 11 INT DET S SNOWM C, 1998. 11th International Detonation Symposium Location: Snowmass Village, Colorado.

[89] T D Sewell, R Menikoff, D Bedrov, and G D Smith. A molecular dynamics simulation study of elastic properties of HMX. J. Chem. Phys., 119(14):7417–7426, 2003.

[90] Lai-Yu Lu, Dong-Qing Wei, Xiang-Rong Chen, Guang-Fu Ji, Xi-Jun Wang, Jing Chang, Qing-Ming Zhang, and Zi-zheng Gong. The pressure-induced phase transition of the solid beta-HMX. Mol. Phys., 107:2373–2385, 2009.

[91] Jun Chen, Yao Long, YongGang Liu, FuDe Nie, and JinShan Sun. The first-principle study on the equation of state of hmx under high pressure. Science China Physics, Mechanics and Astronomy, 54(5):831–835, 2011.

[92] D. G. Pettifor. Theoretical predictions of structure and related properties of intermetallics. Mater. Sci. Technol., 8(4):345–349, APR 1992.

[93] D. D. Dlott and M. D. Fayer. Shocked molecular-solids - vibrational up pumping, defect hot spot formation, and the onset of chemistry. J. Chem. Phys., 92(6):3798–3812, MAR 15 1990.

[94] Weihua Zhu, Jijuan Xiao, Guangfu Ji, Feng Zhao, and Heming Xiao. First-principles study of the four polymorphs of crystalline octahydro-1,3,5,7-tetranitro-1,3,5,7-tetrazocine. J. Phys. Chem. B, 111(44):12715–12722, NOV 8 2007.

[95] J. J. Gilman. Chemical-reactions at detonation fronts in solids. Philos. Mag. B, 71(6):1057–1068, JUN 1995.

[96] T Luty, P Ordon, and C. J. Eckhardt. A model for mechanochemical transformations: Applications to molecular hardness, instabilities, and shock initiation of reaction. J. Chem. Phys., 117(4):1775–1785, JUL 22 2002.

[97] M M Kuklja, E V Stefanovich, and A B Kunz. An excitonic mechanism of detonation initiation in explosives. J. Chem. Phys., 112(7):3417–3423, FEB 15 2000.

[98] M. M. Kuklja and A. B. Kunz. Compression-induced effect on the electronic structure of cyclotrimethylene trinitramine containing an edge dislocation. J. Appl. Phys., 87(5):2215–2218, MAR 1 2000.

[99] E.L. Baker, W. Balas, C. Capellos, J. Pincay, L. Stiel, Report OMBNo. 0704-01-0188

[100] Esen S, Souers P C, Vitello P. Prediction of the non-ideal detonation performance of commercial explosives using the DeNE and JWL++ codes. Int J Numer Methods Eng, 2005, 64: 1889–1914

[101] Gordon J M, Gross K C, Perram G P. Empirical model for the temporally resolved temperatures of postdetonation fire balls for aluminized high explosives. Proc SPIE Int Soc Opt Eng, 2011, 8018: 80181M-80181M-8

[102] Keshavarz M H. New method for predicting detonation velocities of aluminized explosives. Combust Flame, 2005, 142: 303–307.

[103] Zhang Q, Xiang C, Liang H M. Prediction of the explosion effect of aluminized explosives. Sci China-Phys Mech Astron, 2013, 56:1004-1009

[104] J. D. Clayton and R. Becker. Elastic-plastic behavior of cyclotrimethylene trinitramine single crystals under spherical indentation: Modeling and simulation. J. Appl. Phys., 111(6):063512, 2012.

[105] Suvranu De, Amir R. Zamiri, and Rahul. A fully anisotropic single crystal model for high strain rate loading conditions with an application to α-rdx. J. Mech. Phys. Solids, 64(0):287 – 301, 2014.

[106] Amir Reza Zamiri and Suvranu De. Modeling the anisotropic deformation response of β-hmx molecular crystals. Propellants, Explosives, Pyrotechnics, 36(3):247–251, 2011.

[107] Amir Reza Zamiri and Suvranu De. Deformation distribution maps of

β-HMX molecular crystals. J. Phys. D-Appl. Phys., 43(3):035404, JAN 27 2010.

[108] J Vial, D Picart, P Bailly, and F Delvare. Numerical and experimental study of the plasticity of hmx during a reverse edge-on impact test. Modelling Simul. Mater. Sci. Eng.

[109] D. J. Luscher, M. A. Buechler, and N. A. Miller. Self-consistent modeling of the influence of texture on thermal expansion in polycrystalline tatb. Modelling Simul. Mater. Sci. Eng.

[110] Yao Long and Jun Chen. Theoretical study of phonon density of states, thermodynamic properties and phase transitions for hmx. Philos. Mag., 94(23):2656–2677, 2014.

[111] Nathan R Barton, Nicholas W Winter, and John E Reaugh. Defect evolution and pore collapse in crystalline energetic materials. Modelling Simul. Mater. Sci. Eng.

[112] H. H. Cady, D. T. Ccromer, and A. C. Larson. Crystal structure of alpha- HMX and a refinement of structure of beta-HMX. Acta Crystallogr., 16(7):617, 1963.

[113] Ting-Ting Zhou and Feng-Lei Huang. Effects of defects on thermal decomposition of hmx via reaxff molecular dynamics simulations. J. Phys. Chem. B, 115(2):278–287, 2011.

[114] Tingting Zhou, Huajie Song, Yi Liu, and Fenglei Huang. Shock initiated thermal and chemical responses of hmx crystal from reaxff molecular dynamics simulation. Phys. Chem. Chem. Phys., 16:13914–13931, 2014.

[115] Luzheng Zhang, Sergey V. Zybin, Adri C. T. Van Duin, and William A.

Goddard, III. Modeling high rate impact sensitivity of perfect rdx and hmx crystals by reaxff reactive dynamics. J. Energ. Mater., 28:92 – 127, 2010.

[116] M. Warrier, P. Pahari, and S. Chaturvedi. Interatomic potential parameters for molecular dynamics simulations of rdx using a reactive force field: A validation study. J. Phys. Conf. Ser., 377(1):012100, 2012.

[117] Klime, J., Bowler, D. R. & Michaelides, A. Chemical accuracy for the van der waals density functional. Journal of Physics: Condensed Matter 22, 022201 (2010).

[118] Cooper, V. R. Van der waals density functional: An appropriate exchange functional. Phys. Rev. B 81, 161104 (2010).

[119] Berland, K. & Hyldgaard, P. Exchange functional that tests the robustness of the plasmon description of the van der waals density functional. Phys. Rev. B 89, 035412 (2014).

[120] Hamada, I. van der waals density functional made accurate. Phys. Rev. B 89, 121103 (2014).

[121] Baowen Li, Jinghua Lan, and Lei Wang, Interface Thermal Resistance between Dissimilar Anharmonic Lattices, Phys. Rev. Lett. 95, 104302

[122] R Ravelo, B L Holian, T C Germann, et al. Constant-stress Hugoniot method for following the dynamical evolution of shocked matter. Physical Review B. 70 (1), 2004: 014103.

[123] R J Karpowicz. T B Brill. The beta to delta transformation of HMX-Its thermal analysis and relationship to propellants. Aiaa Journal 20.11 (1982): 1586-1591.

[124] M A Cook. The science of high explosives. American Chemical Society Monograph Series. Reinhold Publishing Corporation, 1958.

[125] A W Campbell, W C Davis, and J R Travis. Shock initiation of detonation in liquid explosives. In Third Symposium on Detonation, volume ACR 52, 469–498. Office of Naval Research, 1960.

[126] A W Campbell, W C Davis, J B Ramsay, and J R Travis. Shock initiation of solid explosives. In Third Symposium on Detonation, volume ACR 52, 499–519. Office of Naval Research, 1960.

[127] S Palmer. Private communication. Cavendish Laboratory, Cambridge University.

[128] D A Jones, G Kemister, R A Borg. Numerical simulation of detonation in condensed phase explosives. No. DSTO-TR-0705. Aeronautical and maritime research lab Melbourne (Australia), 1998.

[129] J E Field, N K Bourne, S J P Palmer, et al. Hot-spot ignition mechanisms for explosives and propellants. Philosophical Transactions of the Royal Society of London A: Mathematical, Physical and Engineering Sciences 339.1654 (1992): 269-283.

[130] Y B Zeldovich. On the theory of the propagation of detonations on gaseous systems. Zh. Eksp. Teor. Fiz. 10(5), 542–568 (1940).

[131] J von Neuman. Theory of detonation waves. Institute for advanced study princeton NJ, 1942.

[132] W Döring. Über den detonationsvorgang in gasen. Annalen der Physik 435.6 -7 (1943): 421 436.

[133] N L Allinger, H Y Young, H L Jenn. "Molecular mechanics. The MM3 force field for hydrocarbons. 1." Journal of the American Chemical Society 111.23 (1989): 8551-8566.

[134] N L Allinger, F Li, L Yan. "Molecular mechanics. The MM3 force field for alkenes." Journal of Computational Chemistry 11.7 (1990): 848-867.

[135] N L Allinger, F Li, L Yan et al. (1990). Molecular mechanics (MM3) calculations on conjugated hydrocarbons. Journal of Computational Chemistry, 11(7), 868-895.

[136] S L Mayo, B D Olafson, W A Goddard III. "DREIDING: a generic force field for molecular simulations." Journal of Physical chemistry 94.26 (1990): 8897-8909.

[137] A K Rappe, C J Casewit, K S Colwell, K. S, et al (1992). UFF, a full periodic table force field for molecular mechanics and molecular dynamics simulations. Journal of the American chemical society, 114(25), 10024-10035.

[138] A K Rappe, W A. Goddard III. "Charge equilibration for molecular dynamics simulations." The Journal of Physical Chemistry 95.8 (1991): 3358-3363.

[139] K Chenoweth, A C van Duin, W A Goddard III. "ReaxFF reactive force field for molecular dynamics simulations of hydrocarbon oxidation." The Journal of Physical Chemistry A 112.5 (2008): 1040-1053.

[140] A C van Duin, Y Zeiri, F Dubnikova, et al. (2005). Atomistic-scale simulations of the initial chemical events in the thermal initiation of triacetonetriperoxide. Journal of the American Chemical Society, 127(31), 11053-11062.

[141] K I Nomura, R K Kalia, A Nakano, et al. (2007). Dynamic transition in the structure of an energetic crystal during chemical reactions at shock front prior to detonation. Physical review letters, 99(14), 148303.

[142] L Zhang, S V Zybin, A C van Duin, et al. (2009). Carbon cluster formation during thermal decomposition of octahydro-1, 3, 5, 7-tetranitro-1, 3, 5, 7-tetrazocine and 1, 3, 5-triamino-2, 4, 6-trinitrobenzene high explosives from ReaxFF reactive molecular dynamics simulations. The Journal of Physical Chemistry A, 113(40), 10619-10640.

[143] A Strachan, A C van Duin, D Chakraborty, et al. (2003). Shock waves in high-energy materials: The initial chemical events in nitramine RDX. Physical Review Letters, 91(9), 098301.

[144] F Guo, H Zhang, X Cheng. "Molecular dynamic simulations of solid nitromethane under high pressures." Journal of Theoretical and Computational Chemistry 9.01 (2010): 315-325.

[145] J Budzien, A P Thompson, S V Sergey. "Reactive molecular dynamics simulations of shock through a single crystal of pentaerythritol tetranitrate." The Journal of Physical Chemistry B 113.40 (2009): 13142-13151.

[146] K Chenoweth, A C Van Duin, S Dasgupta, et al. (2009). Initiation mechanisms and kinetics of pyrolysis and combustion of JP-10 hydrocarbon jet fuel. The Journal of Physical Chemistry A, 113(9), 1740-1746.

[147] J J Monaghan, J C Lattanzio. A refined particle method for astrophysical problems. Astronomy and astrophysics 149 (1985): 135-143.

[148] J J Monaghan. Smoothed particle hydrodynamics. Annual review of astronomy and astrophysics 30.1 (1992): 543-574.

[149] J P Morris. A study of the stability properties of smooth particle hydrodynamics. Publications of the Astronomical Society of Australia, 1994, 13(01), 97-102.

[150] J J Monaghan, R A Gingold. Shock simualtion by the particle method SPH. J Comput Phys. 1983; 52:374-389.

[151] J J Monaghan, J Poinracic. Artificial viscosity for particle methods. Appl numer math. 1985; 1: 187-194.

[152] J J Monaghan. SPH meets the shocks of Noh. Monash University. 1987.

[153] J R Shao, H Q Li, G R Liu, M B Liu. An improved SPH method for modeling liquid sloshing dynamics. Comput. Struct. 2012.100-101: 18-26.

[154] G R Johnson, W H Cook. A constitutive model and data for metals subjected to large strains, high strain rates and high temperatures. The Hague, Netherlands: International Ballistics Committee; 1983. p541-547.

[155] S B Segletes. An Analysis on the Stability of the Mie-Gruneisen Equation of State for Describing the Behavior of Shock-Loaded Materials. No. BRL-TR-3214. Army ballistic research lab aberdeen proving ground MD, 1991.

[156] M Arienti, E Morano, J E Shepherd. Shock and detonation modeling with the Mie-Gruneisen equation of state, GALCIT ReportFM99-8, 2004.

[157] L Hernquist, N Katz. "TREESPH-A unification of SPH with the hierarchical tree method." The Astrophysical Journal Supplement Series 70 (1989): 419-446.

[158] M L Hobbs, M R Baer. Proceedings of the tenth synposium (international) on detoantion. Boston, MA, 1993.

[159] W A Trzcinski, S Cudzilo, L Szymanczyk. Studies of detonation characteristics of aluminum enriched RDX compositions, Propellants, Explosive, Pyrotechnics, 32(5) (2007), 392-400.

[160] W A Trzcinski, S Cudzilo, J Paszula, J Callaway. Study of the effect of additive particles size on non-ideal explosive performance, Propellants, Explosive, Pyrotechnics, 335 (2008), 227-235.

[161] P J Miller. "A reactive flow model with coupled reaction kinetics for detonation and combustion in non-ideal explosives." MRS Proceedings. Vol. 418. Cambridge University Press, 1995.

[162] V W Manner, S J Pemberton, J A Gunderson, et al. "The Role of Aluminum in the Detonation and Post-Detonation Expansion of Selected Cast HMX-Based Explosives."Propellants, Explosives, Pyrotechnics 37.2 (2012): 198-206.

[163] A C Mitchell, W J Nellis. Shock compression of aluminum, copper, and tantalum. Journal of Applied Physics 52.5 (1981): 3363-3374.

[164] R A MacDonald, W M MacDonald. Thermodynamic properties of fcc metals at high temperatures. Physical review B 24.4 (1981): 1715.

[165] L G Hill, R A Catanach. W-76 PBX 9501 cylinder tests. Los Alamos (1998).

[166] J J Monaghan "Simulating free surface flows with SPH." Journal of computational physics 110.2 (1994): 399-406.

[167] P W Randles, L D Libersky. "Smoothed particle hydrodynamics: some recent improvements and applications." Computer methods in applied mechanics and engineering 139.1 (1996): 375-408.

[168] G R Johnson, R A Stryk, S R Beissel. "SPH for high velocity impact computations." Computer methods in applied mechanics and engineering 139.1 (1996): 347-373.

[169] A Colagrossi, M Landrini. "Numerical simulation of interfacial flows by smoothed particle hydrodynamics." Journal of Computational Physics 191.2 (2003): 448-475.

[170] M Ozbulut, M. Yildiz, O Goren. "A numerical investigation into the correction algorithms for SPH method in modeling violent free surface flows." International Journal of Mechanical Sciences 79 (2014): 56-65.

[171] S K Godunov. "A difference method for numerical calculation of discontinuous solutions of the equations of hydrodynamics." Matematicheskii Sbornik 89.3 (1959): 271-306.

[172] E F Toro. Riemann solvers and numerical methods for fluid dynamics: a practical introduction. Springer Science & Business Media, 2013.

[173] S Inutsuka. "Godunov-type SPH." Memorie della Societa Astronomica Italiana 65 (1994): 1027.

[174] S Inutsuka. "Reformulation of smoothed particle hydrodynamics with Riemann solver." Journal of Computational Physics 179.1 (2002): 238-267.

[175] J J Monaghan. "SPH and Riemann solvers." Journal of Computational Physics 136.2 (1997): 298-307.

[176] A N Parshikov, S A Medlin, I I loukashenko, et al. "Improvements in SPH method by means of interparticle contact algorithm and analysis of perforation tests at moderate projectile velocities." International Journal of Impact Engineering 24.8 (2000): 779-796.

[177] A N Parshikov, S A Medin. "Smoothed particle hydrodynamics using interparticle contact algorithms." Journal of computational physics 180.1 (2002): 358-382.

[178] S H Cha, A P Whitworth. (2003). Implementations and tests of Godunov-type particle hydrodynamics. Monthly Notices of the Royal Astronomical Society, 340(1), 73-90.

[179] S Borgani, G Murante, R Brunino, et al. "Hydrodynamic Simulations with the Godunov SPH." Advances in Computational Astrophysics: Methods, Tools, and Outcome. Vol. 453. 2012.

[180] K Iwasaki, S Inutsuka. "Smoothed particle magnetohydrodynamics with a Riemann solver and the method of characteristics." Monthly Notices of the Royal Astronomical Society 418.3 (2011): 1668-1688.

[181] K Puri, P Ramachandran. "Approximate Riemann solvers for the Godunov SPH (GSPH)." Journal of Computational Physics 270 (2014): 432-458.

[182] C L Mader. Numerical modeling of detonations. Los Alamos Series in Basic and Applied Sciences, Berkeley: University of California Press, 1979 1 (1979).

[183] C M Tarver, E M McGuire. "Reactive flow modeling of the interaction of TATB detonation waves with inert materials." The Twelfth Symposium (International) on Detonation. 2002.

[184] C M Tarver, J O Hallquist. Modeling two-dimensional shock initiation and detonation-wave phenomena in PBX 9404 and LX-17. No. UCRL-84990; CONF-810602-29. Lawrence Livermore National Lab., CA (USA), 1981.

[185] C M Tarver, S K Chidester. Modeling LX-17 detonation growth and decay using the ignition and growth model. In: Shock Compression of Condensed Matter-2009, AIP Conference Proceedings, vol. 1195, pp.249-254. Nashville (2009).

[186] A K Kapila, D W Schwendeman, J B Bdzil, et al. A study of detoantion diffraction in the ignition-and-growth model. Combust theor model.2006 (11); 5: 781-822.

[187] M L Garcia, C M Tarver. Three-dimensional ignition and growth reactive flow modeling of prism faliure tests on PBX 9502. 13th nternational Detonation Symposium. 2006.

[188] A Connolly, Adam. Smoothed particle hydrodynamics for high velocity impact simulations. Diss. Imperial College London, 2013.

List of Publications Out of This Project

1. Guirong Liu, Guangyu Wang, Qing Peng, Suvranu De. A Micro-Macro coupling approach of MD-SPH method for reactive energetic materials. 19th Biennial Conference on Shock Compression of Condensed Matter (SCCM-2015), Tampa, FL, USA, 2015.

2. Guangyu Wang, Guirong Liu, Qing Peng, Suvranu De, Dianlei Feng, Moubin Liu. "A 3D Smoothed Particle Hydrodynamics Method with Reactive Flow Model for the Simulation of ANFO." Propellants, Explosives, Pyrotechnics (2015).

3. Guangyu Wang, Qing Peng, Guirong Liu, Suvranu De. "Microscopic study of the equation of state of β-HMX using reactive molecular dynamics simulations." RSC Advances 5.69 (2015): 55892-55900.

4. Guangyu Wang, Guirong Liu, Qing Peng, Suvranu De. A SPH implementation with ignition and growth and afterburning model for the simulation of aluminized explosives. International Journal of Computational Methods.

5. Guangyu Wang, Guirong Liu, Qing Peng, Suvranu De. A Godunov SPH method and its application in the simulation of energetic materials. Journal of Computational Physics. (under review)

6. G. R. Liu, C. E. Zhou, and G. Y. Wang. "An implementation of the smoothed particle hydrodynamics for hypervelocity impacts and penetration to layered composites." International Journal of Computational Methods 10.03 (2013): 1350056.

7. Qing Peng, Rahul, Guangyu Wang, Guirong Liu, Suvranu De. "Structures, mechanical properties, equations of state, and electronic properties of β-HMX under hydrostatic pressures: a DFT-D2 study." *Physical Chemistry Chemical Physics* 16.37 (2014): 19972-19983.

8. Qing Peng, Rahul, Guangyu Wang, Guirong Liu, Stefan Grimme, Suvranu De. "Predicting Elastic Properties of β-HMX from First-principles Calculations." The Journal of Physical Chemistry B 119.18 (2015): 5896-5903.

Appendix

The ReaxFF-d3 reactive force field obtained from quantum mechanics simulation is as follow:

Reactive MD-force field

```
 39       ! Number of general parameters
   50.0000 !Comment here
    9.4514 !Comment here
   30.3695 !Comment here
  216.7028 !Comment here
   12.7702 !Comment here
    0.0000 !Comment here
    1.0701 !Comment here
    7.5000 !Comment here
   11.9083 !Comment here
   13.3822 !Comment here
  -10.3004 !Comment here
    0.0000 !Comment here
   10.0000 !Comment here
    2.8793 !Comment here
   33.8667 !Comment here
    3.2650 !Comment here
    1.0563 !Comment here
    2.0384 !Comment here
    6.1431 !Comment here
    6.9290 !Comment here
    0.0283 !Comment here
    0.0570 !Comment here
   -2.4837 !Comment here
    5.8374 !Comment here
   10.0000 !Comment here
    1.8820 !Comment here
   -1.2327 !Comment here
    2.1861 !Comment here
    1.5591 !Comment here
    0.0100 !Comment here
    5.1243 !Comment here
    3.0533 !Comment here
   38.9494 !Comment here
    2.1533 !Comment here
    0.5000 !Comment here
    1.0000 !Comment here
    5.0000 !Comment here
```

```
   0.0000 !Comment here
   7.7896 !Comment here
 7    !Nr of atoms; cov.r; valency;a.m;Rvdw;Evdw;gammaEEM;cov.r2;
          alfa;gammavdW;valency;Eunder;Eover;chiEEM;etaEEM;n.u.
          cov r3;Elp;Heat inc.;n.u.;n.u.;n.u.;n.u.
          ov/un;val1;n.u.;val3,vval4
C    1.3742   4.0000  12.0000   1.9684   0.1723   0.8712   1.2385   4.0000
     8.7696 100.0000   4.0000  31.0823  79.5548   5.7254   6.9235   0.0000
     1.2104   0.0000 183.8108   5.7419  33.3951  11.9957   0.8563   0.0000
    -2.8983   4.7820   1.0564   4.0000   2.9663   1.6737   0.1421  14.0707
     0.0001   1.9255
H    0.6867   1.0000   1.0080   1.3525   0.0616   0.8910  -0.1000   1.0000
     9.1506 100.0000   1.0000   0.0000 121.1250   3.8446  10.0839   1.0000
    -0.1000   0.0000  58.4369   3.8461   3.2540   1.0000   1.0698   0.0000
   -15.7683   2.1504   1.0338   1.0000   2.8793   1.2669   0.0139  12.4538
     0.0001   1.4430
O    1.3142   2.0000  15.9990   1.9741   0.0880   0.8712   1.1139   6.0000
     9.9926 100.0000   4.0000  29.5271 116.0768   8.5000   7.1412   2.0000
     0.9909  14.7235  69.2921   9.1371   1.6258   0.1863   0.9745   0.0000
    -3.5965   2.5000   1.0493   4.0000   2.9225   1.7221   0.1670  13.9991
   624.0000   1.7500
N    1.2456   3.0000  14.0000   2.0437   0.1035   0.8712   1.1911   5.0000
     9.8823 100.0000   4.0000  32.4758 100.0000   6.8453   6.8349   2.0000
     1.0636   0.0276 127.9672   2.2169   2.8632   2.4419   0.9745   0.0000
    -4.0959   2.0047   1.0183   4.0000   2.8793   1.5967   0.1649  13.9888
  1239.0000   1.8300
S    1.9647   2.0000  32.0600   2.0783   0.2176   1.0336   1.5386   6.0000
     9.9676   5.0812   4.0000  35.1648 112.1416   6.5000   8.2545   2.0000
     1.4703   9.4922  70.0338   8.5146  28.0801   8.5010   0.9745   0.0000
   -10.0773   2.7466   1.0338   6.2998   2.8793   1.8000   0.0000  14.0000
   180.0000   2.0783
Si   2.0276   4.0000  28.0600   2.2042   0.1322   0.8218   1.5758   4.0000
    11.9413   2.0618   4.0000  11.8211 136.4845   1.8038   7.3852   0.0000
    -1.0000   0.0000 126.5331   6.4918   8.5961   0.2368   0.8563   0.0000
    -3.8112   3.1873   1.0338   4.0000   2.5791   0.0000   0.0000   0.0000
   180.0000   2.2042
X -1000.0000   2.0000   1.0080   2.0000   0.0000   1.0000  -0.1000   6.0000
    10.0000   2.5000   4.0000   0.0000   0.0000   8.5000   1.5000   0.0000
    -0.1000   0.0000  -2.3700   8.7410  13.3640   0.6690   0.9745   0.0000
   -11.0000   2.7466   1.0338   4.0000   2.8793   0.0000   0.0000   0.0000
   180.0000   2.0000
18      ! Nr of bonds; Edis1;LPpen;n.u.;pbe1;pbo5;13corr;pbo6
```

```
                    pbe2;pbo3;pbo4;n.u.;pbo1;pbo2;ovcorr
 1  1 141.9346 113.4487  67.6027   0.1554  -0.3045   1.0000  30.4515   0.4283
       0.0801  -0.2113   8.5395   1.0000  -0.0933   6.6967   1.0000   0.0000
 1  2 163.6889   0.0000   0.0000  -0.4525   0.0000   1.0000   6.0000   0.5921
      12.1053   1.0000   0.0000   1.0000  -0.0097   8.6351   0.0000   0.0000
 1  3 159.7219 116.8921  77.9315  -0.4324  -0.1742   1.0000  15.0019   0.5160
       1.2934  -0.3079   7.0252   1.0000  -0.1543   4.5116   0.0000   0.0000
 1  4 128.9104 171.2945 100.5836  -0.1306  -0.4948   1.0000  26.7458   0.4489
       0.3746  -0.3549   7.0000   1.0000  -0.1248   4.9232   1.0000   0.0000
 1  5 128.7959  56.4134  39.0716   0.0688  -0.4463   1.0000  31.1766   0.4530
       0.1955  -0.3587   6.2148   1.0000  -0.0770   6.6386   1.0000   0.0000
 2  2 169.8421   0.0000   0.0000  -0.3591   0.0000   1.0000   6.0000   0.7503
       9.3119   1.0000   0.0000   1.0000  -0.0169   5.9406   0.0000   0.0000
 2  3 219.7016   0.0000   0.0000  -0.6643   0.0000   1.0000   6.0000   0.9854
       5.1146   1.0000   0.0000   1.0000  -0.0532   5.1189   0.0000   0.0000
 2  4 208.0443   0.0000   0.0000  -0.3923   0.0000   1.0000   6.0000   0.3221
      10.5505   1.0000   0.0000   1.0000  -0.0690   6.2949   0.0000   0.0000
 2  5 128.6090   0.0000   0.0000  -0.5555   0.0000   1.0000   6.0000   0.4721
      10.8735   1.0000   0.0000   1.0000  -0.0242   9.1937   1.0000   0.0000
 2  6 137.1002   0.0000   0.0000  -0.1902   0.0000   1.0000   6.0000   0.4256
      17.7186   1.0000   0.0000   1.0000  -0.0377   6.4281   0.0000   0.0000
 3  3 108.9631 158.3501  42.0558   0.1226  -0.1324   1.0000  28.5716   0.2545
       1.0000  -0.2656   8.6489   1.0000  -0.1000   6.8482   1.0000   0.0000
 3  4  85.0402 118.8680  75.7263   0.7080  -0.1062   1.0000  16.6913   0.2407
       0.3535  -0.1906   8.4054   1.0000  -0.1154   5.6575   1.0000   0.0000
 3  5   0.0000   0.0000   0.0000   0.5563  -0.4038   1.0000  49.5611   0.6000
       0.4259  -0.4577  12.7569   1.0000  -0.1100   7.1145   1.0000   0.0000
 3  6 191.1743  52.0733  43.3991  -0.2584  -0.3000   1.0000  36.0000   0.8764
       1.0248  -0.3658   4.2151   1.0000  -0.5004   4.2605   1.0000   0.0000
 4  4 160.6599  73.3721 154.2849  -0.7107  -0.1462   1.0000  12.0000   0.6826
       0.9330  -0.1434  10.6712   1.0000  -0.0890   4.6486   1.0000   0.0000
 4  5   0.0000   0.0000   0.0000   0.4438  -0.2034   1.0000  40.3399   0.6000
       0.3296  -0.3153   9.1227   1.0000  -0.1805   5.6864   1.0000   0.0000
 5  5  96.1871  93.7006  68.6860   0.0955  -0.4781   1.0000  17.8574   0.6000
       0.2723  -0.2373   9.7875   1.0000  -0.0950   6.4757   1.0000   0.0000
 6  6 109.1904  70.8314  30.0000   0.2765  -0.3000   1.0000  16.0000   0.1583
       0.2804  -0.1994   8.1117   1.0000  -0.0675   8.2993   0.0000   0.0000
10    ! Nr of off-diagonal terms; Ediss;Ro;gamma;rsigma;rpi;rpi2
 1  2   0.0464   1.8296   9.9214   1.0029  -1.0000  -1.0000   0.0000
 1  3   0.1028   1.9277   9.1521   1.3399   1.1104   1.1609 632.0000
 1  4   0.2070   1.7366   9.5916   1.2960   1.2008   1.1262 650.0000
 1  5   0.1408   1.8161   9.9393   1.7986   1.3021   1.4031   0.0000
```

```
 2  3   0.0403   1.6913  10.4801   0.8774  -1.0000  -1.0000   0.0000
 2  4   0.0524   1.7325  10.1306   0.9982  -1.0000  -1.0000 295.0000
 2  5   0.0895   1.6239  10.0104   1.4640  -1.0000  -1.0000   0.0000
 2  6   0.0470   1.6738  11.6877   1.1931  -1.0000  -1.0000   0.0000
 3  4   0.0491   1.7025  10.6101   1.3036   1.1276   1.0173 880.0000
 3  6   0.1263   1.8163  10.6833   1.6266   1.2052  -1.0000   0.0000
61    ! Nr of angles;at1;at2;at3;Thetao,o;ka;kb;pv1;pv2
 1  1  1  74.0317  32.2712   0.9501   0.0000   0.1780  10.5736   1.0400
 1  1  2  70.6558  14.3658   5.3224   0.0000   0.0058   0.0000   1.0400
 1  1  3  65.1700   8.0170   7.5000   0.0000   0.2028  10.0000   1.0400
 1  1  4  65.4228  43.9870   1.5602   0.0000   0.2000  10.0000   1.8525
 1  1  5  74.4180  33.4273   1.7018   0.1463   0.5000   0.0000   1.6178
 1  2  1   0.0000   3.4110   7.7350   0.0000   0.0000   0.0000   1.0400
 1  2  2   0.0000   0.0000   6.0000   0.0000   0.0000   0.0000   1.0400
 1  2  3   0.0000   0.0019   6.0000   0.0000   0.0000   0.0000   1.0400
 1  2  4   0.0000   0.0019   6.0000   0.0000   0.0000   0.0000   1.0400
 1  2  5   0.0000   0.0019   6.0000   0.0000   0.0000   0.0000   1.0400
 1  3  1  72.1018  38.4720   1.3926   0.0000   0.4785   0.0000   1.2984
 1  3  2  89.0416  36.9460   0.4569   0.0000   2.7636   0.0000   2.0494
 1  3  3  89.9987  44.9806   0.5818   0.0000   0.7472   0.0000   1.2639
 1  3  4  70.3281  12.9371   7.5000   0.0000   0.7472   0.0000   1.2639
 1  4  1  68.3788  18.3716   1.8893   0.0000   2.4132   0.0000   1.3993
 1  4  2  90.0000  33.6636   1.1051   0.0000   0.2638   0.0000   1.1376
 1  4  3  86.5585  37.6814   1.1611   0.0000   1.7325   0.0000   1.0440
 1  4  4  74.4818  12.0954   7.5000   0.0000   1.7325   0.0000   1.0440
 1  5  1  79.7037  28.2036   1.7073   0.1463   0.5000   0.0000   1.6453
 1  5  2  85.9449  38.3109   1.2492   0.0000   0.5000   0.0000   1.1000
 1  5  5  85.6645  40.0000   2.9274   0.1463   0.5000   0.0000   1.3830
 2  1  2  76.7339  14.4217   3.3631   0.0000   0.0127   0.0000   1.0400
 2  1  3  56.4426  17.6020   5.3044   0.0000   0.9699   0.0000   1.1272
 2  1  4  71.0777   9.1462   3.4142   0.0000   0.9110   0.0000   1.0400
 2  1  5  63.3289  29.4225   2.1326   0.0000   0.5000   0.0000   3.0000
 2  2  2   0.0000  27.9213   5.8635   0.0000   0.0000   0.0000   1.0400
 2  2  3   0.0000   0.0019   6.0000   0.0000   0.0000   0.0000   1.0400
 2  2  4   0.0000   0.0019   6.0000   0.0000   0.0000   0.0000   1.0400
 2  2  5   0.0000   0.0019   6.0000   0.0000   0.0000   0.0000   1.0400
 2  2  6   0.0000  47.1300   6.0000   0.0000   1.6371   0.0000   1.0400
 2  3  2  82.2020  12.7165   3.9296   0.0000   0.2765   0.0000   1.0470
 2  3  3  81.1709   4.2886   6.5904   0.0000   3.0000   0.0000   1.2618
 2  3  4  75.9203  44.9675   0.8889   0.0000   3.0000   0.0000   1.2618
 2  3  6  83.7634   5.6693   2.7780   0.0000   1.6982   0.0000   1.0400
 2  4  2  55.8679  14.2331   2.9225   0.0000   0.2000   0.0000   2.9932
```

```
 2  4  3  83.8493  44.9000   1.3580   0.0000   0.5355   0.0000   2.5279
 2  4  4  78.7452  24.2010   3.7481   0.0000   0.5355   0.0000   2.5279
 2  5  2  83.8555   5.1317   0.4377   0.0000   0.5000   0.0000   3.0000
 2  5  5  97.0064  32.1121   2.0242   0.0000   0.5000   0.0000   2.8568
 2  6  2  78.3939  20.9772   0.8630   0.0000   2.8421   0.0000   1.0400
 2  6  3  73.8232  16.6592   3.7425   0.0000   0.8613   0.0000   1.0400
 2  6  6  75.6168  21.5317   1.0435   0.0000   2.5179   0.0000   1.0400
 3  1  3  71.7582  26.7070   6.0466   0.0000   0.2000   0.0000   1.8525
 3  1  4  73.7046  23.8131   3.9811   0.0000   0.2000   0.0000   1.8525
 3  2  3   0.0000   0.0019   6.0000   0.0000   0.0000   0.0000   1.0400
 3  2  4   0.0000   0.0019   6.0000   0.0000   0.0000   0.0000   1.0400
 3  2  6   0.0000  31.0427   4.5625   0.0000   1.6371   0.0000   1.0400
 3  3  3  84.2807  24.1938   2.1695 -10.0000   0.7472   0.0000   1.2639
 3  3  4  84.2585  44.1039   0.9185   0.0000   0.7472   0.0000   1.2639
 3  3  6  73.4663  25.0761   0.9143   0.0000   2.2466   0.0000   1.0400
 3  4  3  78.5850  44.3389   1.3239 -26.2246   1.7325  40.0000   1.0440
 3  4  4  77.6245  32.0866   1.8889  -0.9193   1.7325   0.0000   1.0440
 3  6  3  90.0344   7.7656   1.7264   0.0000   0.7689   0.0000   1.0400
 3  6  6  70.3016  15.4081   1.3267   0.0000   2.1459   0.0000   1.0400
 4  1  4  65.6602  40.5852   1.8122   0.0000   0.2000   0.0000   1.8525
 4  2  4   0.0000   0.0019   6.0000   0.0000   0.0000   0.0000   1.0400
 4  3  4  74.2312  25.7005   4.3943   0.0000   0.7472   0.0000   1.2639
 4  4  4  66.4718  15.9087   7.5000   0.0000   1.7325   0.0000   1.0440
 6  2  6   0.0000  31.5209   6.0000   0.0000   1.6371   0.0000   1.0400
 6  3  6  22.1715   3.6615   0.3160   0.0000   4.1125   0.0000   1.0400
 6  6  6  69.3456  21.7361   1.4283   0.0000  -0.2101   0.0000   1.3241
31    ! Nr of torsions;at1;at2;at3;at4;;V1;V2;V3;V2(BO);vconj;n.u;n
 0  1  1  0   0.0930  18.6070  -1.3191  -9.0000  -1.0000   0.0000   0.0000
 0  1  2  0   0.0000   0.0000   0.0000   0.0000   0.0000   0.0000   0.0000
 0  1  3  0   1.7254  86.0769   0.3440  -4.2330  -2.0000   0.0000   0.0000
 0  1  4  0  -1.3258 149.8644   0.4790  -7.1541  -2.0000   0.0000   0.0000
 0  1  5  0   4.0885  78.7058   0.1174  -2.1639   0.0000   0.0000   0.0000
 0  2  2  0   0.0000   0.0000   0.0000   0.0000   0.0000   0.0000   0.0000
 0  2  3  0   0.0000   0.1000   0.0200  -2.5415   0.0000   0.0000   0.0000
 0  2  4  0   0.0000   0.1000   0.0200  -2.5415   0.0000   0.0000   0.0000
 0  2  5  0   0.0000   0.0000   0.0000   0.0000   0.0000   0.0000   0.0000
 0  2  6  0   0.0000   0.0000   0.1200  -2.4847   0.0000   0.0000   0.0000
 0  3  3  0   1.2314 116.5137   0.5599  -4.1412   0.0000   0.0000   0.0000
 0  3  4  0   1.3168  57.0732   0.2679  -4.1516  -2.0000   0.0000   0.0000
 0  3  6  0   0.0000   0.0000   0.1200  -2.4703   0.0000   0.0000   0.0000
 0  4  4  0   2.0000  75.3685  -0.7852  -9.0000  -2.0000   0.0000   0.0000
 0  5  5  0  -0.0170 -56.0786   0.6132  -2.2092   0.0000   0.0000   0.0000
```

```
0  6  6  0   0.0000   0.0000   0.1200  -2.4426   0.0000   0.0000   0.0000
1  1  1  1   0.0000  48.4194   0.3163  -8.6506  -1.7255   0.0000   0.0000
1  1  1  2   0.0000  63.3484   0.2210  -8.8401  -1.8081   0.0000   0.0000
1  1  3  3   1.2707  21.6200   1.5000  -9.0000  -2.0000   0.0000   0.0000
1  1  3  4   1.2181 119.6186  -1.5000  -7.0635  -2.0000   0.0000   0.0000
1  1  4  2  -2.0000 147.2445  -1.5000  -7.0142  -2.0000   0.0000   0.0000
1  1  4  3  -2.0000  47.8326  -1.5000  -9.0000  -2.0000   0.0000   0.0000
1  3  3  1  -1.8804  79.9255  -1.5000  -4.1940  -2.0000   0.0000   0.0000
1  3  4  3   2.0000  96.6281  -1.5000  -3.8076  -2.0000   0.0000   0.0000
1  4  4  3   0.1040  70.1152   0.5284  -3.5026  -2.0000   0.0000   0.0000
2  1  1  2   0.0000  45.2741   0.4171  -6.9800  -1.2359   0.0000   0.0000
2  1  3  4  -2.0000 156.6604   1.1004  -7.3729  -2.0000   0.0000   0.0000
2  3  4  3  -0.2997 152.9040  -1.5000  -4.4564  -2.0000   0.0000   0.0000
2  4  4  3   0.1040  70.1152   0.5284  -3.5026  -2.0000   0.0000   0.0000
3  1  3  3  -2.0000  22.5092   1.5000  -8.9500  -2.0000   0.0000   0.0000
4  1  4  4  -2.0000  20.6655  -1.5000  -9.0000  -2.0000   0.0000   0.0000
9    ! Nr of hydrogen bonds;at1;at2;at3;Rhb;Dehb;vhb1
3  2  3   2.1845  -2.3549   3.0582  19.1627
3  2  4   1.6658  -3.8907   3.0582  19.1627
3  2  5   2.6644  -3.0000   3.0000   3.0000
4  2  3   1.8738  -3.5421   3.0582  19.1627
4  2  4   1.8075  -4.1846   3.0582  19.1627
4  2  5   4.0476  -3.0000   3.0000   3.0000
5  2  3   2.1126  -4.5790   3.0000   3.0000
5  2  4   2.2066  -5.7038   3.0000   3.0000
5  2  5   1.9461  -4.0000   3.0000   3.0000
```

DEPARTMENT OF DEFENSE

DEFENSE THREAT REDUCTION
AGENCY
8725 JOHN J. KINGMAN ROAD
STOP 6201
FORT BELVOIR, VA 22060
ATTN: A. DALTON

DEFENSE TECHNICAL
INFORMATION CENTER
8725 JOHN J. KINGMAN ROAD,
SUITE 0944
FT. BELVOIR, VA 22060-6201
ATTN: DTIC/OCA

DEPARTMENT OF DEFENSE CONTRACTORS

QUANTERION SOLUTIONS, INC.
1680 TEXAS STREET, SE
KIRTLAND AFB, NM 87117-5669
ATTN: DTRIAC